Combustion Fundamentals

NASA–Chinese Aeronautical Establishment (CAE) Symposium

*Proceedings of a symposium
held at NASA Lewis Research Center
Cleveland, Ohio
September 23–27, 1985*

NASA

Combustion Fundamentals

NASA–Chinese Aeronautical Establishment (CAE) Symposium

NASA

National Aeronautics
and Space Administration

**Scientific and Technical
Information Branch**

1986

FOREWORD

In September and October of 1985 Vice President Zhang Chi of the Chinese Aeronautical Establishment led a delegation of management and technical specialists to the United States. Arrangements for the delegation were supervised by Lavonne Parker of NASA. Included in the activities of this delegation was the NASA - Chinese Aeronautical Establishment (CAE) Symposium on Combustion Fundamentals at the NASA Lewis Research Center in Cleveland, Ohio, from September 23 - 27, 1985. This symposium was one of several exchanges resulting from an agreement, signed on January 31, 1979, between the United States of America and the People's Republic of China to exchange technology in the area of civil aeronautics. The technical sessions of this symposium were conducted under the joint chairmanship of Mr. Zhou Xiaoqing of the CAE and Dr. Edward J. Mularz of NASA. Following the presentation of overviews of combustion research activities in each of the organizations, 12 technical papers were given by combustion specialists from both CAE and NASA. Small group discussions were then held to clarify and further examine the presented material. These technical presentations are bound in this publication as a record of the proceedings of this joint symposium.

In addition to the symposium participants, a number of technical observers were present. For the Chinese, these were the remaining members of the CAE delegation. Other observers were combustion specialists from industry and local universities and some members of the Lewis technical staff. Following the symposium, the Chinese delegation toured combustion and related facilities at a number of relevant industries and university establishments.

Technical and other exchanges were open and fruitful with the technical experts using some similar methods, instrumentation, and equipment. Common correlations and approaches and similar academic background existed for a number of the technical experts resulting in an apparent mutual understanding of the technology presented by both the CAE and the NASA combustion experts.

Melvin J. Hartmann
NASA Lewis Research Center

CONTENTS

COMBUSTION RESEARCH IN THE INTERNAL FLUID MECHANICS DIVISION

Edward J. Mularz
Propulsion Directorate
U.S. Army Aviation Research and Technology Activity-AVSCOM
NASA Lewis Research Center
Cleveland, Ohio

At the NASA Lewis Research Center, combustion research is being conducted in the Internal Fluid Mechanics Division. The research is organized into three main functions focusing on the fluid dynamics related to aeropropulsion systems (fig. 1). The first function, computational methods, looks at improved algorithms and new computational fluid dynamic techniques to solve internal flow problems, including heat transfer and chemical reactions. This area also looks at using expert systems and parallel processing as they might be applied to solving internal flow problems.

The second function is fundamental experiments. These experiments can generate benchmark data in support of computational models and numerical codes, or they can focus on the physical phenomena of interest to obtain a better understanding of the physics or chemistry involved as a preamble to models and computer codes.

Computational applications is the third function in the Internal Fluid Mechanics Division. New flow codes are validated against available experimental data, and they are used as a tool to investigate performance of real engine hardware. Since the geometry may be quite complex for the system being analyzed, large grids and computer storage may be required. The hardware of interest includes combustion chambers, high-speed inlets, and turbomachinery components (e.g., a centrifugal compressor).

The goal of this research is to bring computational fluid dynamics to a state of practical application for the aircraft engine industry. As shown in figure 2, the approach is to have a strongly integrated computational and experimental program for all the disciplines associated with the gas turbine and other aeropropulsion systems by advancing the understanding of flow physics, heat transfer, and combustion processes. The computational and experimental research is integrated in the following way: the experiments that are performed provide an empirical data set so that physical models can be formulated to describe the processes that are occurring - for example, turbulence or chemical reaction. These experiments also form a data base for those who are doing code development by providing experimental data against which the codes can be verified and assessed. Models are generated as closure to some of the numerical codes, and they also provide physical insight for experiments. At the same time, codes which solve the complete Navier-Stokes equations can be used as a kind of numerical experiment from which far more extensive data can be obtained than ever could be obtained experimentally. This could provide physical insight into the complex processes that are taking place. These codes are also exercised against experimental data to assess the accuracy and applicability of models (e.g., the turbulence model). We feel that a fully integrated computational-experimental research program is more productive than other approaches and that it is the most desirable way of pursuing our goal.

Figure 3 is a cutaway view of a hypothetical combustor which illustrates the typical complex fluid mechanics and combustion features. The flows are highly three-dimensional with turbulence levels, in many cases, comparable in magnitude to the bulk velocity. Liquid fuels are injected as a spray which then undergoes vaporization and mixing. The chemical reaction which occurs causes changes in density and fluid mechanics properties and can cause the formation of a solid phase (soot) with its attendant high-radiation heat transfer. An understanding of these physical processes is needed before accurate numerical codes can be built and used as a predictive tool in the design process. In addition, the numerical methods for three-dimensional flows need improvements in accuracy and efficiency in order to properly simulate the features of these flows.

This then is the framework of the combustion research program. As shown in figure 4, the program is divided into four elements: advanced numerics, fuel sprays, fluid mixing, and radiation chemistry. The research in each of these elements is focused on the long-range objective of developing numerical codes that can be used as a predictive tool to describe both two- and three-dimensional flows. Once the codes can be used with confidence, industry will be able to integrate them into their combustor design system.

Before discussing the specific research currently taking place, I would like to describe the major computing hardware now being used at NASA Lewis to compute reacting internal flows. Lewis currently has a CRAY 1-S computer which is tied to an IBM 370 system for input/output. It has a relatively small storage capacity, but a very high calculation speed. In the near future a CRAY X-MP will be installed (fig. 5). It will replace the CRAY 1-S and will provide a modest increase in computer speed. Core storage, however, will increase dramatically from 2 million words to 36 million words, and a high-speed solid-state device, which is practically equivalent to core memory, will also be included. In addition, the new equipment will have two processors which will give Lewis some ability to start using algorithms that can take advantage of simultaneous processing and thus increase the computation speed even further.

In addition to the computers located at Lewis, NASA is building a "super computer" at its Ames Research Center called the Numerical Aerodynamic Simulator (NAS) (fig. 6). The NAS computer will be accessed at both NASA Langley and NASA Lewis through satellite linkage with a UNIX operating system. In its current configuration, the NAS computer is a CRAY 2 with 256 megawords of memory, which will enable it to make very large calculations of chemically reacting internal fluid flows. It will have four processors. In addition, as the state-of-the-art of computers advances changes will be made in the NAS computer to reflect these advances.

The current research in combustion can be summarized in six major activities. The first activity is called improved numerical methods for complex flows. Numerical error is a big problem with the current numerical codes. This numerical error must be reduced before the accuracy of physical models can be assessed. The grids used in calculations that are performed with state-of-the-art codes are very sensitive to the flow direction relative to that grid, and at high angles this sensitivity leads to serious numerical errors. Techniques to reduce numerical diffusion, or error, and to virtually eliminate it from calculations are being pursued. Work is also underway to establish second-order accurate closure models for turbulent reacting flow.

The second activity involves the development of techniques for making predictive calculations of chemically reacting flow. One of the more promising techniques, which is really in its infancy, is called direct numerical simulations, or DNS. In this technique, the Navier-Stokes equations are solved directly without any modeling of the turbulence. This technique is currently being applied to reacting shear layers. Although this is a relatively simple flow, there is nevertheless a lot of complexity associated with it. Much work remains to be done with this technique, but the results to date have been very promising.

Another technique that has been used in several kinds of flows is called the random vortex method. This technique accounts for the vorticity generated at the wall of the confined flow and solves the vorticity equation without any turbulence closure modeling. Calculated results of flow over a rearward facing step show many of the characteristics seen in high-speed movies of turbulent reacting flow experiments.

The third activity involves benchmark experiments for code development and verification. Two-phase flow research is currently underway. Detailed data are required for code assessment, and instruments which Lewis has helped to develop now show much promise of being able to make the appropriate measurements. (Those instruments are also being used to support icing research.) Research is also being conducted on numerical calculation of two-phase flow. With the data from the experiments, an assessment of the current code capability will be made to guide future code development efforts. In addition, an extensive set of experiments is being conducted to look at the mixing of dilution jets into a cross stream in a channel. A substantial range of parametric variables has been studied, and a very complete set of data has been established.

The next activity is computer code applications. Currently available codes are applied to real systems. The study of flow in the transition section of a reverse flow combustor is an example of such work. Here a flow in which fuel has already been burned has to undergo a 180° annular turn. Very strong secondary flows arise, and the analysis is very complex. Another example is the application of the Lewis-developed general chemical kinetics programs and chemical equilibrium codes to problems of practical interest. These codes are used throughout the world.

The next activity is code development for thermochemical properties and kinetic rates. Thermodynamic calculations for real gases are being performed in support of future combustion models. The modeling of chemical kinetic computations for complex reactions is also being actively developed in support of future computer codes.

The final activity in the current combustion research program is to advance the understanding of chemical mechanisms in reacting flow. Chemical kinetic rates are measured using a shock tube facility. The data from this experiment are used to assess the kinetic models for various fuels of interest in aeropropulsion systems. Detailed characteristics of one- and two-dimensional controlled flames are also being established. We are interested in studying the behavior of some of the minor species of flames and in looking at the soot nucleation growth and eventual soot consumption in flames. Radiation heat transfer is dominant in combustors and other aeropropulsion systems. The control of soot nucleation and growth is essential if radiation heat transfer

3

is to be reduced. Also, some of the minor intermediates of combustion are being measured in an attempt to understand the detailed physics involved in flame fronts.

BENCHMARK EXPERIMENTS COMPUTATIONAL METHODS

APPLICATIONS
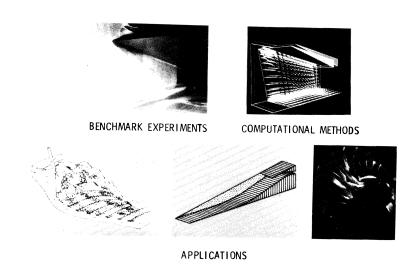
Figure 1. - Fundamental aeropropulsion computational and experimental research in the internal fluid mechanics division.
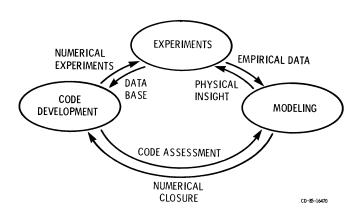
Figure 2. - Integrated computational-experimental methodology for propulsion aerothermodynamics research. Objective - advance the understanding of flow physics, heat transfer, and combustion processes which are fundamental to aeropropulsion.

4
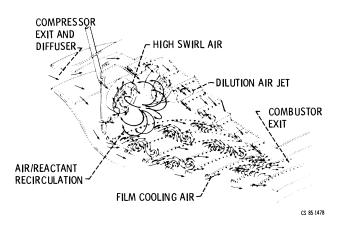
Figure 3. - Illustration of the typical flow phenomena in a gas turbine combustor. Typical flow is fully three-dimensional, has high turbulence levels, has chemical reactions and heat release, and occurs in two phases with vaporization.
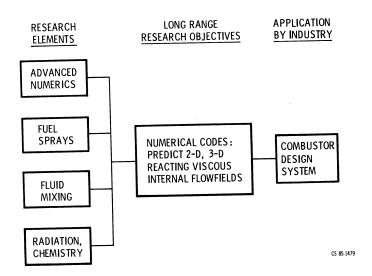
Figure 4. - Fundamental combustion research plan.

5

	CRAY 1-S (PRESENT)	CRAY X-MP (NOV. 85)
CYCLE TIME	12.5 nsec	9.5 nsec
STORAGE	2×10^6 WORDS	4×10^6 WORDS CORE 32×10^6 WORDS SSD
PROCESSORS	1	2
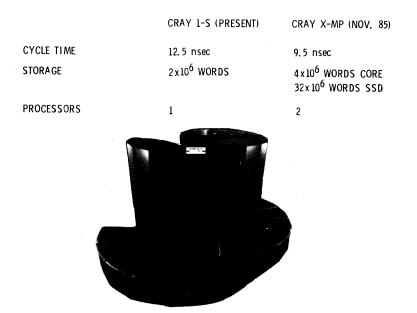
Figure 5. - Comparison of Cray 1-S and Cray X-MP computer capabilities.

NUMERICAL AERODYNAMIC SIMULATION

CRAY 2 with 256 mega words memory
250 mega flops with 4 CPUs
UNIX operating system
Remote user access

Figure 6. - Numerical aerodynamic simulator (NAS) computer capabilities and Lewis remote workstation.

NUMERICAL STUDY OF COMBUSTION PROCESSES IN AFTERBURNERS

Zhou Xiaoqing
Chinese Aeronautical Establishment
Beijing, People's Republic of China

and

Zhang Xiaochun
Shenyang Aeroengine Research Institute
Shenyang, People's Republic of China

Mathematical models and numerical methods are presented for computer modeling of aeroengine afterburners. A computer code GEMCHIP is described briefly. The algorithms SIMPLER, for gas 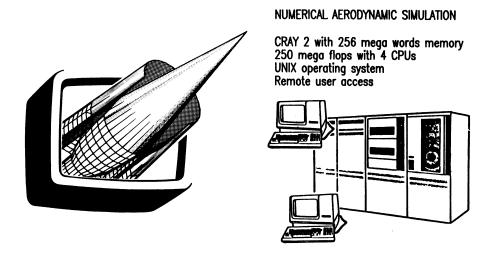flow predictions, and DROPLET, for droplet flow calculations, are incorporated in this code. The block correction technique is adopted to facilitate convergence. The method of handling irregular shapes of combustors and flameholders is described. The predicted results for a low-bypass-ratio turbofan afterburner in the cases of gaseous combustion and multiphase spray combustion are provided and analyzed, and engineering guides for afterburner optimization are presented.

INTRODUCTION

Thus far the design and development of air-breathing engine combustors have been based mainly on ad hoc tests. But the past 10 years have seen a boom of numerical fluid mechanics and combustion. The computer modeling technique is beginning to establish itself in territory which has been dominated exclusively by the empirical technique. It is believed that the combination of numerical modeling with the semi-empirical method and the modern diagnostic technology will greatly promote combustion study and combustor design and development.

The objective of this paper (which is part of the authors' continuing effort to make computer models of multiphase turbulent combustion processes in combustors and furnaces (refs. 1 and 2 and private communication with X. Zhang and H.H. Chiu, University of Illinois at Chicago, 1984)) is to present mathematical models and numerical methods for combustor flows and to apply these methods to the computer prediction of aeroengine afterburner characteristics.

The long-ignored droplet-turbulent-diffusion model plays an important role in droplet dispersion and species distribution. It has now been incorporated in this modeling. The K-ε turbulence model is modified and extended to account for multiphase turbulence effects. A hybrid, finite-rate chemical-reaction model based on a global Arrhenius law and a turbulent mixing-rate model is used judiciously to predict the combustion rate of multiphase premixed turbulent flames. A system of conservation equations of the Eulerian type is used for both gaseous flow and multisized droplet flow predictions. To solve these equations, the authors developed a computer code called GEMCHIP (general, elliptic-type, multiphase, combustion-heat-transfer, and interdiffusion program), in which the SIMPLER algorithm (ref. 3) for gaseous flow prediction

7

and the DROPLET (private communication with X. Zhou and H.H. Chiu, University of Illinois at Chicago, 1983) procedure for droplet flow calculation were incorporated. The block correction technique and the alternating-direction reciprocating-sweep line-by-line TDMA (tri-diagonal matrix algorithm) method was adopted to facilitate convergence of the iteration processes.

The afterburner under study is a low-bypass-ratio turbofan engine augmentor of the axisymmetric type with a bluff body flameholder. The method of simulating the irregularly shaped flow domain and the flameholder configuration is described briefly and the inlet and boundary conditions are presented. The usual wall functions (ref. 4) are used to bridge the near wall regions where local Reynolds numbers are very low.

The numerical results of gas flow, droplet flow fields, and the spray flame structures are presented. A study of the parametric sensitivity of the combustion efficiency is made for both gas combustion and multiphase combustion. Engineering guides are given for afterburner design optimization.

SYMBOLS

C_p specific heat of gas at constant pressure

E activation energy

h total enthalpy

J work-heat equivalence

K turbulent kinetic energy

L latent heat of vaporization

P gas pressure

q heat value of fuel

R_u universal gas constant

r_ℓ droplet radius

T temperature

U,V velocities in X and R directions, respectively

W molecular weight

Y species mass concentration

Γ gamma function; transport coefficient

γ stoichiometric coefficient

ξ turbulence dissipation rate

λ heat conductivity

μ viscosity

ρ density

Φ mixture fraction

Nondimensional numbers:

D_1 first Damkohler number

Ec   Eckert number

Eu   Eulerian number

G_c spray group combustion number

G_d spray group aerodynamic drag number

G_v spray group droplet preheating number

L_{mk} mass fraction of liquid in the mixture

Nu   Nusselt number

Pe   Peclet number

Pr   Prandtl number

Re   Reynolds number

Sc   Schmidt number

τ_{TR} ratio of flow residence time to turbulence dissipation time

ε_R ratio of turbulent kinetic energy to mean flow value

σ turbulent Schmidt/Prandtl number

Subscripts:

b   boiling point

eff   effective

F   fuel

g   gas

k   Kth size group of droplets

ℓ liquid

M,m   mean

o   initial or inlet condition

ox   oxygen

p   product

T,t   turbulent; temperature

MATHEMATICAL FORMULATION

The Eulerian scheme is used to construct elliptic-type conservation equations for both gaseous and droplet phases in two-dimensional, multiphase, combusting, turbulent flows. Nondimensionalization of these equations leads to the following two general forms (ref. 1 and private communication with X. Zhou and H.H. Chiu, University of Illinois at Chicago, 1983):

$$\frac{1}{\bar{r}^i}\left[\frac{\partial}{\partial \bar{X}}\left(\bar{r}^i f_x \bar{\xi} - \bar{r}^i \Gamma_\xi \frac{\partial \bar{\xi}}{\partial \bar{X}}\right) + \frac{\partial}{\partial \bar{r}}\left(\bar{r}^i f_r \bar{\xi} - \bar{r}^i \Gamma_\xi \frac{\partial \bar{\xi}}{\partial \bar{r}}\right)\right] = S_\xi + S_{int} \qquad (1)$$

$$\frac{1}{\bar{r}^i}\left[\frac{\partial}{\partial \bar{X}}(\bar{r}^i \bar{f}_x \bar{\xi}) + \frac{\partial}{\partial \bar{r}}(\bar{r}^i \bar{f}_r \bar{\xi})\right] - \frac{\bar{\xi}}{\bar{r}^i}\left[\frac{\partial}{\partial \bar{X}} - (\bar{r}^i \bar{f}_x) + \frac{\partial}{\partial \bar{r}}(\bar{r}^i \bar{f}_r)\right] = S_{int} \qquad (2)$$

where $\bar{f}_x$ and $\bar{f}_r$ are fluxes in the X and R directions, respectively; Γ_ξ is the transport coefficient for the variable ξ, S_ξ and S_{int} are the inner-phase and interphase source terms, respectively, and i takes the values i = 1 for the cylindrical coordinate and i = 0 for the Cartesian coordinate.

All conservation equations in these two forms are summarized in tables I and II, respectively.

The physical models employed or developed in this study are introduced in the following sections.

Spray Spectrum Model

The generalized Rosin-Rammler function is adopted to derive the size derivative of the droplet number density:

$$f_{n,\ell} = \frac{n_\ell S}{r_{\ell,m}}\frac{\Gamma[(t+4)/S]^{(t+1)/3}}{\Gamma[(t+1)/S]^{(t+4)/3}}\left(\frac{r_\ell}{r_{\ell,m}}\right)^t \exp\left\{-\left(\frac{r_\ell}{r_{\ell,m}}\right)^S\left[\frac{\Gamma[(t+4)/S]}{\Gamma[(t+1)/S]}\right]^{S/3}\right\} \qquad (3)$$

$$n_{\ell,k} = \int_{r_{\ell,k-1/2}}^{r_{\ell,k+1/2}} f_{n,\ell}\, dr_\ell \qquad (4)$$

where S and t characterize the spray spectrum quality, Γ denotes gamma function, and n_ℓ and $r_{\ell,m}$ are the droplet number density and the volume-mean initial droplet radius.

DROPLET Turbulent Diffusion Model

Besides the trajectory motion, droplets also disperse through diffusion caused by the gas turbulence. A droplet diffusion model is formulated (private communication with X. Zhou and H.H. Chiu, University of Illinois at Chicago, 1983 and ref. 5) which takes the following final forms:

$$\sigma_{n\ell} = \psi\sigma_g \tag{5}$$

$$\psi = \left[1 + \sum_{j}^{3} \ell^{h_j}\left(\frac{\rho_\ell}{\rho_g^{3/4}}\frac{\varepsilon}{K} - r_\ell^2\right)^j\right] \tag{6}$$

$$\overline{n_\ell'\vec{V}_g'} = -\frac{\mu_T}{\rho_g\sigma_g}\nabla n_\ell \tag{7}$$

$$\overline{n_\ell'\vec{V}_\ell'} = -\frac{\mu_T}{\rho_g\sigma_{n\ell}}\nabla n_\ell \tag{8}$$

where σ_g and $\sigma_{n\ell}$ are the gas and droplet turbulent Schmidt numbers, respectively.

Modified K-ε Model

The original $K-\varepsilon$ turbulence model is modified to take account of droplet-phase effects. The droplets are assumed to share turbulent kinetic energy with the gas phase. The relationship of turbulent kinetic energies between gas and droplets can be approximated as

$$K_\ell \sim K/\psi^2$$

The modified K-equation is expressed as

$$\nabla \cdot (\theta\rho_g\vec{V}_g K) = \nabla \cdot \left(\theta\frac{\mu_{eff}}{\sigma_K}\nabla K\right) + \theta G_k - \theta\rho_g\varepsilon - \nabla \cdot \int_0^{\dot{m}_\ell} K_\ell\vec{V}_\ell d\dot{m}_\rho \tag{9}$$

The ε-equation remains unchanged.

Hybrid Turbulent Gas Combustion Model

The combustion reaction is supposed to take place in a single step:

$$\gamma_F F + \gamma_{ox} 0 \rightarrow \gamma_p P \tag{10}$$

A hybrid combustion model is adopted; it assumes that the combustion rate is controlled by the slower of two competitive rates of successive subprocesses - the chemical reaction rate and the turbulent mixing rate. The former rate is determined by the Arrhenius law, the latter rate is calculated from the eddy-break-up (EBU) model

$$R_F = - \min \left(|R_{F,EBU}|, \; |R_{F,Ar}| \right) \tag{11}$$

where

$$R_{F,EBU} = -C_R \theta \rho_g K^{1/2} \left[\left(\frac{\partial Y_F}{\partial X_1} \right)^2 + i \left(\frac{\partial Y_F}{\partial X_2} \right)^2 + \left(\frac{\partial Y_F}{\partial X_3} \right)^2 \right]^{1/2}$$

$$R_{F,Ar} = -B_a T_g^\alpha \rho_g^2 Y_F Y_{ox} \exp(-E/R_u T_g)$$

NUMERICAL METHODS

A 42 by 38 staggered grid system is superimposed on the flow domain. The previously mentioned two general forms of nonlinear partial differential equations are then discretized into their finite difference counterparts by using the control volume scheme and the primitive variables of pressure and velocity. The power law scheme (ref. 3) is adopted to determine combined diffusion/convection fluxes. The SIMPLER procedure is employed to predict gaseous flow fields, it reduces computer time by 30 to 50 percent in comparison with the popular SIMPLE procedure. The DROPLET procedure is used for calculating droplet flow fields. The alternating-direction double-reciprocating-sweep line-by-line TDMA method is adopted to solve simultaneous algebraic equations iteratively. The block correction technique is used to facilitate convergence. The usual wall function method is employed to bridge the near wall regions where the laminar viscosity effect is quite strong. This method is very effective in greatly reducing computer time while obtaining rather satisfactory results. All these methods have been assembled into the computer code GEMCHIP. The main flow chart of GEMCHIP is shown in figure 1.

A droplet-free solution is first obtained through SIMPLER, which provides both final results for the single gas-phase flow and the initial guesses of the gas flow fields for multiphase flow. Then we enter DROPLET to calculate droplet flow fields and the interphase exchanges of mass, momentum, and energy. These quantities are substituted as source terms into SIMPLER, and the gas flow fields are modified. Then we enter DROPLET again. This alternating iterative process continues until all the gas- and droplet-flow equations satisfy the convergence criterion in all grids. The typical iteration number ranges from 40 to 75 for gas-phase burning problems and from 120 to 150 for multiphase burning problems. The corresponding computer times are about 5 and 30 min, respectively, on an IBM 4342 machine.

THE AFTERBURNER STUDIED

Figure 2 shows a low-bypass-ratio turbofan afterburner in which the computer modeling is made. The afterburner consists of a cone-type diffuser/mixer, a cylindrical combustion section, and a single-ring bluff-body flameholder. A cylindrical partition board separates the cold fan flow from the hot core flow. The temperature and velocity are 350 K and 80 m/sec in the fan flow and 600 to 800 K and 60 to 200 m/sec in the core flow. The liquid fuel is evenly injected in spray form into the core flow, and then the droplets are heated, vaporized, mixed, and combusted with oxygen in the airflow.

Handling of Irregularly Shaped Wall and Flameholder

The curved afterburner wall and the flameholder are simulated by blocking off some of the control volumes of the regular grid system so that the remaining active control volumes form the desired shape. The advantage of this method is that a computer code developed for the nominally regular domain can be adapted to flows of arbitrarily shaped configurations so that there is no need to generate new programs and the time for developing and testing such programs is saved.

The irregular boundary can be represented approximately by a series of rectangular steps (fig. 3). Usually a rather crude representation of the boundary can produce surprisingly good results.

The values of the relevant flow parameters should be given in the blocked-off regions. This is done by using extremely large source terms or by assigning extremely large transport coefficients in these inactive control volumes. These inactive grids also participate in the iteration process.

Boundary Conditions

Appropriate boundary conditions are selected to represent the wall regions of the afterburner. The following assumptions can be realistically made with regard to this kind of selection:

(1) No slip at the wall
(2) Zero turbulent fluctuation at the wall
(3) Adiabatic and impermeable wall

It is reported that the predicted solution is very sensitive to the inlet conditions. For this reason, the inlet profiles should conform to measured values whenever available. Unfortunately, measurements of the profiles of the inlet variables, especially the inlet velocity vectors and the inlet turbulence variables K and ε, are seldom carried out in complex geometries. It is, therefore, reasonable to assume the following profiles (ref. 6):

$$U_g = U_{go}(1 - \bar{r})^n$$

$$V_g = 0$$

$$K = K_0 \left(1 + m(\bar{r})^2\right)$$

$$\varepsilon = \varepsilon_0 \, (K/K_0)^{1.5}$$

where $0.2 \geq n \geq 0$ and $2 \geq m \geq 0$. The variables with subscript o denote values at the centers of core flow or fan flow. The nondimensional radius $\bar{r} = r/R$ for the core flow and $\bar{r} = |r - (R_1 + R_0)/2|/((R_1 + R_0)/2)$ for the fan flow, where R_0 denotes the radius of the partition board and R_1 represents the diffuser's inlet radius.

The inlet profiles of the droplet number densities, temperatures, and velocities vary with the fuel nozzle type and spray quality.

In the axis of symmetry the radial gradients of all droplet-phase variables are taken to be equal to zero.

The exit plane should be located far downstream and outside the recirculation zone so that the local parabolic flow assumption applies and that the calculating domain is isolated from the ambient environment. The only exceptions are the equations for pressure p and for the pressure correction parameter p', since the pressure effect is always two way. The problem is solved by calculating the outlet velocity component in the main flow direction.

RESULTS AND DISCUSSIONS

The objectives of the numerical study are to analyze the shape and the size of recirculation zones at different working conditions, to examine the vaporization process of multisize fuel sprays, to compare the multiphase flame structures with the gas flame structures, and to study the parametric sensitivity of afterburning efficiency.

Recirculation Zones

The gas velocity vector fields inside the afterburner are shown in figures 4 to 6 for gas flow and multiphase flow. The numerical calculations reveal that the recirculation zones in the wake of the flameholder are induced by negative pressure gradients, which, in turn, are caused by gaseous viscosity.

Figures 4 and 5 are pictures of velocity vectors and X-direction velocity component profiles in a gas phase flow. The length of the recirculation zone in the cold flow case is about 2.0 to 3.5 times the flameholder width. It is readily seen from figure 4 and 5 that the wake effect still exists far downstream of the flameholder. Some experimental reports claim that the recirculation zone will become larger and longer in gas combustion cases because of gas expansion and the reduction of the absolute value of the negative pressure behind the flameholder. But this trend is not obvious in this calculation. Research work is under way in this direction.

Figure 7 shows droplet velocity vectors of two size groups in the multiphase afterburning condition. A comparison of the multiphase flow with the gas flow field (fig. 6) shows that the small droplets are capable of reaching

14

velocity equilibrium more quickly than the large droplets. The velocity non-equilibrium in the downstream is somewhat enhanced because the gas is accelerated more rapidly than the droplets. This is especially true for the large droplets. The droplet recirculation zone is obviously smaller than the gas recirculation zone.

Cascading Vaporization

The preheating and vaporization processes of droplets of different size groups are illustrated in figure 8. It is readily seen from the predicted curves that the small droplets (e.g., $\overline{D}_1 = 0.15$) complete the preheating process and initiate the vaporization process much earlier than the large droplets (e.g., $\overline{D}_1 = 1.60$).

The phenomenon of successive initiation of the vaporization of droplets of different sizes in spray is designated as cascading vaporization (ref. 1) since the initial vaporization lines of different size droplets constitute a form of cascade.

Gas Flame and Multiphase Flame Structures

Figures 9(a) and (b) show the temperature field and flame structure of the gas combustion flow. The gas flame structure is rather simple: the flow of the combustible mixture mixes with the fan flow of the cold air, and the flame is stabilized in the recirculation zone close behind the flameholder. There is a "dark" area, which is fuel-deficient, in the wake of the flameholder. This is where the combustion is completed.

The structure of the multiphase flame is very complicated. Calculation reveals that there are three principal combustion modes: (1) pre-evaporating flame, (2) dense spray group flame, and (3) dilute spray group flame. The total fuel-air ratio and the spray group combustion number G_c are the two main parameters determining combustion mode. The G_c is actually the ratio of the characteristic vaporization rate to the convection flow rate and was first proposed by Prof. H.H. Chiu (ref. 7).

Pre-evaporating flame. - The pre-evaporation flame is shown in figure 10. When the G_c number is very large (fine atomization, i.e., the spray consists of an extremely large quantity of small droplets) all the droplets are vaporized at a typical afterburner inlet temperature before they get to the flame zone. The flame structure is similar to that of gas phase combustion.

Dense spray group flame. - If the G_c number is rather large and the fuel-air ratio is also high, dense spray group combustion occurs (fig. 11); this is characterized by the presence of an oxygen-deficient zone, which decreases combustion efficiency. Both types of gas and droplet burning coexist in the flame.

Dilute spray group flame. - This mode occurs at a small G_c number, which is characterized by poor atomization quality and a low fuel-air ratio: that is, there is a small quantity of big droplets. If the droplet size is large enough and droplets concentrate near the central line of the afterburner, the v-type flame shown in figure 12 may appear. This type of flame is unstable.

Figures 13(a) and (b) show, respectively, the axial distributions of afterburning efficiencies in gas-phase and multiphase combustion cases. It is seen that the growth of the combustion efficiency for the multiphase flame has a slower start than that for the gas flame. This difference is caused by the droplet preheating and by vaporization processes. The results also indicate that the smaller the spray group combustion number G_c, the larger the difference.

Parametric Sensitivity Study of Combustion Efficiency

Figure 14 shows the effect of fuel-air ratio on gas-phase combustion efficiency at two different pressures (2.0 kg/cm^2 and 0.5 kg/cm^2). The efficiency curve reaches its peak at an approximately stoichiometric fuel-air ratio in the core flow. At higher pressures, the efficiency peak moves toward richer mixtures and the curve becomes flatter because of the dilution action by the fan flow and the improvement of combustion conditions.

Figure 15 shows the variation of the multiphase combustion efficiency with the fuel-air ratio at two different spray group combustion numbers. With multiphase combustion there is a combustion efficiency peak at an appropriate fuel-air ratio similar to that with gas-phase combustion. With an increase of G_c number, the efficiency peak moves toward leaner mixtures - which means mixtures with a larger number of smaller-sized droplets will have a higher combustion efficiency at a lower fuel-air ratio. The results are also in agreement with the experimental measurements.

Figures 16(a) and (b) show the effect of the inlet gas temperature on combustion efficiencies of gas-phase and multiphase flames. The temperature increase enhances the heat release rate and speeds up droplet vaporization, which, in turn, enhances the combustion efficiencies of both the gas and multiphase flames. But, for obvious reasons, the temperature effect is stronger in multiphase flames.

The effect of inlet gas pressure on combustion efficiency is similar to that of inlet temperature. It is seen from figure 14 that, in the case of gas phase combustion, an increase of gas pressure from 0.5 to 2.0 kg/cm^2 significantly improves combustion. Figure 17 shows the increase of combustion efficiency with gas pressure in a multiphase combustion case. The pressure effect is negligible at pressures greater than 1.3 kg/cm^2.

Figure 18 shows the effect of gas-flow velocity on gas-phase combustion efficiency. An increase in gas velocity results in a decrease in combustion efficiency because of the reduction of the residence time of the gas flow in the afterburner. The higher the velocity, the lower the efficiency. The effect of inlet gas velocity on multiphase combustion efficiency is rather complicated since the velocity affects not only the residence time but also the droplet atomization, vaporization, and spray group combustion number G_c.

CONCLUSIONS

The mathematical models and numerical methods for predicting multiphase turbulent reacting flows, developed in the authors' study of spray group combustion phenomena have been successfully extended and applied to the numerical

study of flow fields and combustion characteristics of a low-bypass-ratio turbofan afterburner. The computer code developed by the authors is versatile and effective in this study. The technique of blocking off relevant control volumes makes it possible for a computer code developed for a regular grid system to be applied to arbitrary flow domains.

The numerical analysis reveals that the size of the recirculation zone behind the flameholder is about 2.0 to 3.5 times its width. The droplet recirculation zone is smaller than the gas recirculation zone and decreases or even disappears with an increase in droplet size.

The calculation also exposes the existence of three principal combustion modes in multiphase combustion. They are the pre-evaporating flame mode, the dense spray group flame mode, and the dilute spray group flame mode. Study of flame structure is useful to afterburner design optimization.

The results reveal the dependence of afterburner combustion efficiency on the fuel-air ratio and on the operating parameters (such as the inlet gas temperature, pressure, and velocity). As for multiphase combustion, which prevails in turbofan afterburners, the spray group combustion number has a significant effect on combustion efficiency and flame structure. It is concluded that afterburners should be designed to work in the optimum spray group combustion number, which is related to the fuel-air ratio and its distribution. Generally speaking, the favorable design has a pre-evaporating flame mode or a dense group combustion mode with an initial fuel distribution capable of keeping oxygen-deficient zones as small as possible.

Although the previously predicted results are in good qualitative agreement with the known facts, accurate diagnostic measurements and detailed experimental verifications are necessary to examine the quantitative agreement and to improve the present models.

REFERENCES

1. Chiu, H.H.; and Zhou, Xiaoqing: Turbulent Spray Group Evaporation and Combustion, 9th International Colloquium on Dynamics of Explosion and Reactive System, Poiter, France, 1983.

2. Zhou, Xiaoqing; and Chiu, H.H.: Spray Group Combustion Processes in Air Breathing Propulsion Combustors, AIAA-83-1323, AIAA/ASME/SAE 19th Joint Propulsion Conference, 1983, Seattle, U.S.A.

3. Patankar, S.V.: Numerical Heat Transfer and Fluid Flow, McGraw-Hill, 1980, U.S.A.

4. Launder, B.E.; and Spalding, D.B.: The Numerical Computation of Turbulent Flows, Computer Method in Applied Mechanics and Engineering, Vol. 3, pp. 269-289, 1974.

5. Ward, P.; Collings, N.; and Hay, N.: A Comparison of Simple Models of Turbulent Droplet Diffusion Suitable for Use in Computations of Spray Flames, ASME-82-WA/HT-2.

6. Khalil, E.E.: Numerical Computations of Turbulent Reacting Combustion Flows, Numerical Method in Heat Transfer, 1981, John Wiley and Sons Ltd.

7. Chiu, H.H.; and Liu, T.M.: Group Combustion of Liquid Droplets, Combustion Science and Technology, 1977, Vol. 17, pp. 127-142.

TABLE I. - THE GOVERNING EQUATIONS IN THE FORM OF EQUATION (1)

(a) Form of equation (1)

Type of equation	$\bar{F}_x$	$\bar{F}_r$	$\bar\xi$	$\bar\Gamma_\xi$	S_ξ	S_{int}
Continuity	$\bar\theta\bar\rho_g\bar U_g$	$\bar\theta\bar\rho_g\bar V_g$	1	0	0	$-\dfrac{G_c}{3}\dfrac{\bar\lambda}{\bar c_p}\sum_{k=1}^{M}\bar r_{\ell,k}^{-3}\dfrac{\partial}{\partial\bar r_{\ell,k}}\left(\dfrac{\bar n_{\ell,k}}{\bar r_{\ell,k}}\overline{Nu}_{\ell,k}\Phi_{r,k}\right)$
Gas phase X-direction momentum	$\bar\theta\bar\rho_g\bar U_g$	$\bar\theta\bar\rho_g\bar V_g$	$\bar U_g$	$\dfrac{2}{Re\theta_0}\bar\mu_{eff}$	$-\dfrac{Eu}{\theta_0}\dfrac{\partial\bar P_g}{\partial\bar X}+\dfrac{2}{Re\theta_0}\left\{\dfrac{\partial}{\partial\bar X}\left[-\dfrac{2}{3}\bar\mu_{eff}\left(\dfrac{\partial\bar U_g}{\partial\bar X}+\dfrac{1}{\bar r}\dfrac{\partial}{\partial\bar r}(\bar r^{-1}\bar V_g)\right)+\bar\mu_{eff}\dfrac{\partial\bar U_g}{\partial\bar X}\right]+\dfrac{\partial}{\bar r^{-1}\partial\bar r}\left(\bar r^{-1}\bar\mu_{eff}\dfrac{\partial\bar U_g}{\partial\bar X}\right)\right\}$	$-\dfrac{G_c}{3}\dfrac{\bar\lambda}{\bar c_p}\sum_{k=1}^{M}\bar r_{\ell,k}^{-3}\bar D_{\ell,k}\dfrac{\partial}{\partial\bar r_{\ell,k}}\left(\dfrac{\bar n_{\ell,k}}{\bar r_{\ell,k}}\overline{Nu}_{\ell,k}\Phi_{r,k}\right)-G_d\cdot\sum_{k=1}^{M}\dfrac{\bar z_g}{1+B_k}\mu\bar n_{\ell,k}\bar r_{\ell,k}(\bar U_g-\bar U_{\ell,k})$
Gas phase R-direction momentum	$\bar\theta\bar\rho_g\bar U_g$	$\bar\theta\bar\rho_g\bar V_g$	$\bar V_g$	$\dfrac{2}{Re\theta_0}\bar\mu_{eff}$	$-\dfrac{Eu}{\theta_0}\dfrac{\partial\bar P_g}{\partial\bar r}+\dfrac{2}{Re\theta_0}\left\{\dfrac{\partial}{\partial\bar r}\left(\bar\mu_{eff}\dfrac{\partial\bar U_g}{\partial\bar r}\right)+\dfrac{\partial}{\bar r^{-1}\partial\bar r}\left[-\dfrac{2}{3}\cdot\bar r^{-1}\bar\mu_{eff}\left(\dfrac{\partial\bar U_g}{\partial\bar X}+\dfrac{1}{\bar r}\dfrac{\partial}{\partial\bar r}(\bar r^{-1}\bar V_g)\right)-2\delta(\bar T)\bar\mu_{eff}\dfrac{\bar V_g}{\bar r^2}\right]+\bar\mu_{eff}\bar r^{-1}\dfrac{\partial\bar V_g}{\partial\bar r}\right\}$	$-\dfrac{G_c}{3}\dfrac{\bar\lambda}{\bar c_p}\sum_{k=1}^{M}\bar r_{\ell,k}^{-3}\bar V_{\ell,k}\dfrac{\partial}{\partial\bar r_{\ell,k}}\left(\dfrac{\bar n_{\ell,k}}{\bar r_{\ell,k}}\overline{Nu}_{\ell,k}\Phi_{r,k}\right)-G_d\sum_{k=1}^{M}\dfrac{\bar z_r}{1+B_k}\mu\bar n_{\ell,k}\bar r_{\ell,k}(\bar V_g-\bar V_{\ell,k})$
Gas fuel conservation	$\bar\theta\bar\rho_g\bar U_g$	$\bar\theta\bar\rho_g\bar V_g$	Y_F	$\dfrac{2\bar\theta}{Re}\dfrac{\bar\mu_{eff}}{\sigma_F}$	(1) Arrhenius Law $\;-D_1\bar\theta\bar T^\alpha\bar\rho_g^{-2}Y_F Y_{ox}\exp\left[-\dfrac{E}{RT_0}\left(\dfrac{1}{\bar T_g}-1\right)\right]$ (2) EBU model $\;-C_R\epsilon_R\bar\rho_g k^{-1/2}\bar\theta\bar\rho_g^{1/2}\left[\left(\dfrac{\partial Y_F}{\partial\bar X}\right)^2+\left(\dfrac{\partial Y_F}{\partial\bar r}\right)^2\right]^{1/2}$	$-\dfrac{G_c}{3}\dfrac{\bar\lambda}{\bar c_p}\sum_{k=1}^{M}\bar r_{\ell,k}^{-3}\dfrac{\partial}{\partial\bar r_{\ell,k}}\left(\dfrac{\bar n_{\ell,k}}{\bar r_{\ell,k}}\overline{Nu}_{\ell,k}\Phi_{r,k}\right)$
Mixture fraction conservation	$\bar\theta\bar\rho_g\bar U_g$	$\bar\theta\bar\rho_g\bar V_g$	Φ	$\dfrac{2\bar\theta}{Re}\dfrac{\bar\mu_{eff}}{\sigma_\Phi}$	0	$-C_\Phi\dfrac{G_c}{3}\dfrac{\bar\lambda}{\bar c_p}\sum_{k=1}^{M}\bar r_{\ell,k}^{-3}\dfrac{\partial}{\partial\bar r_{\ell,k}}\left(\dfrac{\bar n_{\ell,k}}{\bar r_{\ell,k}}\overline{Nu}_{\ell,k}\Phi_{r,k}\right)$

19

TABLE I. - Continued.

Gas energy conservation	$\bar{\theta}\bar{\rho}_g\bar{U}_g$	$\bar{\theta}\bar{\rho}_g\bar{V}_g$	$\bar{h}$	$\dfrac{2\bar{\theta}}{Re}\dfrac{\mu_{eff}}{\sigma_h}$	$2\dfrac{Ec_g}{Re}\bar{\theta}\bar{\mu}_{eff}G_u$ where $G_u=\left[2\left(\dfrac{\partial\bar{U}_g}{\partial\bar{X}}\right)^2+2\left(\dfrac{\partial\bar{V}_g}{\partial\bar{r}}\right)^2+2\left(\dfrac{\bar{V}_g}{\bar{r}}\right)^2\delta(1)+\left(\dfrac{\partial\bar{U}_g}{\partial\bar{r}}+\dfrac{\partial\bar{V}_g}{\partial\bar{X}}\right)^2\right]$	$\dfrac{-G_c\bar{\lambda}}{1-T_{L0}/T_{g0}}\displaystyle\sum_{k=1}^{M}\overline{Nu_{c,k}(T_g-T_{\ell,k})}\,\bar{r}_{\ell,k}\bar{n}_{\ell,k}\delta(T_{\ell,k})$ $-\dfrac{G_c}{3}\overline{(q^0/w_F-L)}\dfrac{\bar{\lambda}}{C_p}\displaystyle\sum_{k=1}^{M}\bar{r}_{\ell,k}^{-3}\dfrac{\partial}{\partial\bar{r}_{\ell,k}}\left(\dfrac{\bar{n}_{\ell,k}}{\bar{r}_{\ell,k}}\overline{Nu_{\ell,k}}\right)$ $\Phi_{r,k}+G_dEc_g\displaystyle\sum_{k=1}^{M}\overline{\dfrac{z\mu\bar{n}_{\ell,k}}{1+B_k}\bar{r}_{\ell,k}\left[(\bar{U}_g-\bar{U}_{\ell,k})^2+(\bar{V}_g-\bar{V}_{\ell,k})^2\right]}$
K-equation	$\bar{\theta}\bar{\rho}_g\bar{U}_g$	$\bar{\theta}\bar{\rho}_g\bar{V}_g$	$\bar{K}$	$\dfrac{2\bar{\theta}}{Re}\dfrac{\mu_{eff}}{\sigma_k}$	$\dfrac{2}{Re\sigma_R}\bar{\theta}\mu-G_u-\tau_{TR}\bar{\theta}\bar{\rho}_g\varepsilon$	$-L_{mR}\displaystyle\sum_{k=1}^{M}\bar{r}_{\ell,k}^{-3}\dfrac{1}{\bar{r}}\left[\dfrac{\partial}{\partial\bar{X}}(\bar{r}^{-1}\bar{n}_{\ell,k}\bar{0}_{\ell,k}\bar{K}_{\ell,k})+\dfrac{\partial}{\partial\bar{r}}(\bar{r}^{-1}\bar{n}_{\ell,k}\cdot\bar{V}_{\ell,k}\bar{K}_{\ell,k})\right]$
ε - Equation	$\bar{\theta}\bar{\rho}_g\bar{U}_g$	$\bar{\theta}\bar{\rho}_g\bar{V}_g$	$\bar{\varepsilon}$	$\dfrac{2\bar{\theta}}{Re}\dfrac{\mu_{eff}}{\sigma_\varepsilon}$	$\dfrac{C_1C_\mu}{\tau_{TR}}\bar{\theta}K\bar{\rho}_gG_u-C_2\tau_{TR}\bar{\theta}\bar{\rho}_g\dfrac{\bar{\varepsilon}^2}{\bar{K}}$	0
G-Equation*	$\bar{\theta}\bar{\rho}_g\bar{U}_g$	$\bar{\theta}\bar{\rho}_g\bar{V}_g$	$\bar{G}$	$\dfrac{2\bar{\theta}}{Re}\dfrac{\mu_{eff}}{\sigma_G}$	$C_{g1}\dfrac{2\bar{\mu}_t}{Re\sigma_\Phi}\left[\left(\dfrac{\partial\bar{\Phi}}{\partial\bar{X}}\right)^2+\left(\dfrac{\partial\bar{\Phi}}{\partial\bar{r}}\right)^2\right]-C_{g2}\tau_{TR}\cdot\bar{\theta}\bar{\rho}_g(\bar{\varepsilon}/\bar{K})\bar{G}$ $\dfrac{G_c}{3\bar{L}_{mR}}\dfrac{\bar{\lambda}}{C_p}\dfrac{\partial}{\partial\bar{r}_{\ell,k}}\dfrac{\partial}{\partial\bar{r}_{\ell,k}}\left(\dfrac{\overline{Nu_{\ell,k}}}{\bar{r}_{\ell,k}}\bar{n}_{\ell,k}\bar{\Phi}_{r,k}\right)$	$\dfrac{G_c}{3}\dfrac{G_c\bar{\lambda}}{C_p}\displaystyle\sum_{k=1}^{M}\bar{r}_{\ell,k}^{-3}\dfrac{\partial}{\partial\bar{r}_{\ell,k}}\left(\dfrac{\overline{Nu_{\ell,k}}}{\bar{r}_{\ell,k}}\bar{n}_{\ell,k}\bar{\Phi}_{r,k}\right)$
Droplet number-density	$\bar{U}_{\ell,k}$	$\bar{V}_{\ell,k}$	$\bar{n}_{\ell,k}$	$\dfrac{2}{Re}\dfrac{\bar{\mu}_t}{\bar{\rho}_g\sigma_\psi}$		0

*G-equation used for turbulent diffusion flame; not mentioned in text.

20

TABLE I. - Concluded.

(b) Form of equation (2)

Type of equation	$\bar{\xi}$	$\bar{F}_x$	$\bar{F}_r$	S_{int}
X-direction droplet moment	$\bar{U}_{\ell,k}$	$\bar{n}_{\ell,k}\bar{U}_{\ell,k}$	$\bar{n}_{\ell,k}\bar{V}_{\ell,k}$	$\dfrac{G_d}{L_{mR}(1+B_k)}\dfrac{Z_x\mu\bar{n}_{\ell,k}}{\bar{r}_{\ell,k}^2}(\bar{U}_g-\bar{U}_{\ell,k})$
R-direction droplet moment	$\bar{V}_{\ell,k}$	$\bar{n}_{\ell,k}\bar{U}_{\ell,k}$	$\bar{n}_{\ell,k}\bar{V}_{\ell,k}$	$\dfrac{G_d}{L_{mR}(1+B_k)}\dfrac{Z_r\mu\bar{n}_{\ell,k}}{\bar{r}_{\ell,k}^2}(\bar{V}_g-\bar{V}_{\ell,k})$
Droplet temperature	$\bar{T}_{\ell,k}$	$\bar{n}_{\ell,k}\bar{U}_{\ell,k}$	$\bar{n}_{\ell,k}\bar{V}_{\ell,k}$	$\dfrac{G_v}{L_{mR}}\dfrac{Cp_o}{C_\ell}\dfrac{\lambda\overline{Nu}_{c,k}\bar{n}_{\ell,k}}{\bar{r}_{\ell,k}^2}(T_g-T_{\ell,k})$

where $C_1 = 1.44$, $C_2 = 1.92$, $C_\mu = 0.09$, $C_R = 1.07$, $C_{g1} = 2.8$, $C_{g2} = 2.0$,

$\sigma_f = \sigma_{ox} = \sigma_\phi = \sigma_h = \sigma_G = 0.7$, $\sigma_g = 0.9$, $\sigma_K = 1.0$, $\sigma_\epsilon = 1.3$

$G_c = 4\pi\,\dfrac{\lambda_o}{Cp_o}\dfrac{n_{\ell o}r_{\ell mo}R_o Nu_{\ell,o}}{\theta_o\rho_{go}U_{go}}$; $\quad G_d = 6\pi\,\dfrac{\nu_o R_o r_{\ell mo}n_{\ell,o}Z_o}{\theta_o\rho_{go}\bar{U}_{go}}$; $\quad G_v = 4\pi\,\dfrac{Nu_{c,o}r_{\ell mo}n_{\ell,o}R_o^2}{\theta_o Pe}$;

$L_{mR} = \dfrac{\rho_\ell}{\rho_g}\dfrac{1-\theta_o}{\theta_o}$; $\quad \tau_{TR} = \dfrac{\epsilon_o R_o}{k_o U_{go}}$; $\quad Pe = \dfrac{R_o Cp_o\rho_{go}}{\lambda_o}\,2U_{go}$; $\quad Re = \dfrac{2U_{go}R_o\rho_{go}}{\mu_o}$;

$Eu = \dfrac{P_{go}}{\rho_{go}U_{go}^2}$; $\quad Ec_g = \dfrac{U_{go}^2}{JCp_o(T_{go}-T_{\ell,o})}$; $\quad D_1 = \dfrac{R_o}{U_{go}}B_a T_o^\alpha\rho_{go}\dfrac{1}{W_{ox}}\exp\dfrac{-E}{R_U T_o}$;

$Re_m = \dfrac{2U_{go}r_{\ell mo}\rho_{go}}{\nu_o}$; $\quad \epsilon_R = \dfrac{K_o}{U_{go}^2}$
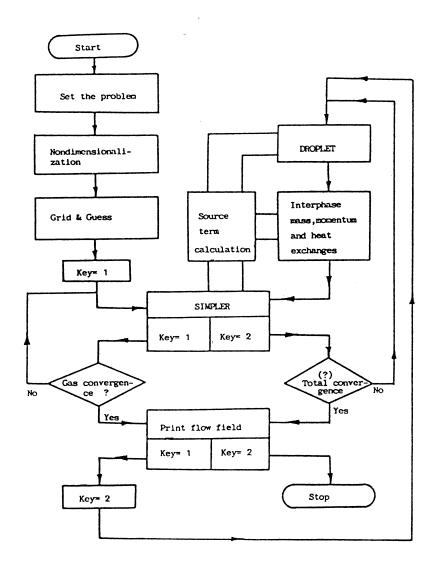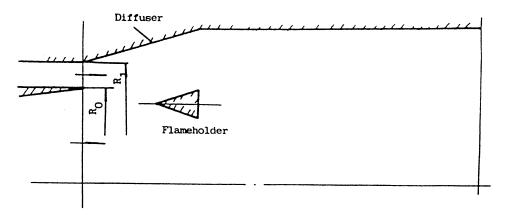
21

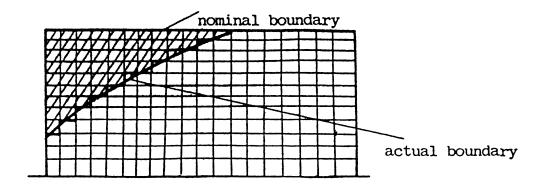Figure 1. – Main flowchart of GEMCHIP.

Figure 2. – Afterburner studied.
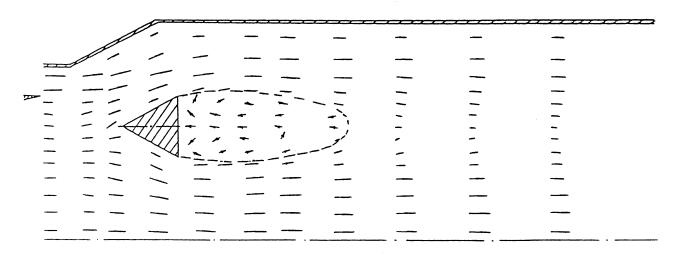
Figure 3. - Blocked-off region in regular grid system.

Figure 4. - Gas velocity vectors of a cold flow.

-2.0   0   +2.0 +4.0
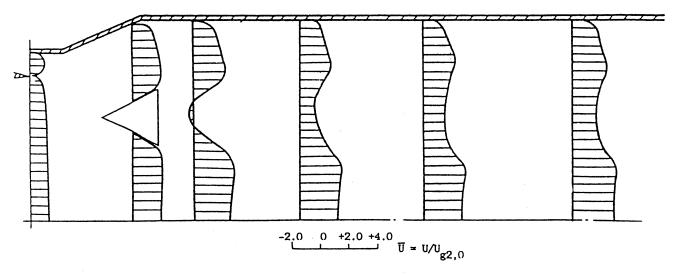
$\bar{U} = U/U_{g2,0}$

Figure 5. - X-Direction velocity component profiles in a gas flow.
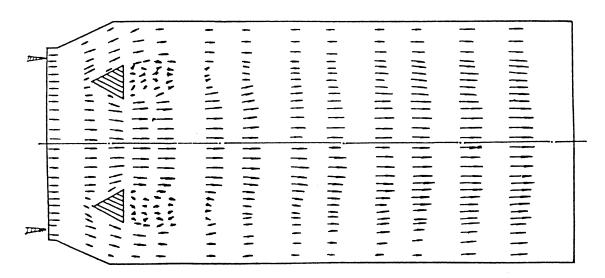
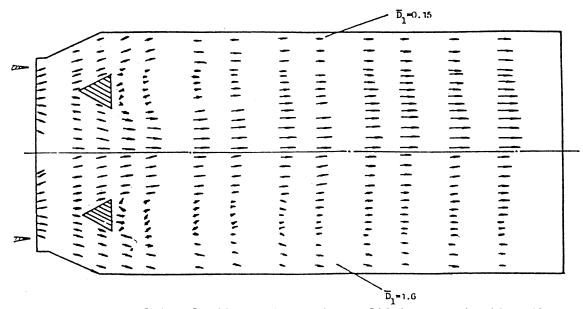Figure 6. - Gas velocity vectors of a multiphase combustion flow.

Figure 7. - Droplet velocity vectors of a multiphase combustion flow.
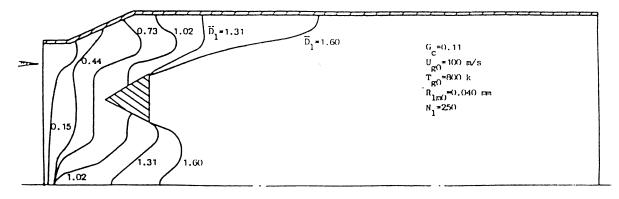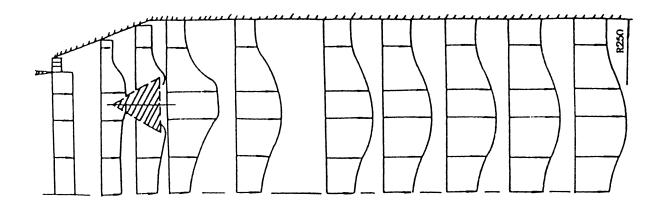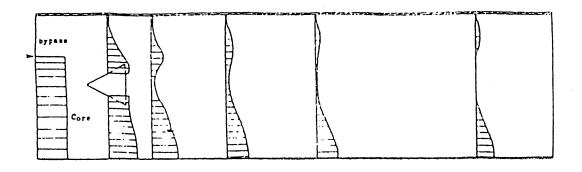

Figure 8. - Cascading vaporization of a multiphase spray flow.

24

(a) Temperature field in a gas combustion flow.

(b) Gas fuel concentration field in a gas phase combustion flow.

Figure 9. - Gas phase combustion flow.
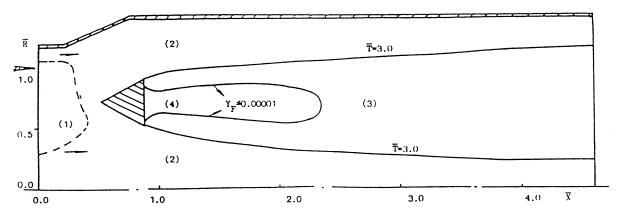
Figure 10. - Pre-evaporating flame mode. Droplet preheating and evaporating zone, (1); gas phase mixing zone, (2); gas phase burning zone, (3); fuel-deficient zone, (4).
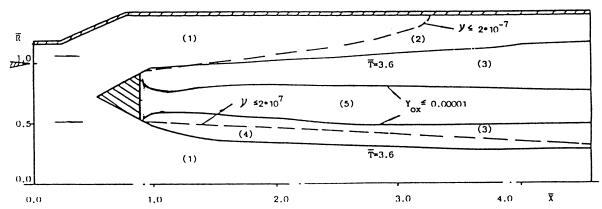
Figure 11. - Dense spray group flame mode. Droplet preheating and evaporating zone, (1); gas phase mixing zone, (2); gas phase burning zone, (3); gas phase and droplet burning zone, (4); oxygen-deficient zone, (5).
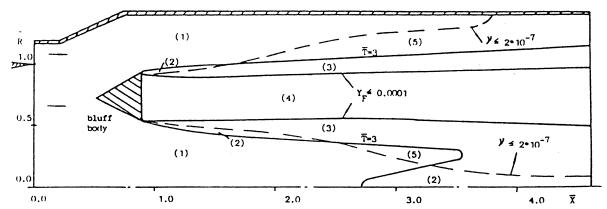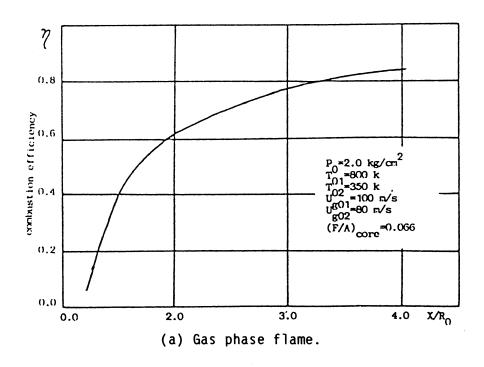
Figure 12. - Dilute spray group flame mode. Droplet preheating and evaporating zone, (1); gas phase and droplet burning zone, (2); gas phase combustion zone, (3); fuel-deficient zone, (4); gas phase mixing zone, (5).

26

(a) Gas phase flame.

(b) Multiphase flame.
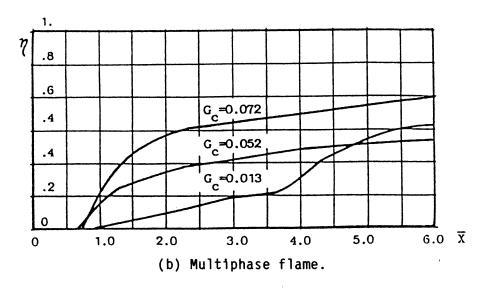
Figure 13. - Axial distributions of combustion efficiency.

27
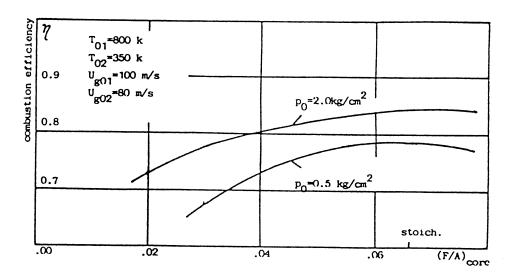
Figure 14. – Relation of gas phase combustion efficiency
with fuel-air ratio and pressure.
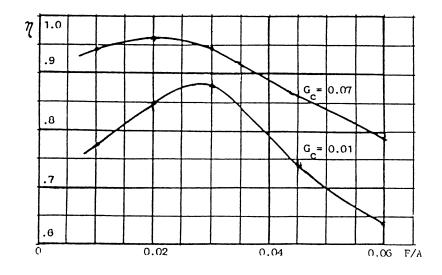
Figure 15. – Relation of multiphase combustion efficiency
with fuel-air ratio and spray group combustion number.
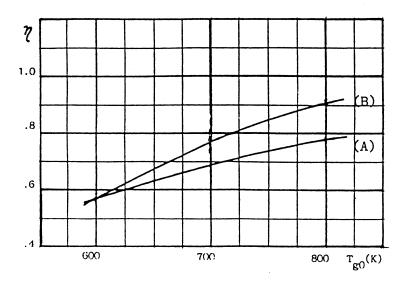
Figure 16. - Effect of inlet temperature on
combustion efficiency. Gas phase flame,
(A); multiphase flame (at better condition),
(B).

T_{g0}=800 k;U_{g0}=100 m/s;F/A= 0.03;G_c=0.03
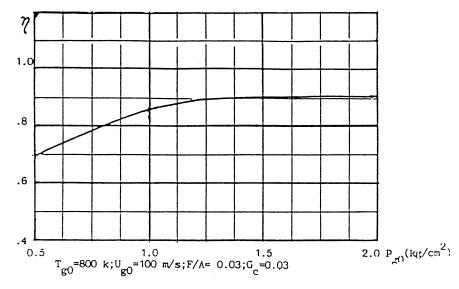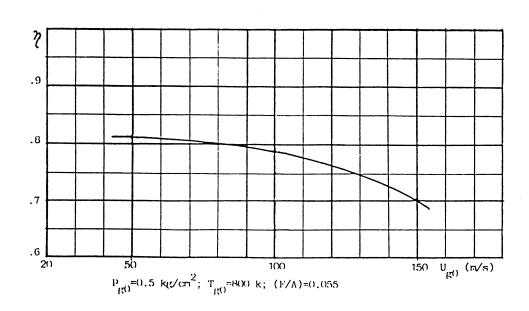
Figure 17. - Effect of inlet pressure on multiphase
combustion efficiency.

Figure 18. – Effect of inlet gas flow velocity on gas combustion efficiency.

MODELING TURBULENT, REACTING FLOW

Russell W. Claus
NASA Lewis Research Center
Cleveland, Ohio

This paper examines several of the approximations or models involved in the development of a numerical combustor flow code. In the first section, the importance of numerical accuracy is illustrated, and the impact that improved-accuracy schemes have on slowing convergence is demonstrated. Solution algorithms that can speed convergence are discussed and some performance features of these algorithms are illustrated. A sample calculation displaying the importance of boundary conditions on a three-dimensional numerical prediction is presented. The inaccuracy of a current turbulence model in highly turbulent (nonequilibrium) regions is described. Finally, the surprisingly good performance of a six-flux model in describing radiation heat transfer is displayed. In all the areas examined, continued research is still needed, but valuable engineering tools are available today.

INTRODUCTION

Three-dimensional combustor calculations involve detailed modeling of several important physical processes. Airflow, chemical reactions, fuel sprays, and turbulence are just a few of the physical processes that must be described. Many of these processes occur on both a molecular and a macroscopic scale. To exactly describe these processes numerically, one must resolve these scales on a computational mesh. And this is clearly beyond current computational resources. To make the computational task tractable, we introduced modeling assumptions. These modeling assumptions limit the generality of the computational flow code, but it is hoped that the dominant physics remain correctly represented.

Modeling assumptions are only the first limit of generality introduced when developing a combustor flow code. A further limit is introduced by the need to approximate the modeled equations before they are solved numerically. This approximation process can significantly affect the accuracy of a model prediction.

In view of all these factors, a combustor designer cannot be expected to fully embrace a computer model prediction. If a clear distinction between modeling errors and errors introduced by the numerical solution algorithm cannot be made, then the designer is left with a very unreliable computational tool.

This paper examines some of the compromises made when developing combustor flow codes and how these compromises affect the accuracy of turbulent flow calculations. To assess the balance of the modeling compromises, we compare a number of sample calculations with experimental data. This paper examines the five areas of numerical accuracy, solution algorithms, inlet boundary conditions, turbulence models, and radiative heat transfer.

The NUMERICAL ACCURACY section focuses on the development of more accurate numerical methods to be used in combustor flow codes. Upwind differencing, which is currently used in these flow codes, introduces an appreciable error (or numerical diffusion) into the calculation. This error may be of such a large magnitude that it obscures the turbulence model used in the calculation. A series of calculations are illustrated which demonstrate the accuracy of a variety of differencing schemes.

An important aspect of improved accuracy is the effect that the differencing scheme has on the rate of convergence. The improved accuracy schemes all appear to require more CPU time to converge. For this reason, the next section discusses solution algorithms. SIMPLE (semi-implicit pressure-linked equations) is one of the most widely used solution algorithms for solving the steady-state form of the Navier-Stokes equations. Although this scheme has proven to be quite effective, its convergence rate can be improved. This paper focuses on two approaches which accelerate convergence by performing corrections that improve the iterative agreement with continuity. These alternate schemes are illustrated in a series of calculations.

A third section examines the importance of inlet boundary conditions. An illustrative example is displayed.

The fourth section discusses turbulence models and reaction closures. Here the more pragmatic approaches to calculating turbulent reactions are illustrated. An eddy-breakup model and a PDF (probability density function) method are described and compared.

Finally, the fifth section examines the accuracy of a radiation heat-transfer model. A six-flux model of radiative heat transfer is described. This model provides only a limited geometric description of the radiation transfer process, but a comparison with experimental data indicates an encouraging level of agreement.

NUMERICAL ACCURACY

The following is a general form of the time-averaged equations that must be solved in a combustor flow code:

$$\frac{\partial}{\partial x}(\rho U \varphi) + \frac{\partial}{\partial y}(\rho V \varphi) - \frac{\partial}{\partial x}\left(\Gamma_\varphi \frac{\partial \varphi}{\partial x}\right) - \frac{\partial}{\partial y}\left(\Gamma_\varphi \frac{\partial \varphi}{\partial y}\right) = S_\varphi \tag{1}$$

where φ can represent U, V, W, $\overline{u_i u_j}$, K, ε, or H; where Γ_φ is the diffusion coefficients (e.g., μ_{eff}); and S_φ is the source term (e.g., $- \partial P/\partial x$). The equation represents convection of a conserved scalar that is subtracted by diffusion terms equal to a source term that could represent a pressure gradient or a source/sink term. These equations are solved by discretizing on a staggered mesh using the finite volume method (fig. 1). The staggered mesh system is used to avoid the pressure-velocity decoupling that can result in a finite volume representation of incompressible flow.

An example of the discretization of a convective term using central differencing is the following:

$$\frac{1}{\Delta x \Delta y} \iint \frac{\partial \rho u \varphi}{\partial x} \, dx \, dy \approx \frac{(\rho u \varphi)_e - (\rho u \varphi)_w}{\Delta x} \tag{2}$$

(Alternate types of differencing are possible and some will be illustrated in the following paragraphs.) Once all the terms have been approximated, like terms are then rearranged in a substitution formula which can be solved using a tri-diagonal matrix algorithm (TDMA) procedure applied in alternate directions (ADI):

$$\alpha_P \varphi_P = \alpha_N \varphi_N + \alpha_S \varphi_S + \alpha_E \varphi_E + \alpha_W \varphi_W + S \tag{3}$$

where, for example,

$$\alpha_N = \left[\frac{\Gamma_n}{\delta_y} - \frac{(\rho V)_n}{2} \right] \Big/ \Delta y_j$$

The source and diffusive terms in these equations are approximated using central differencing which is second-order accurate (Error $\propto O(\Delta x)^2$). The convective terms have typically been differenced using hybrid differencing which reverts to upwind differencing when the absolute value of the cell Reynolds number, or cell Peclet number, is greater than 2, which is the main reason for the loss of numerical accuracy. An example of convective discretization using hybrid differencing is as follows:

$$\frac{\partial u \varphi}{\partial x} \approx \frac{(u \varphi)_e - (u \varphi)_w}{\Delta x} \tag{4}$$

For upwind, with $u > 0$,

$$(u \varphi)_e = u_e \varphi_P$$

and

$$(u \varphi)_w = \frac{1}{2} u_w (\varphi_w + \varphi_P)$$

Since upwind differencing is only first-order accurate, it can introduce an extensive amount of numerical diffusion into the calculation. The virtue of this scheme is that it provides "bounded," stable solutions. Higher order convective schemes invariably yield nonphysical oscillations in the solution. Upwind differencing avoids this, at a considerable loss in accuracy.

To alleviate this problem, NASA has conducted a program to identify and incorporate an improved accuracy differencing scheme into a combustor flow code. Under a portion of this program a variety of differencing schemes were examined in several test calculations. The schemes examined included QUICK (quadratic upstream interpolation) and SUD (skewed upwind differencing). QUICK differencing was developed by Leonard (ref. 1). This scheme improves the accuracy of convective differencing by performing an upwind biased quadratic interpolation. For $u > 0$,

33

$$
\begin{aligned}
(u\varphi)_e &= u_e\left(-\frac{1}{8}\varphi_W + \frac{3}{4}\varphi_P + \frac{3}{8}\varphi_E\right) \\[2mm]
(u\varphi)_W &= u_W\left(-\frac{1}{8}\varphi_{WW} + \frac{3}{4}\varphi_W + \frac{3}{8}\varphi_P\right)
\end{aligned}
\qquad (5)
$$

where grid point locations are as noted on figure 2. This scheme is second-order accurate and can produce nonphysical oscillations in the solution. SUD (skewed upwind differencing) (ref. 2) attains high accuracy by differencing in an upwind manner along the flow streamlines. While maintaining the same formal accuracy as upwind differencing, the truncation error in SUD is smaller. For example:

For $u > 0$ and $V > 0$,

$$
\begin{aligned}
(u\varphi)_e &= u_e\varphi_P \\[2mm]
(u\varphi)_W &= u_W(1 - \alpha)\varphi_W + u_W\alpha\varphi_{SW} \\[2mm]
V &= \text{minimum of } (1, V/2u)
\end{aligned}
\qquad (6)
$$

where grid point locations are as noted in figure 3. As with QUICK, SUD can produce nonphysical oscillations in the solution; therefore, a scheme to "bound" SUD was also examined. This scheme employs the concept of flux-blending (ref. 3), wherein a bounded flux determined from upwind differencing is blended with the unbounded, but more accurate, SUD flux. The main factor is to blend as little of the lesser accurate scheme while still maintaining a properly "bounded" solution. This procedure, called BSUDS, starts from an initial, totally skew-differenced estimate and blends an upwind flux if the solution is out of the range of neighboring values. If the solution is in range (i.e., bounded), then no blending is performed.

An illustration of the accuracy of the upwind, QUICK, and SUD schemes is seen in figure 4. This figure displays the results of a single-point scalar-transport calculation made for various flow angles. All schemes agree with an exact solution (no error) at a zero flow angle; however, at angles greater than zero, each scheme displays some degree of error relating to numerical diffusion. The error displayed by upwind differencing increases with flow angle to a maximum at 45°. The QUICK scheme displays a similar behavior, but the overall error is much less. The SUD scheme displays a maximum error around 15°, but it tends to zero at angles approaching 45°. Both QUICK and SUD display a much higher level of accuracy than upwind.

Although a scalar transport calculation is useful for a general examination of some aspects of differencing scheme performance, a laminar flow calculation is a more complete test. The results of a series of laminar flow calculations from reference 4 are displayed in figure 5. In this figure, axial velocity profiles at a distance of one-half a duct height from the inlet are shown for two different computational meshes. In these calculations, the steepness of the velocity profile indicates accuracy. Steep velocity profiles are exhibited by QUICK and BSUDS; the upwind profiles exhibit a high degree of numerical diffusion. On the coarse mesh, BSUDS appears to be more accurate than QUICK; on the fine mesh, there is not much of a distinction between the two schemes.

An important aspect of improved accuracy is the effect that the differencing scheme has on the rate of convergence. The computational times to converge the system of governing equations in the previous laminar calculations are shown in table I. The convergence times are ratioed to the upwind convergence times to clearly illustrate the computational penalty paid to attain improved accuracy. Generally, the improved accuracy schemes required from 3 to 15 times longer to reach a converged solution. To a degree one can hope that this computational penalty can be offset by using coarse meshes to achieve the same overall level of accuracy. In reality, a relatively fine mesh is needed, even with the high-accuracy schemes. In any case, the need for improved solution algorithms for these more accurate differencing schemes is strongly indicated.

SOLUTION ALGORITHMS

The previous section demonstrated the need for improved solution algorithms. This section examines the widely used SIMPLE algorithm and two modifications to this scheme. These schemes cover only a small portion of the wide range of methods to accelerate solution convergence. Vectorization, direct-solution methods, and multigrid methods - to list just a few - are all areas of active research that are certain to yield much greater computational benefits in the near future.

In the SIMPLE algorithm, a guessed pressure field is inserted into the discretized momentum equations to obtain a velocity field. The pressure field is corrected by an equation which is derived through a combination of the continuity and momentum equations. The velocity field is then updated and is used in the solution of the equations for k, ε, and φ. The corrected pressure field is treated as the guessed pressure field, and the procedure is repeated until a converged solution is obtained.

The following velocity correction equation is used in the SIMPLE scheme for u at point e:

$$A_e u_e' = \sum_{nb} \underline{A_{nb} U_{nb}'} + (P_P' - P_E')A_e \tag{7}$$

Primes indicate corrections to old values. The underlined term, which represents the influence of corrected pressures on neighboring velocities, is neglected in the SIMPLE algorithm. The converged solution is unchanged by the exclusion of this term since, for the steady-state solution, the corrections go to zero. Neglecting terms, however, does force the use of low underrelaxation factors, which can slow convergence.

The SIMPLER algorithm improves on the SIMPLE scheme by including the previously neglected terms when calculating the pressure field. The calculation sequence starts with a guessed velocity field. An equation that solves for the pressure field (using the terms ignored in the SIMPLE scheme) is calculated from the guessed velocity field. This pressure field is then used to solve the discretized momentum equations to obtain a velocity field. The velocity field is corrected in a manner similar to the SIMPLE velocity correction. This velocity field is then treated as the guessed velocity field, and the iteration procedure is repeated until convergence is reached.

Because additional equations are solved, each iteration through the SIMPLER routine involves more computational time than an iteration step through SIMPLE. However, higher underrelaxation factors can be applied in the SIMPLER routine, thereby accelerating convergence.

The PISO scheme also takes into account the terms neglected in the SIMPLE code, but in a different manner. The PISO routine mimics the SIMPLE approach until the end of the first iteration. At this point, the PISO scheme employs an equation containing the neglected terms to correct the pressure and velocity field to more closely agree with continuity. Again, this procedure is repeated until the solution converges. In this manner, the PISO code allows for higher underrelaxation factors to accelerate convergence.

The performance of these various solution schemes is displayed in figure 6. As an example, the convergence times for a 38-by-38 grid point calculation are plotted as a function of underrelaxation factor (fig. 6(a)). When a reasonably large underrelaxation factor is used, SIMPLER or PISO converge about twice as fast as SIMPLE. In addition, SIMPLER and PISO converge over a larger range of underrelaxation factors than SIMPLE. From an engineering standpoint, improving the "robustness" of a computational scheme is often just as important as accelerating convergence. The computational benefit of using SIMPLER and PISO for fine-mesh calculations is displayed in figure 6(b). The greater the number of mesh points used in the calculation, the greater the benefit of SIMPLER or PISO over SIMPLE. For example, a calculation of approximately 3300 grid points converges three times faster using PISO or SIMPLER than it does using SIMPLE. This is a savings of about 600 CPU seconds. The 1440 grid points calculation demonstrated a savings of only about 100 CPU seconds.

INLET BOUNDARY CONDITIONS

In any calculation of a complex, three-dimensional turbulent flow, the boundary conditions that are needed in the calculation are frequently unknown or unmeasured. The use of inappropriate values at the computational boundary can sometimes be the main limit to the calculation's predictive capability. This error can sometimes be more important than numerical accuracy or turbulence model considerations. Figure 7 shows an example of a three-dimensional jet-in-crossflow calculation using alternate boundary conditions. In one calculation, the jet orifice flow was specified as having a uniform plug flow at a position two jet diameters upstream of the orifice outlet. This allowed the flow to distort as it exited the orifice outlet. The second calculation specified a uniform plug flow at the orifice outlet. The resulting axial velocity profiles are compared with experimental data in figure 8. Somewhat surprisingly, the uniform boundary condition at the orifice compared more favorably with experimental data than the theoretically more correct distorted profile. This should not be interpreted as an endorsement of the use of uniform-plug-flow boundary conditions for these types of flows. Indeed, there is some indication of experimental error (ref. 5). This example is meant only to illustrate that unmeasured or unknown boundary conditions can significantly affect a numerical calculation.

TURBULENCE MODELS

Although a great deal of progress is being made in solving the three-dimensional, time-dependent Navier-Stokes equations in large-eddy or direct

numerical simulations, practical engineering calculations currently require the introduction of some form of turbulence modeling. These models are based on either Reynolds or Favre averaging of the exact Navier-Stokes equations, reducing the unsteady form of these equations to an averaged form. Currently, the most widely used turbulence model is the two equation, k-ε, closure. This model relates the Reynolds stresses to a turbulent viscosity through Boussinesq's eddy-viscosity concept:

$$-\overline{\rho u_i u_j} = \rho v_T\left(\frac{\partial U_i}{\partial x_j} + \frac{\partial U_j}{\partial x_i}\right) - \frac{2}{3}\delta_{ij}k \tag{8}$$

where $v_T = C_\mu k^2/\varepsilon$. The turbulent viscosity is related to the kinetic energy k and the dissipation rate ε of the turbulence. The transport equations are then solved for k and ε:

$$\left. \begin{array}{l} U_i \dfrac{\partial k}{\partial x_i} = \dfrac{\partial}{\partial x_i}\left(\dfrac{v_T}{\sigma_k}\dfrac{\partial k}{\partial x_i}\right) + v_T\left(\dfrac{\partial U_i}{\partial x_j} + \dfrac{\partial U_j}{\partial x_i}\right)\dfrac{\partial U_i}{\partial x_j} - \varepsilon \\[4mm] U_i \dfrac{\partial \varepsilon}{\partial x_i} = \dfrac{\partial}{\partial x_i}\left(\dfrac{v_T}{\sigma_\varepsilon}\dfrac{\partial \varepsilon}{\partial x_i}\right) + C_{\varepsilon 1}\dfrac{\varepsilon}{k} v_T\left(\dfrac{\partial U_i}{\partial x_j} + \dfrac{\partial U_j}{\partial x_i}\right)\dfrac{\partial U_i}{\partial x_j} - C_{\varepsilon 2}\dfrac{\varepsilon^2}{k} \end{array} \right\} \tag{9}$$

Where $C_\mu = 0.09$, $C_{\varepsilon 1} = 1.44$, $C_{\varepsilon 2} = 1.92$, $\sigma_k = 1.0$, $\sigma_\varepsilon = 1.3$, $\sigma_\varphi = 0.9$, $k = (1/2)(\overline{u'}^2 + \overline{v'}^2 + \overline{w'}^2)$ and $\varepsilon = C_\mu k^{3/2}/\ell_T$.

The model constants typically employed are those recommended in reference 6. The turbulent Schmidt number σ_φ, is frequently changed from 0.9 to as low as 0.2, depending on the flow being studied.

This two-equation model is based on several assumptions which should be considered when making a numerical calculation. First, the flow is assumed to be close to equilibrium; that is, the flow properties change relatively slowly. Second, the turbulence Reynolds number is assumed to be high. Third, the turbulence is assumed to be isotropic.

The main concern is how well this model, with its inherent assumptions, can represent combustorlike flow fields. Figure 9 displays a comparison between laboratory experiments and numerical predictions of two different isothermal flows. (Figs. 10 and 11 show the locations of the measurements that were made in the flow fields.) In the two-dimensional bluff-body comparison, a major disagreement between measurements and predictions is evident at an axial distance x/D of approximately 0.8. This corresponds to the end of the recirculation zone and causes an incorrect prediction of recirculation zone length. The jet-in-crossflow comparison displays a similar disagreement in the region where the turbulence intensity is high. In this comparison, both hybrid and BSUDS differencing were used in the predictions. It is obvious from the displayed results that numerical accuracy can have a major impact on the comparison with experimental measurements. Hybrid differencing is so completely influenced by numerical diffusion that the qualitative agreement between experiment and calculation, evident in the BSUDS results, is eliminated. The BSUDS results are not grid-independent, but it seems unlikely that this will fully explain the noted disparity.

37

Both of these flow fields display the greatest disagreement between experiment and calculation where the turbulence intensities are the highest. These are regions where the flow field is likely to be far from equilibrium. It is interesting to note that a full Reynolds stress transport (RST) model calculation (presented by McGuirk, J.J., Papadimitriou, C., and Taylor, A.M.K.P. at the Fifth Symposium on Turbulent Shear Flows held at Cornell University, Ithaca, New York, August, 1985) did not yield appreciably better results for a similar flow field. Because both models appear to lose validity around the region of the stagnation point, further model development is needed.

Reaction closures involve a further series of assumptions and approximations. The simplest level of closure is to assume that the reaction is mixing limited and ignore the effect of temporal density fluctuations. The reaction rate can then be related to an eddy lifetime (ε/k) using either a Magnussen-Hjertager or Spaldings eddy-breakup model:

$$\text{Rate} = -S_{m_F} \tag{10}$$

where

$$S_{m_F} = - \rho \, \frac{\varepsilon}{k} \, \min\left[Am_F, \ A \, \frac{Mo_2}{STOIC}, \quad AB \, \frac{M_{pr}}{STOIC + 1}\right]$$

or

$$S_{m_F} = - C_R \, \rho \, \frac{\varepsilon}{k} \, m_{Fu}^2$$

where A, B, and C_R are empirical constants and ε/k can be considered as the eddy lifetime. The density and temperature throughout the flow field can then be established from equilibrium chemistry.

Improved physical realism can be added to this model by introducing the probability density function (PDF) for mixture fraction f. This can account for the unsteady time history of the mixture fraction at each point in space. A nonlinear functional dependence between concentration, temperature, and density occurs as pockets of alternately hot and cold gases are swept past each point in space. Integrating the resultant PDFs allows a determination of the mean properties of the flow.

Figure 12 displays the results of both an eddy-breakup and a PDF model calculation of a planar-mixing layer. The PDF model calculations (ref. 7) demonstrate a significant improvement over the eddy-breakup results. The main factor involved in this improvement is the more physically correct representation of the mixture fraction variation at the point of maximum temperature rise. Of course, both of these models are only as good as the turbulence closure and are wholly inadequate when finite-rate chemistry is important.

RADIATION HEAT TRANSFER

The final topic to be covered in this review concerns radiative heat transfer. Radiation is one of the most significant and least understood heat loads to the combustor liner. It can also play a significant role in the

determination of flame temperature. Any numerical description of a gas turbine combustor must include a radiation heat-transfer model. The six-flux model is the model most commonly used to approximate multidimensional radiative transfer. In this model, differential equations describing the radiative fluxes in positive and negative directions along the principal axis are solved:

$$
\begin{aligned}
\frac{d}{dx}\left(\frac{1}{a+S}\frac{dR^X}{dx}\right) &= a(R^X - E) + \frac{S}{3}(2R^X - R^r - R^Z) \\[2mm]
\frac{1}{r}\frac{d}{dr}\left(\frac{r}{a+S+\frac{1}{r}}\frac{dR^r}{dr}\right) &= a(R^r - E) + \frac{S}{3}(2R^r - R^X - R^Z) \\[2mm]
\frac{1}{r}\frac{d}{d\theta}\left(\frac{1}{a+S}\frac{dR^Z}{r\,d\theta}\right) &= a(R^Z - E) + \frac{S}{3}(2R^Z - R^X - R^r)
\end{aligned}
\qquad (11)
$$

where

$R^{X,r,Z}$ composite fluxes

a absorption coefficient

S scattering coefficient

E σT^4

The main input to this analysis concerns the optical characteristics of the hot gas and soot which must be arbitrarily specified or calculated through a soot formation and oxidation model.

The performance of the six-flux model (ref. 8) is displayed in figure 13. Although the model overestimates the radiative heat transfer in comparison with experimental data, the qualitative trend is quite closely followed. Given the large number of approximations used in the analysis, the agreement with experimental data is quite surprising. The six-flux model does not accurately treat the angular dependence of energy transfer, and the determination of the optical characteristics of the soot cloud still remains as an area of needed research; however, fairly good results appear to be possible in this example.

CONCLUDING REMARKS

Perhaps the most important question any review on numerical modeling can answer is whether or not current computational codes can be usefully employed in the design of combustion devices. Certainly a great deal of research is needed before one can expect quantitative predictive accuracy, and it seems likely that some hardware problems will only be resolved through development testing. The best computer program will never replace the designer's innovative mind, but computer predictions can be used to extend the designer's productivity. New designs can be examined much more rapidly on the computer than in hardware testing. Development costs can be reduced. The promise of this computer-based design methodology is so great that these numerical models will be used despite their deficiencies. Designers should not and probably will

not abandon empirical design tools, but the cautious adoption of numerical models in the design process is a trend which can reap important benefits.

REFERENCES

1. Leonard, B.P.: Stable and Accurate Convective Modelling Procedure Based on Quadratic Upstream Interpolation. Comput. Methods Appl. Mech. Eng., vol. 19, no. 1, June 1979, pp. 59-98.

2. Raithby, G.D.: Skew Upstream Differencing Schemes for Problems Involving Fluid Flow. Comput. Methods Appl. Mech. Eng., vol. 9, no. 2, Oct. 1976, pp. 153-164.

3. Boris, J.P.; and Book, D.L.: Flux Corrected Transport. I. SHASTA, A Fluid Transport Algorithm That Works. J. Comput. Phys., vol. 11, no. 1, Jan. 1973, pp. 38-69.

4. Claus, R.W.; Neely, G.M.; and Syed, S.A.: Reducing Numerical Diffusion for Incompressible Flow Calculations. NASA TM-83621, 1984.

5. Claus, R.W.: Numerical Calculation of Subsonic Jets in Crossflow With Reduced Numerical Diffusion. NASA TM-87003, 1985.

6. Launder, B.E.; and Spalding, D.B.: The Numerical Computation of Turbulent Flows. Comput. Methods Appl. Mech. Eng, vol. 3, no. 2, Mar. 1974, pp. 269-289.

7. Farchshi, M.: Prediction of Heat Release Effects on a Mixing Layer. AIAA Paper 86-0058, Jan. 1986.

8. Srivatsa, S.K.: Computations of Soot and NO_x Emissions From Gas Turbine Combustors. (GARRETT-REPT-21-4309, Garrett Turbine Engine Co.; NASA Contract NAS3-22542.) NASA CR-167930, 1982.

TABLE I. - RATIO OF CONVERGENCE TIMES

FOR VARIOUS DIFFERENCING SCHEMES

WITH UPWIND CONVERGENCE TIMES

USED AS THE STANDARD

Mesh	Upwind	BSUDS	QUICK
Coarse (30 by 22)	1	6.4	3.2
Fine (58 by 38)	1	14.7	15.7
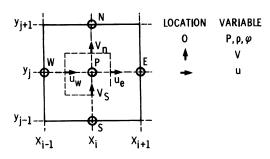
Figure 1. - Staggered mesh system for discretizing equations by finite volume method.
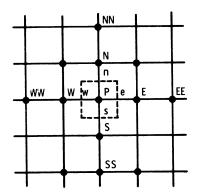
Figure 2. - Staggered mesh system for quadratic upstream interpolation.
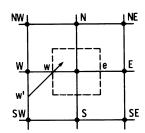
Figure 3. - Staggered mesh system for bounded skew upwind differencing scheme (BSUDS).
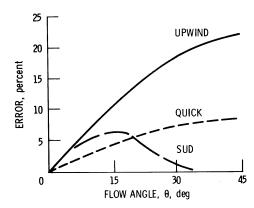
Figure 4. - Accuracy of various differencing schemes for a scalar transport test calculation.

(a) Coarse grid calculations, 30 by 22.

(b) Fine grid calculations, 58 by 38.
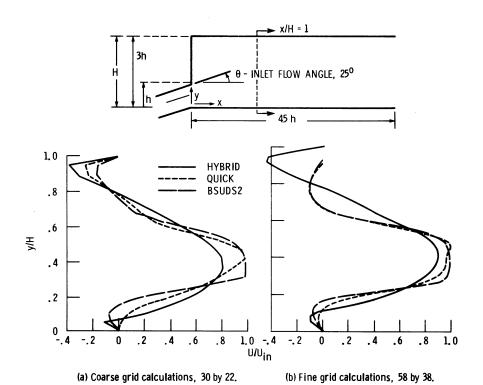
Figure 5. - Laminar flow calculations testing various differencing schemes.

42

(a) For 38 by 38 grid point calculation.

(b) For various computational meshes.
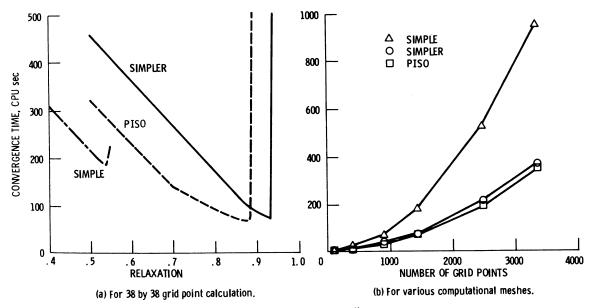
Figure 6. - Convergence times.
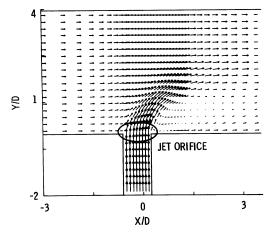
Figure 7. - Three-dimensional jet-in-crossflow calculation.
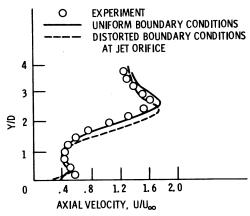
Figure 8. - Calculated axial velocity profiles compared with experimental data.

43

(a) Two-dimensional bluff-body wake.

(b) Three-dimensional jets in crossflow.
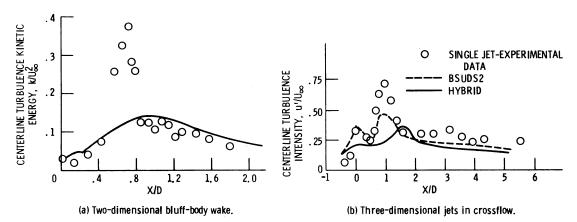
Figure 9. - Comparison of laboratory experiments with numerical predictions of two different isothermal flows.
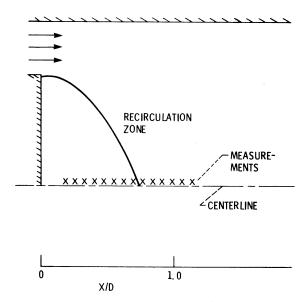
Figure 10. - Two-dimensional bluff-body geometry.
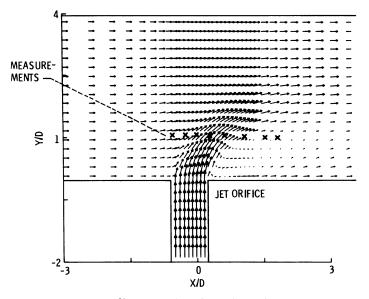
Figure 11. - Three-dimensional jet geometry.

(a) Example - planar mixing layer.

(b) Eddy breakup model.

(c) PDF model.
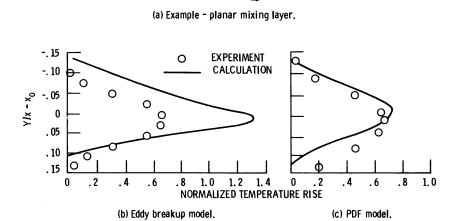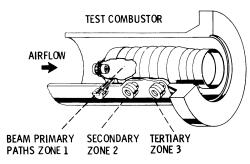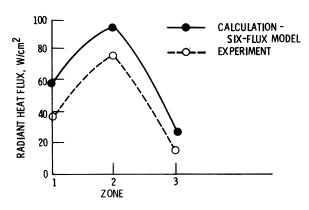
Figure 12. - Results of calculations of a planar-mixing layer.

45

TEST COMBUSTOR

AIRFLOW

BEAM PRIMARY   SECONDARY   TERTIARY
PATHS ZONE 1   ZONE 2   ZONE 3

(a) Schematic drawing of experimental measurement
    locations.

(b) Performance of six-flux
    model.

Figure 13. - Radiative heat transfer test calculation.

EXPERIMENTAL AND ANALYTICAL INVESTIGATION OF THE VARIATION OF SPRAY

CHARACTERISTICS ALONG A RADIAL DISTANCE DOWNSTREAM OF A

PRESSURE-SWIRL ATOMIZER

J.S. Chin, W.M. Li, and X.F. Wang
Beijing Institute of Aeronautics and Astronautics
Beijing, People's Republic of China

The variation of spray characteristics along a radial distance downstream
of a pressure-swirl atomizer was measured by laser light-scattering technology.
An analytical model was developed to predict the variation of spray character-
istics along the radial distance. A comparison of the predicted and experi-
mental data showed excellent agreement. Therefore, the spray model proposed,
although relatively simple, is correct and can be used, with some expansion
and modification of the prepared model, to predict more complicated spray
systems.

INTRODUCTION

The characteristics of the spray formed by an atomizer in a liquid-fueled
combustion device are extremely important to the performance, stability, and
pollutant formation of the combustor. The spray characteristics should be
measured accurately, and a model should be developed to predict the variation
of spray characteristics, droplet trajectory, spray dispersion, and evapora-
tion history. It is also important to understand the influence of various
factors on the measurement of spray characteristics. A comparison between
predicted and measured spray characteristics provides useful insight into
spray combustion. Such research has a significant effect on engineering
applications and on the fundamental understanding of spray combustion.

The authors analyzed the variation of spray characteristics along the
axial distance downstream of a pressure-swirl atomizer. The effect of spray
evaporation on the variation of spray characteristics is discussed in
reference 1 and was presented by J.S. Chin and J.Y. Zhu at this symposium.
(Paper, entitled The Interdependence of Spray Characteristics and Evaporation
History of Fuel Sprays in High Temperature Airflows, was unavailable for
printing at the time of publication.) The influence of downstream distance on
the spray characteristics of pressure-swirl atomizers is caused by the effects
of spray dispersion and drop acceleration or deceleration. This condition is
analyzed in reference 2. These analyses have been partially substantiated by
some experimental data. Until now there have been few experimental data of
the variation of spray characteristics along the radial distance downstream of
the pressure-swirl atomizer. Lee Dodge published his measurement results as
shown in figure 1 (ref. 3). He shows that both the Sauter mean diameter SMD
and drop-size distribution parameter N increase with radial distance. There
is no analysis on this aspect available at the present time.

We are interested in comparing the experimental and predicted values of
the variation of spray characteristics along the radial distance. Therefore,
we carefully measured this variation in a well-defined experimental condition,
developed an analytical model to predict the variation, and then compared the

experimental and predicted data. These comparisons promote our understanding of spray dispersion and the factors influencing drop-size measurement. After we have predicted the simple spray system, we will be able to expand and modify the proposed spray model to extend its capability to more complicated spray systems.

Cao and Chin proposed a flat-fan spray model for the fuel distribution downstream of a plain orifice injector under cross airflow (ref. 4). The model was validated by fuel distribution measured by gas analysis and drop size. It is obvious that, for the validation of a given spray model, the spray characteristics measurement is reliably accurate and much simpler than the fuel distribution measurement. It is this author's intention to validate a spray model by measuring the spray characteristics along the radial distance. The same spray model has also been validated by measuring the spray characteristics along different θ angles (as shown in fig. 5).

TEST APPARATUS, ATOMIZER, AND PARTICLE SIZER

The test section was a rectangular chamber with transparent windows for optical drop-size measurement. The test apparatus included an air system and a fuel system, as shown in figure 2.

The atomizer tested (fig. 3) was a pressure-swirl atomizer taken from an existing aircraft gas-turbine engine. The atomizer had a pilot-fuel flow and a main-fuel flow. In this test we used the pilot-fuel passage. Because the flow rate is relatively lower with pilot-fuel flow, the obscuration was in the right range.

A Malvern drop-size analyzer model 2200 was used. The principle of the particle sizer is shown in figure 4. The instrument was set on the Rosin-Rammler distribution mode. The direct results from the instrument are the characteristic diameter $\bar{D}$ and the drop-size distribution parameter N in the R-R distribution which is expressed by

$$Q = 1 - \exp\left[-\left(\frac{D}{\bar{D}}\right)N\right] \tag{1}$$

where Q is the fraction of the total volume contained in drops that have a diameter less than D.

The Sauter mean diameter SMD can be obtained from

$$SMD = \bar{D}\left[\Gamma\left(1 - \frac{1}{N}\right)\right]^{-1} \tag{2}$$

where Γ is the gamma function.

EXPERIMENTAL RESULTS

During drop-size measurement tests, the laser light beam was first adjusted so that it was in the same horizontal plane as the central line of the atomizer and that it was perpendicular to this central line. At this

48

position (defined as the y = 0 position), the spray characteristics were measured. Then the Malvern particle sizer was put on some size blocks of known dimension. This changed the height of the laser beam so that the radial distance where the particle sizer measured the drop size was changed. The summation of the size block was defined as the radial distance y. The dimensions of the blocks chosen were 2.5, 3.0, and 10 mm. Thus, the following radial distance y could be obtained by different combinations of the size blocks: y = 0, 5.5, 10.0, 15.5, 20.0, 25.5, and 30.0 mm. The experimental results are shown in figures 6 to 13. From these figures it is clear that the Sauter mean diameter and drop-size distribution parameter increase with radial distance until the edge of the spray has been reached. The experimental results obtained by the present authors are quantitatively in good agreement with Lee Dodge's results. The obvious explanation of the measured results shown in figures 6 to 13 is that with larger radial distances the possibility of the laser light beam meeting the large drops is greater than it is with smaller radial distances. This shows that when we measure the drop size it is necessary to take a sample that is representative of the spray formed; however, it is impossible to define the sample which would fully represent the spray. The most reasonable sample can be obtained by measuring the spray at the y = 0 position.

Comparing figure 6 with 8 and 7 with 9 shows that, at a higher airflow velocity, the change of spray characteristics along the radial distance is weaker. A comparison of figures 8, 10, and 12 and of 9, 11, and 13 shows that, with a lower pressure drop across the nozzle, the change of the spray characteristics along the radial distance is weaker. These results tell us that when the spray is expanded less radially the change of spray characteristics is also flatter. The reverse is also true.

The experimental data obtained in this way were used to check the proposed spray model.

PHYSICAL MODEL

The spray formed by a pressure-swirl atomizer is shown in figure 5. The physical model was proposed with the following assumptions:

(1) The atomization process is completed as soon as the fuel leaves the atomizer nozzle; that is, droplets of different sizes start their movement at the nozzle exit. Droplets of different sizes have the same initial velocity. Because it is suitable to use a cylindrical coordinate system to describe droplet motion, the tangential velocity and the radial velocity component can be combined and treated as one velocity component.

(2) The airflow is uniform.

(3) The air is at ambient temperature, so droplet evaporation can be neglected.

(4) The influence of different droplet velocities on the drop-size measurements made by the Malvern particle sizer is neglected.

The initial drop-size distribution can be expressed by $\bar{D}_0(SMD_0)$ and N_0 with the initial volume fraction $(dQ/dD)_0$ as

$$\left(\frac{dQ}{dD}\right)_0 = \frac{N_0}{D_0} \left(\frac{D}{D_0}\right)^{N_0-1} \exp\left[-\left(\frac{D}{D_0}\right)^{N_0}\right] \tag{3}$$

At a downstream distance x, the droplets of diameter D move from the origin and then distribute themselves on a circumference of radius $R(D)$ while the laser light beam of diameter d_j only meets some of these droplets:

$$\left(\frac{dQ}{dD}\right)_0 \frac{2(\varphi_2 - \varphi_1)}{2\pi} \tag{4}$$

where

$$\varphi_1 = \arcsin \frac{y_0 - \frac{1}{2} d_j}{R(D)} \tag{5}$$

$$\varphi_2 = \arcsin \frac{y_0 + \frac{1}{2} d_j}{R(D)} \tag{6}$$

The definitions of φ_2 and φ_1 are shown in figure 5. When

$$y_0 - \frac{1}{2} d_j \leq R(D) \leq y_0 + \frac{1}{2} d_j$$

then

$$\varphi_2 = \frac{\pi}{2}$$

where y_0 is the radial distance and d_j the diameter of the light beam.

The summation of the liquid fraction of the droplets of various diameters passing through the laser light beam is given by

$$\int_{D_{min}}^{D_{max}} \left(\frac{dQ}{dD}\right)_0 \frac{\varphi_2 - \varphi_1}{\pi} \, dD \tag{7}$$

The minimum diameter D_{min} that the laser light beam can see is determined by

$$R(D_{min}) = y_0 - \frac{1}{2} d_j$$

That is, at the downstream distance x, if $R(D) < y_0 - 1/2 \, d_j$, this droplet will not pass through the laser light beam. The relationship $R(D)$ can be determined by the droplet motion equation. The maximum diameter that may exist in the spray, can be approximated by

$$D_{max} = 3.5(SMD)$$

If we take the droplets within the laser light beam as a new spray (a sample), the liquid volume fraction of droplets of diameter D in this new spray (sample) is

$$\frac{dQ'}{dD} = \frac{\left(\frac{dQ}{dD}\right)_o \frac{\varphi_2 - \varphi_1}{\pi}}{\int_{D_{min}}^{D_{max}} \left(\frac{dQ}{dD}\right)_o \frac{\varphi_2 - \varphi_1}{\pi} \, dD} \tag{8}$$

Since this is actually the drop-size distribution of the sample (new spray) the laser light beam is to measure, we may obtain Q' as a function of D. Then, if we assume that the Rosin-Rammler (R-R) distribution can be used for data fitting the sample (new spray), we obtain new SMD' and N' for the sample. These values, SMD' and N', change with the distance y_o. If we delete the prime, we obtain the functional relationships $SMD = f(y)$ and $N = f(y)$.

DROPLET TRAJECTORY EQUATION

If we use a coordinate system which is moving with the airflow, then the droplet motion equation is

$$m \frac{dw}{dt} = -C_D \frac{\rho_a w^2}{2} s \tag{9}$$

where

m droplet mass, $(\pi/6)\rho_\ell D^3$

ρ_ℓ liquid density

w droplet relative velocity

C_D droplet drag coefficient, $C_D = 15/\sqrt{Re}$ for $Re = \rho_a DW/\mu_a$

ρ_a density of air

μ_a viscosity of air

Equation (9) can be rewritten as

$$\frac{d\left(\frac{W}{W_o}\right)}{dt} = -\frac{45}{4} \frac{(\rho_a \mu_a W_o)^{1/2}}{\rho_\ell} D^{-3/2} \left(\frac{W}{W_o}\right)^{3/2} \tag{10}$$

where W_o is the droplet initial relative velocity.

51

Integrating equation (10) yields

$$\frac{W}{W_0} = (Bt + 1)^{-2} \tag{11}$$

where

$$B = \frac{45}{8} \frac{\left(\rho_a \mu_a W_0\right)^{1/2}}{\rho_\ell} D^{-3/2} \tag{12}$$

We know that, at the downstream distance x, droplet velocity, air velocity, and the relative velocity of these two have the following relations:

$$V_x = V_a + (V_{xo} - V_a)\frac{W}{W_0}$$

and

$$V_R = V_{Ro} \frac{W}{W_0} \tag{13}$$

where V_x and V_R are the axial and radial velocity components of the droplet, and V_{xo} and V_{Ro} are the initial values of these components. Thus, we obtain the droplet trajectory equations

$$\left. \begin{array}{l} x = V_a t + (V_{xo} - V_a) \displaystyle\int_0^t \frac{W}{W_0}\, dt \\[20pt] R = V_{Ro} \displaystyle\int_0^t \frac{W}{W_0}\, dt \end{array} \right\} \tag{14}$$

From equation (11) we have

$$\int_0^t \frac{W}{W_0}\, dt = \frac{t}{Bt + 1} \tag{15}$$

From equations (14) and (15) we have the radial position (droplet size D) at downstream distance x:

$$R(D) = V_{Ro} \frac{1}{B + \frac{1}{t}} \tag{16}$$

52

Time t can be determined by

$$t = \frac{XB - V_{xo} + \left[(XB - V_{xo})^2 + 4V_a BX\right]^{1/2}}{2V_a B} \tag{17}$$

where B is determined by equation (12).

From equations (14) and (15), by substituting x and $R_{min} = R(D_{min}) = y_o - (1/2) d_j$, we obtain

$$D_{min} = \left[\frac{45}{8} \frac{\left(\rho_a \mu_a W_o\right)^{1/2}}{\rho_\ell} \frac{\frac{V_{xo} - V_a}{V_{Ro}} R_{min}^2 - XR_{min}}{V_{xo} R_{min} - xV_{Ro}}\right]^{2/3} \tag{18}$$

CALCULATION METHOD AND RESULTS

In order to calculate the variation of spray characteristics along the radial distance the following parameters must be known:

(1) Axial distance x
(2) Pressure drop across the nozzle ΔP_ℓ
(3) Fuel properties and physical properties of air
(4) Atomizer spray cone angle
(5) Initial spray characteristics $(SMD)_0$ and N_0

The calculation method used in this paper may be summarized as follows:

(1) Use the measured SMD and N values at y = 0 and the downstream distance x as the approximation of $(SMD)_0$ and N_0. We know that there is some difference between $(SMD)_0$ and $SMD_{y=0}$, N_0, and $N_{y=0}$ (ref. 2). So far these are the most reasonable approximate values that can be used.

(2) Calculate the initial droplet velocity $V_\ell = \mu(2\Delta p_\ell/\rho_\ell)^{1/2}$ where μ is the flow coefficient for the pressure drop. For the atomizer used in the present research, the spray angle is close to 90°; therefore,

$$\left.\begin{array}{l} V_{xo} = 0.566 \left(\frac{2\Delta p_\ell}{\rho_\ell}\right)^{1/2} \\[4mm] V_{Ro} = 0.566 \left(\frac{2\Delta p_\ell}{\rho_\ell}\right)^{1/2} \end{array}\right\} \tag{19}$$

(3) Determine the D_{min} value for a different y_0 value by equation (18). We assume $D_{max} = 3.5(SMD)$.

(4) Use the Simpson method to solve equation (8), with the R(D) value calculated from equations (16) and (17).

53

(5) Determine the integration

$$Q' = \int_{D_{min}}^{D} \left(\frac{dQ'}{dD}\right) dD$$

From this, we are able to obtain a set of the data of Q' and D.

(6) Assume that Q' can be fitted by R-R distribution:

$$Q' = 1 - \exp\left[-\left(\frac{D}{\overline{D}'}\right)^{N'}\right]$$

By using the least-square method, we can obtain $\overline{D}$ and N'; then, SMD' and N' can be calculated. These SMD' and N' values are plotted against y in figures 6 to 13.

The results of the calculations for different airflow velocities and for the nozzle pressure drop are shown in figures 6 to 13. These are compared with the corresponding experimental data. It is obvious that the predictions are in excellent agreement with the experimental results.

CONCLUDING REMARKS

In the present study, droplet evaporation was neglected (discussed by J.S. Chin and J.Y. Zhu in the unpublished paper cited previously), and it is not difficult to take into consideration the effect of droplet evaporation.

After this model has been validated, it is relatively simple to predict the fuel distribution downstream of a pressure-swirl atomizer (ref. 6).
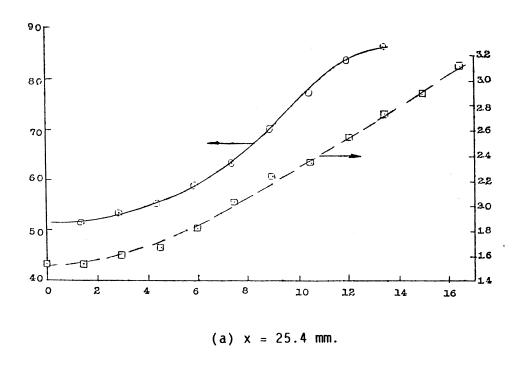
One interesting point that was noticed from the experiments and the analysis was that the larger droplets are always at the spray edge. Because the ignition spark plug is also always positioned close to the spray edge, the spark might meet the larger droplets, which would harm the ignition.

We measured the variation of spray characteristics along the radial distance was by laser light-scattering technology. And we found that the prediction based on the proposed spray model was in excellent agreement with the experimental data.

REFERENCES

1. J.S. Chin; R. Durrent; and A.H. Lefebvre: The Interdependence of Spray Characteristics and Evaporation History of Fuel Sprays. Transactions of ASME Journal of Engineering for Gas Turbine and Power. July, 1984.

2. J.S. Chin; D. Nickolaus; and A.H. Lefebvre: Influence of Downstream Distance on the Spray Characteristics of Pressure-Swirl Atomizers. ASME 85-GT-138, Transactions of the ASME, Journal of Engineering for Gas Turbine and Power, Jan., 1986.

3. L.G. Dodge; and C.A. Moses: Mechanisms of Smoke Reduction in the High Pressure Combustion of Emulsified Fuels. Vol. 1, Construction of Apparatus and Preliminary Experiments, Yearly Progress Report No. 1, Sept. 29, 1980 to Sept. 29, 1981.

4. M.H. Cao; J.S. Chin; et al.: Semi-Empirical Analysis of Liquid Fuel Distribution Downstream of a Plain Orifice Injector Under Cross-stream Air Flow. Transactions of the ASME, Journal of Engineering for Power, Oct., 1982.

5. J.S. Chin; X.F. Wang; W.M. Li; and A.H. Lefebvre: The Influence on Measured Spray Characteristics of Variations in the Radial and Angular Positions of the Sampling Laser Beam. Spring Technical Meeting Central States Section/The Combustion Institute, Paper CSS/CI 86-5C1, 1986.

6. J.S. Chin; and A.H. Lefebvre: Prediction of Liquid Fuel Distribution Downstream of a Swirl Atomizer in Flowing Air. Spring Technical Meeting, Central States Section/The Combustion Institute, Paper CSS/CI 83-20, 1983.

(a) x = 25.4 mm.

(b) x = 50.8 mm.
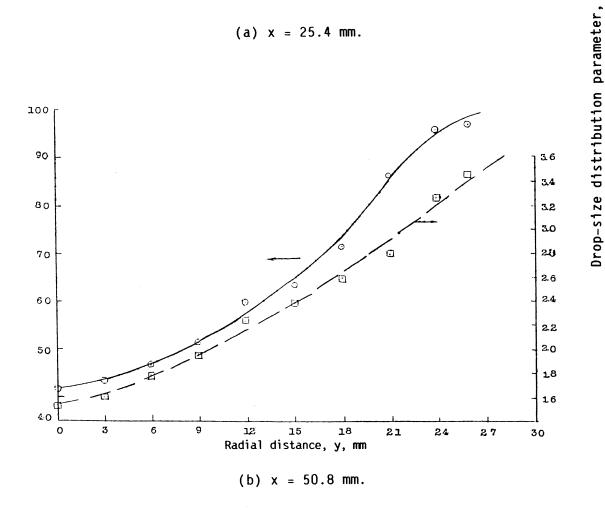
Figure 1. – Lee Dodge's measurement results (ref. 4). Atomizer pressure drop, ΔP, 100 lb/in.^{2}.
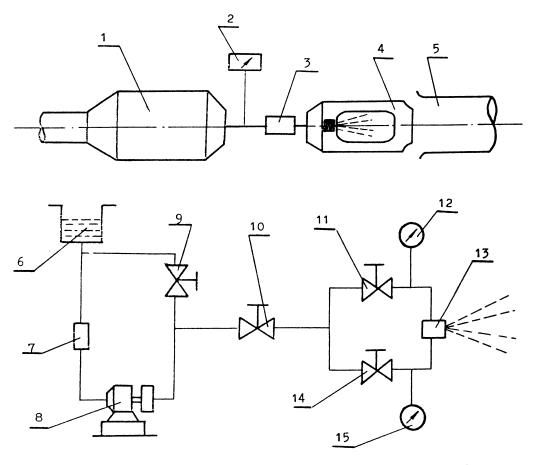
Figure 2. - Experimental system. Plenum chamber, 1; air
temperature, 2; air flowmeter, 3; test section, 4; exhaust
pipe, 5; fuel tank, 6; filter, 7; pump, 8; return valve, 9;
valve, 10; pilot-fuel flow valve, 11; pressure gauge, 12;
atomizer, 13; main-fuel flow valve, 14; pressure gauge, 15.
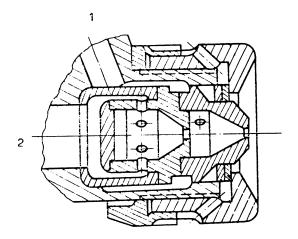
Figure 3. - Atomizer. Pilot-fuel
flow, 1; main-fuel flow, 2.
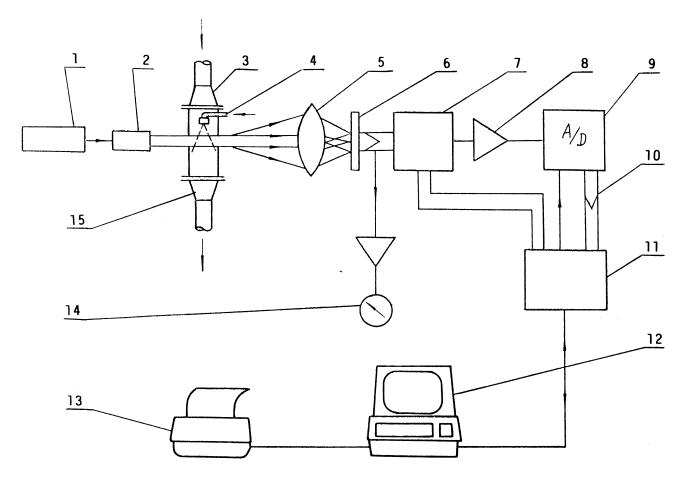
Figure 4. - Laser drop particle sizer. Laser, 1; beam expander, 2; test
  section, 3; fuel nozzle, 4; lens, 5; photo detector, 6; solid valve, 7;
  amplifier, 8; A/D converter, 9; data transfer, 10; interface, 11;
  computer, 12; printer, 13; micro tune, 14.
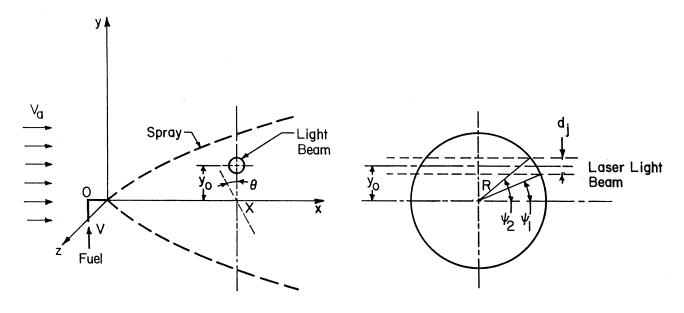
Figure 5. - Physical model.

58
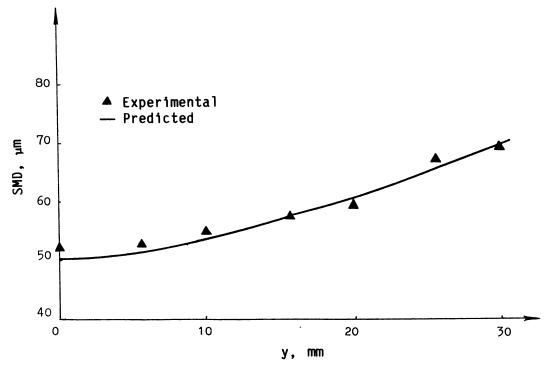
Figure 6. - Variation of Sauter mean diameter (SMD) along radial distance (y) for x = 70 mm, V_a = 9 m/sec, and ΔP = 12 kg/cm^2.
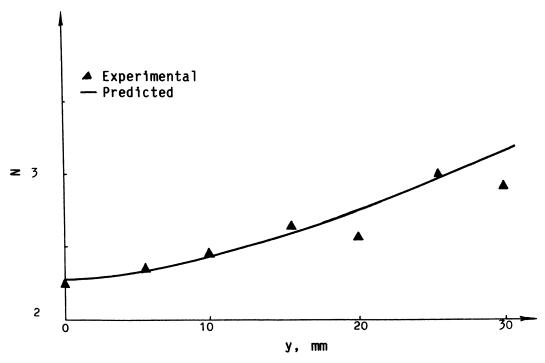
Figure 7. - Variation of drop-size distribution parameter (N) along radial distance (y) for x = 70 mm, V_a = 9 m/sec, and ΔP = 12 kg/cm^2.
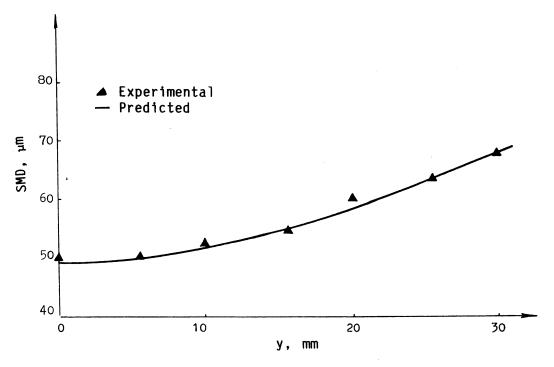
Figure 8. - Variation of Sauter mean diameter (SMD) along radial
distance (y) for x = 70 mm, V_a = 6 m/sec, and ΔP = 12 kg/cm^2.
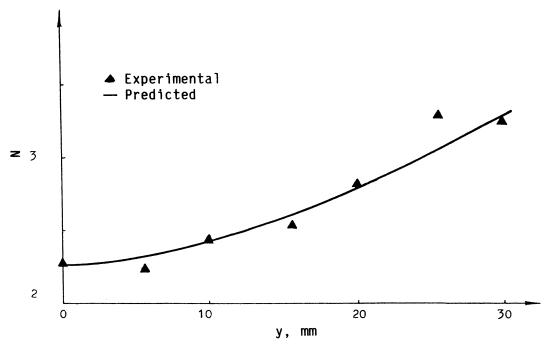
Figure 9. - Variation of drop-size distribution parameter (N) along
radial distance (y) for x = 70 mm, V_a = 6 m/sec, and
ΔP = 12 kg/cm^2.

60
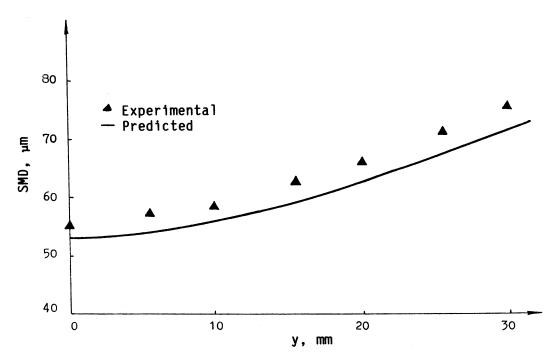
Figure 10. - Variation of Sauter mean diameter (SMD) along radial distance (y) for x = 70 mm, V_a = 6 m/sec, and ΔP = 8 kg/cm^2.
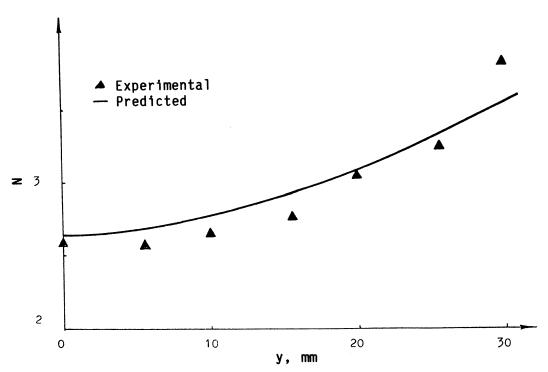
Figure 11. - Variation of drop-size distribution parameter (N) along radial distance (y) for x = 70 mm, V_a = 6 m/sec, and ΔP = 8 kg/cm^2.

61
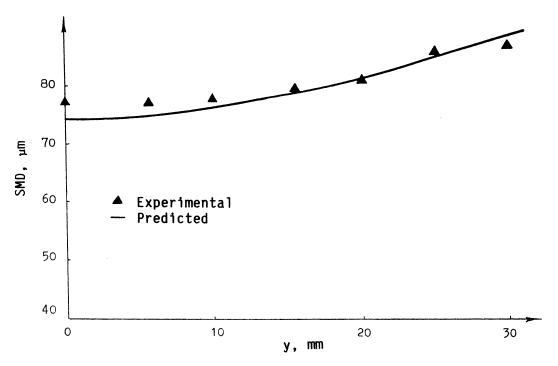
Figure 12. – Variation of Sauter mean diameter (SMD) along radial distance (y) for x = 70 mm, V_a = 6 m/sec, and ΔP = 4 kg/cm^2.
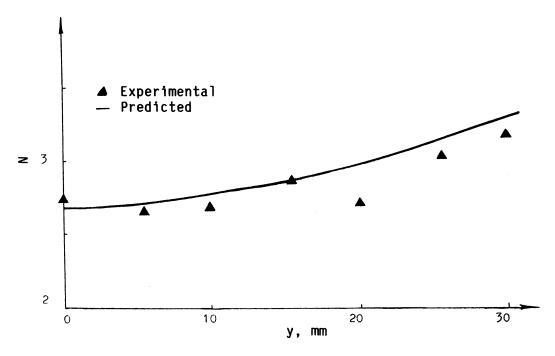
Figure 13. – Variation of drop-size distribution parameter (N) along radial distance (y) for x = 70 mm, V_a = 6 m/sec, and ΔP = 4 kg/cm^2.

TWO-PHASE FLOW

Robert R. Tacina
NASA Lewis Research Center
Cleveland, Ohio

An experimental program to characterize the spray from candidate nozzles for icing-cloud simulation is discussed. One candidate nozzle, which is currently used for icing research, has been characterized for flow and drop size. The median-volume diameter (MVD) from this air-assist nozzle is compared with correlations in the literature. The new experimental spray facility is discussed, and the drop-size instruments are discussed in detail. Since there is no absolute standard for drop-size measurements and there are other limitations, such as drop-size range and velocity range, several instruments are used and the results are compared. The drop-size instruments used are the Malvern 2600, the NASA Lewis Scanning Radiometer, the Phase/Doppler Spray Analyzer (P/DSA), a Forward-Scattering Spectrometer Probe (FSSP), an Optical Array Probe (OAP), and a limited amount of photography. The known capabilities and limitations of the drop-size instruments are compared.

A two-phase model was developed at Pennsylvania State University. The model uses the k-ε model of turbulence in the continous phase. Three methods for treating the discrete phase are used: (1) a locally homogenous flow (LHF) model, (2) a deterministic separated flow (DSF) model, and (3) a stochastic separated flow (SSF) model. In the LHF model both phases have the same velocity and temperature at each point. The DSF model provides interphase transport but ignores the effects of turbulent fluctuations. In the SSF model the drops interact with turbulent eddies whose properties are determined by the k-ε turbulence model. The two-phase flow model has been extended to include the effects of evaporation and combustion. Model development has been accompanied by an experimental program to provide data for verification. Presently, the model has been further extended at NASA Lewis to include the effects of swirling flow, and a particle-laden swirling flow experiment is currently being performed to provide verification data.

INTRODUCTION

Sprays and two-phase flow are of interest in many fields - for example, gas turbine combustion, agricultural crop spraying, paint spraying, fire protection, and drying. This paper describes the use of sprays to simulate icing clouds for the Altitude Wind Tunnel Icing Research Program. Icing-cloud simulation and gas turbine combustion research have common interests in the method of injection, the characterization of drop size and of droplet velocities, and the development of analytical models for droplet trajectories and droplet vaporization. This paper discusses injector or spray-nozzle drop-size characterization, an experimental test facility for injector characterization, drop-size measurement techniques, and analytical models for trajectory calculations.

INJECTOR CHARACTERIZATION

The injector, or spray nozzle, used currently for icing-cloud simulation at the NASA Lewis Research Center is an air-assist injector (fig. 1). It is

very similar to the injector used by Nukiyama and Tanasawa (ref. 1). The water flows through a center tube (0.635-mm diam) and has a concentric annular passage (9.35-mm diam) for air-assist flow. The water and the air exit through a 3.175-mm orifice. The advantage of an air-assist injector for icing research and other applications is that, within limits, there is nearly independent control of water flowrate and drop size. The water flow is controlled by the difference between the air pressure and water pressure, and the drop size is controlled by the air pressure only.

Drop-size measurements using this injector were made for us at Arnold Engineering Development Center by J.L. Hunt. The drop-size data shown in figure 2 are plotted as median-volume diameter in micrometers. The median-volume diameter MVD is defined as the drop size where 50 percent of the total droplet volume is contained in droplets less than that diameter, and 50 percent is contained in droplets greater than that diameter. The MVD is plotted as a function of the difference of water and air-assist pressure with the air-assist pressure as a parameter.

This method of correlating the data is very useful for setting the operating conditions in the wind tunnel. However, the drop-size data could be presented in a more fundamental manner as a function of the water to air mass ratio. Other factors that appear in correlations in the literature, such as viscosity, surface tension, and relative velocity between the air and water, are constant or nearly constant for these data. The relative velocity is nearly constant, even though the flowrates are changing. The reason for this is, first, that the air is being injected at high pressure into a low-pressure ambient environment and thus has sonic, or nearly sonic, velocity. Second, the water pressure is relatively low so that the water has a relatively small velocity compared to the sonic velocity of the air. Thus, the difference in the velocities or the relative velocity is constant.

These data were compared to values from various correlations. These comparisons are shown in figure 3 for one air-assist pressure. The injectors used in the references were similar to the NASA Lewis Research Center injector. However, the drop-size measurement techniques were different. The Nukiyama-Tanasawa (ref. 1) drop-size correlation was made from measurements of water droplets on photographs. The Lorenzetto-Lefebvre correlation (ref. 2) was made from light-scattering measurements of water droplets. Wigg (ref. 3) used measurements from molten wax sprays with swirl. As you can see in the figure, the results of the correlations have a wide range of values, some higher and some lower than the data taken at Arnold. Preliminary data taken at NASA Lewis seem to be closest to the data of Nukiyama-Tanasawa. Preliminary data taken with the NASA Lewis injector at Carnegie-Mellon University are lower than the Arnold data. There needs to be much more work on drop-size measurements and correlations before drop sizes can be accurately predicted.

TEST FACILITY

The objectives of our experimental program are to characterize a variety of candidate injectors for drop size and dispersion, to compare different drop-size measurement techniques, and to take data that can be used for trajectory models. Trajectory model data consist of initial condition data taken upstream close to the injector and verification data taken far downstream.

The test stand is shown in figure 4. Duct air enters through a 40-cm-diameter pipe. The maximum air velocity through the pipe is 88 m/sec. We will be able to control the relative humidity from 0 to 100 percent by adding steam far upstream. Controlling the relative humidity could be necessary if evaporation is important.

The duct air temperature will be controlled by injecting liquid nitrogen upstream. The primary use of the temperature control will be to provide a constant inlet temperature of 292 K. For some icing tests the inlet temperature is held at 273 K and even lower temperatures for shorter times.

The injector is inserted in a section with a window so that the nozzle operation can be monitored with a television camera. Water is the only liquid capable of being tested in this facility. The water is demineralized and heated to 380 K. For icing applications, the water and the air-assist injector are heated so that ice crystals do not form during the expansion process. The water and air-assist flow temperature can be controlled between the ambient temperature and 373 K.

The injector is shown in a section 2.5 m upstream of the instrument section. The injection section can be moved to any location closer to the instrument section. Upstream of the injector there is a traversing pitot tube to measure the inlet velocity.

Downstream, at the instrument section, drop-size measurements can be made. The instrument section has a square cross section with windows in the sides that are at 7° angles to each other to prevent reflections. Other drop-size instruments that are used are described in the next section. The instruments sit on a three-axis traversing table so that radial and spatial variations can be measured. A liquid-water measurement probe traverses vertically to measure the variation in liquid-water concentration.

Another set of droplet-sizing instruments is mounted in the duct downstream of the instrument section. The principle of operation of these instruments is discussed in the next section. These instruments are intrusive and mounted in a fixed position. They are the same instruments that are mounted on airplanes to measure drop sizes in clouds. Tests with these instruments will provide a good comparison of the data from the nozzles with that in the clouds. This is an atmospheric pressure rig, so the air and water are vented to the atmosphere.

DROP-SIZE INSTRUMENTS

The most important factor in making drop-size measurements is the drop-size measuring instrument. As you have seen from the figure comparing the drop-size data correlations, there must be large differences in the data on which they are based. One of the major problems is that there is no standard to which to compare the drop-size measurements, especially in a spray. Since there are other limitations beside the lack of a standard such as drop-size range and velocity range, in our program we use five different drop-size instruments and compare the results. The instruments are a Malvern 2600, a NASA Lewis Scattered-Light Scanner, a Phase/Doppler Spray Analyzer, a Forward-Scattering Spectrometer Probe, and an Optical Array Probe. And a limited

amount of photography is used for qualitative analysis. A qualitative analysis and a discussion of each of these instruments follows.

The Malvern 2600 is a commonly used drop-size instrument (fig. 5). Lewis' HSD version of this instrument, which provides a faster snapshot of the data, is described in reference 4. (The inserts in figure 5 describe the principle of operation.) This instrument measures the angle that the light is diffracted by the drops. The bigger drops diffract the light at a small angle and the smaller drops diffract the light at a larger angle. The detector is a series of concentric rings that determine the angle of the scattered light. The drop size is calculated from the scattered light angle. The insert also shows that, no matter where the droplet is in the line of sight, the light that is scattered at the same angle always falls on the same detector ring.

Although there is no standard for determining drop sizes, we use a Hirleman reticle for calibration purposes. The Hirleman reticle (fig. 6) consists of a glass substrate on which chrome disks are photographically deposited. The chrome disks are sized to represent a Rosin-Rammler distribution with an x-bar of 50 and an n value of 3. One problem we have found using the reticle with the Malvern 2600 is that there is a correction for anomalous diffraction. The Malvern calculations are based primarily on Fraunfaufer diffraction theory. However, for small drop sizes (below a diameter of 5 μm) three-dimensional effects are considered; these effects are lumped under the term anomalous diffraction. Thus, the problem is that the reticle has two-dimensional disks and not three-dimensional spheres. We are currently studying the feasibility of modifying the Malvern software to ignore the anomalous diffraction calculation when using the reticle. If this does not prove to be practical, we will still use the reticle for relative comparisons.

We also plan to add an additional lens system to the Malvern to be able to measure an MVD of 5 μm across the 30-cm instrument section. Verification of the correctness of the additional lens system will be done by taking measurements of the reticle with and without the additional lens system.

The second instrument, the Scattered-Light Scanner, is also based on the diffraction principle. This is a revised version of the NASA Lewis Scanning Radiometer (described in ref. 5), which was developed by Don Buchele and used in many research projects by Robert Ingebo. Figures 7 to 9 explain the operation of the instrument.

Figure 7 shows the reflection, refraction, and diffraction of a laser light beam passing through a drop. Since calculations are based on the diffraction of light through the drop, the wide-angle diffraction is ignored. There is narrow-angle diffracted light from the envelope (or aperture) of the laser beam that must also be ignored.

Figure 8(a) is a plot of light intensity as a function of the light-scatter angle. Figure 8(b) shows the product of the light intensity and the light-scatter angle as a function of the light-scatter angle. It shows that the measurement interval extends from where the intensity of the near envelope diffraction is negligible to a value of the light intensity which is still high enough to be meaningful. A scanner is used to measure the intensity of the scattered light as a function of the light scatter angle. The scanner is a

disk with a radial slot that is rotated with its centerline eccentric to the laser beam centerline.

To calculate the mean drop size, Don Buchele has calculated the light intensity as a function of a beam spread parameter (fig. 9). From the previous figure we can find the maximum light intensity and the light intensity at a specified angle. Using these values and the beam spread parameter and knowing the wave length and the specified angle, we can determine the mean drop size. Calculations were made with five different distribution correlations, and they are shown plotted for three dispersion levels. The distribution correlations used were the Nukiyama-Tanasawa, the upper-limit distribution functions, the Rosin-Rammler, the Weibel, and the Rinks distribution function. The beam-spread parameter is nearly the same for all the distributions and dispersions at a relative intensity of 0.75. If this relative intensity is used, then the mean drop-size calculation is independent of distribution and dispersion. The dispersion can be calculated from the slope of the curve.

A schematic of the Scattered Light Scanner (fig. 10) shows the various parts and dimensions of the instrument. The primary feature is the eccentric light scanner.

The third drop-size instrument to be discussed was developed under a NASA combustion fundamentals contract to William Bachello at Aerometrics Corporation. The method is the phase/Doppler detection technique and the instrument is called the Phase/Doppler Spray Analyzer (ref. 6). This is a scheme where a set of laser beams is crossed to form a fringe pattern (fig. 11). As a droplet passes through the fringes the light is scattered and measured 30° off axis with a photodetector. From this measurement, simultaneous values of drop diameter and velocity can be calculated. The measurement and calculations are for single droplets; averages and medians are calculated from the single droplet data.

Figure 12 shows in more detail the principle of the phase/Doppler system. The scattered light is collected by three detectors with slightly different spatial locations. Because of the spatial difference, the light path to the three detectors is different, and thus there is a phase difference in the signals. From this phase difference the drop size can be calculated. Again, the phase difference occurs because of the path difference inside the drop, so that the phase angle is a function of the diameter.

Figure 12(b) is a plot of phase difference as a function of diameter. From the phase difference between detectors 1 and 2, an approximate drop-size estimate can be made. From this approximate drop size and the phase difference between detectors 1 and 3, a more accurate determination of diameter can be made.

The calculations are based on reflection and refraction theory. Diffraction can be ignored because the measurements are taken 30° off axis, where diffraction is negligible.

The Forward-Scattering Spectrometer Probe (FSSP) is one of the two intrusive instruments that we use that is located downstream of the instrument section. This instrument is the same type that is mounted on airplanes to measure raindrop diameters (see ref. 7). It provides a comparison of the other drop-size instrument measurements with the measurements made in clouds.

The FSSP is a single particle counter. A schematic of its operation is shown in figure 13. A laser beam is optically directed across two arms of the probe, in a direction perpendicular to that of the particle-laden flow. Scattered light from a particle is optically directed and focused onto a photodiode to measure the intensity of the scattered light. Any unscattered light is removed by the dump spot. The scattered light is also directed onto a second photodetector that is used to determine whether the droplet is in focus (in focus along the axial length of the laser beam). This second photodetector also has a dump spot. The light from a droplet that is in focus is removed by the dump spot. A droplet that is not in focus has a broader signal that is not removed by the dump spot, and the droplet measurement is rejected.

Drop size as a function of the measured intensity is shown in figure 14. In the figure the light intensity is shown in the near forward-scattering angles of 4° to 14°. The curve is shown for a Gaussian T-type (transverse electric) beam. This is a multivalued function; thus, for a given intensity, the drop size may not be uniquely determined. The actual instrument uses a high-mode laser beam which has a smooth curve and is single valued.

The last drop-size instrument to be discussed is the Optical Array Probe (OAP), which can also be flown on an airplane to measure raindrop sizes. This instrument is made by the same company as the FSSP, but it is made to cover a larger drop-size range. The operating principle is shown in figure 15. It is a single-particle imaging system. The drops pass through a laser beam, and then the light is transmitted through the instrument optics to an array of photodetectors. The drop size is determined by counting the detectors in the shadow of the drop. The last detector at each end is kept open as a check to determine if the whole drop is seen. To determine if the drop is in focus, we use an intensity gradient criteria. An infocus drop has a sharp gradient from lit to unlit photodetectors, while an out-of-focus drop has a gradual gradient from lit to unlit. Figure 16 is a simple schematic of the OAP.

Table I compares the FSSP, OAP, Malvern 2600, Scattered-Light Scanner, and Phase/Doppler Particle Analyzer (P/DSA) drop-size instruments. The size range refers to the droplet diameters that can be measured with any particular setup. The number of bins refers to the number of increments into which the size range is divided. The overall size range then refers to the smallest to the largest diameter that can be measured, but it may require a change in setup and multiple measurements to cover the range. The numbers in the ranges refer to individual droplets for all the instruments except for the Scattered Light Scanner, whose range is given in MVD.

The velocity limits are all acceptable for our work except for those of the P/DSA, which has a slight limitation for our purposes. Currently manufactured P/DSA instruments have a upper limit of 75 m/sec. The comments section lists features that we consider particularly beneficial. With the FSSP and OAP, we consider the ability to use the same instrument to obtain data from clouds and the test facility to be important. The Malvern and the Scattered-Light Scanner have the ability to measure MVD directly and thus are good for screening a number of injectors quickly. The P/DSA has the capability of making point measurements of size and velocity which makes the data particularly useful for modeling work.

ANALYTICAL TRAJECTORY MODELS

The second part of this report describes spray model development. The model work to be presented was done at Pennsylvania State University by Professor Faeth and his graduate students and associates (refs. 8 to 10). Figure 17 shows the important interactions of the drop with its environment. These interactions are: the droplet drag that results in a source term in the continuous flow equation, random deflections of the drops by turbulent eddies, and turbulence modulation of the continuous phase by the extraction of turbulent energy by the droplet drag. Actually, three models of increasing complexity were developed. They are a locally homogenous flow model, a deterministic separated-flow model, and a stochastic separated-flow model.

The locally homogenous flow model is the simplest model (fig. 18). It uses the k-ε model to calculate the continuous-phase flow characteristics. It then assumes that the particles have the same velocity as the continuous phase and treats the k-ε equations as a varying-density flow. This model is correct for small drops that follow the continuous phase flow. An advantage of the model is that the calculation is no more complex for a two-phase flow than for a single-phase flow. It is also useful when the initial conditions of the spray, such as drop size or spray angle, are not available since they are not needed in the calculation.

The second model is the deterministic separated flow (DSF) model (fig. 19). It also uses the k-ε model to calculate the gas or continuous-phase flowfield. The particle or droplet distribution is divided into a number of classes with a representative number of droplets in each class. Then, for each drop, the trajectory is calculated. The trajectory calculation is based on the mean continuous-phase flow properties. Dispersion due to turbulence is ignored. This is the most widely used approximation in current models of combusting sprays. Other assumptions are that the drops are spherical and that the spray is dilute with no collisions.

One feature of this model is the particle-in-cell approach. As a particle goes through a cell, the drag momentum is coupled with the continuous-phase momentum. The net change in momentum is calculated for each drop class as it passes through a computational cell as shown in figure 20. Then the gas or continuous-phase flow equation is calculated with the change in momentum as a source term.

The last, and most complex, model is the stochastic separated flow (SSF) model (fig. 21). In this model, the continuous-phase turbulence does interact with the drop or particle. Again the gas-phase calculation is made using the k-ε model. To make the Lagragian drop-trajectory calculation we assume the drop interacts with an eddy. The properties of the eddy have a distribution based on a probability density function with a standard deviation dependence on k. From the distribution, the properties of the eddy are found by using a Monte Carlo technique. The interaction is shown in figure 22. The drop interacts with the eddy either for the lifetime of the eddy or the time it takes the particle to traverse the eddy. The size of the eddy is based on the dissipation length. The number of calculations are much greater for this

method than for the deterministic separated flow (DSF) model. While for the DSF model approximately 600 drops are sufficient for an accurate calculation, for the stochastic separated flow model about 6000 drops are needed for an accurate calculation.

An experimental study was also done to complement the analytical modeling effort. From a large amount of data, four plots were chosen as representive. Figure 23 is a plot of the mean axial velocities of the drops as a function of the drop diameter at different axial locations. An air-assist injector with an exit-orifice diameter of 1.194 mm was used. The initial conditions were taken at an x/d of 50, where x is the axial distance and d is the injector-orifice diameter. This is a distance of about 55 mm. This was sufficient distance for the spray to be well formed for most conditions. However, there were some conditions where ligaments were observed.

The drop-size and velocity measurements were made using double-flash photography. Two other methods were used to measure drop size. One was slide impaction in which a slide coated with magnesium oxide was used. The second alternate method was to measure drop size with a Malvern. The Malvern measurement was used mainly to monitor the spray to determine whether the spray varied from day to day.

The data were compared with the calculations from the stochastic separated flow model and the deterministic separated flow model. The calculations agree well, with the data from the stochastic separated flow model agreeing the best. For all the data plots, the stochastic separated flow model agreed well with the data, while the deterministic separated flow model and the locally homogenous model agreed well for some conditions and not so well for other conditions.

Figure 24 shows the radial variation of mean liquid flux G. For this case, the SMD at an x/d of 50 was 30. Again the calculations with the stochastic separated flow model agree well with the data for all conditions, while the other two models do not agree well for all conditions. It is interesting to note that the locally homogenous model underpredicts the data. For all the previous work in which the locally homogenous model was calibrated with solid-particle-laden flow, the model overpredicted the development of the spray.

Figure 25 shows the variation of the Sauter mean diameter with the distance along the axis. Figure 25(a) is for a nonevaporating oil spray and figure 25(b) is for an evaporating Freon 11 spray. Case 1 had an initial SMD of 30 at an x/d of 50 and case 2 had an initial SMD of 87. For the nonevaporating case, the mean diameter increases after an x/d of 100 because of the greater dispersion of the small drops. The stochastic separated flow model does better at predicting the data because it considers the dispersion due to turbulence.

The variation of SMD along the axis for an evaporating spray is shown in figure 25(b). For an evaporating spray, there are competing effects: evaporation reduces the mean diameter, and greater dispersion of the small drops increases the mean diameter along the axis. The stochastic separated flow model and deterministic separated flow model do a good job of predicting the trends even if they do not exactly duplicate the data.

The model development is continuing at the NASA Lewis Research Center as part of a Ph.D. thesis (by Daniel Bulzan). The ability to calculate flow fields with swirl has been added to the model, and an experimental calibration and verification is underway. The experiment will have a weakly swirling flow field with a swirl number of less than 0.4. Glass beads with known sizes will be used to simplify the analysis. Particle number flux will be measured by a 30° off-axis Mie-scattering technique. Laser Doppler velocimetry (LDV) will be used to measure the particle and gas-phase velocities. The parameters to be studied are swirl number, particle loading ratio, and particle size. The initial conditions will be well characterized to provide input conditions to the computer model.

Figure 26 is a drawing of the experimental configuration. It has a two-component laser velocimeter system that will be used to measure the particle and the gas-phase velocities. Small aluminum oxide particles, approximately 0.5 μm diameter, will be added to make the gas-phase velocity measurement. The laser system will remain fixed and the injection system will be traversed to determine spatial variations. The injector has four tangential slots to create swirl.

CONCLUDING REMARKS

There has been much work in this field of two-phase flow in the past, and, with the new instruments that are more accurate, faster, and easier to use, there promises to be great advances in the experimental data base. Analytical models will complement the experimental work; there promises to be more accurate and faster analytical models to calculate the two-phase flow fields that exist in icing clouds, gas turbine combustors, and other applications.

REFERENCES

1. Nukiyama, Shiro; and Tanasawa, Yasushi (E. Hope, trans.): Experiments on the Atomization of Liquids in an Air Stream. Rept. No. 4, The Influences of the Characteristics of the Liquid on the Atomized Droplets. Defense Res. Board, Dept. Nat. Defense, Ottawa (Canada), Mar. 18, 1950. (Trans. from Trans. Soc. Mech. Eng. (Japan), vol. 5, no. 18, Feb. 1939, pp. 68-75.)

2. Lorenzetto, G.E.; and Lefebvre, A.H.: Measurements of Drop Size on a Plain-Jet Airblast Atomizer. AIAA Paper 76-679, July 1976.

3. Wigg, L.D.: Drop-size Prediction for Twin-fluid Atomizers. J. Inst. Fuel, vol. 37, no. 286, Nov. 1964, pp. 500-505.

4. Watson, D.J.: Laser Diffraction Measurements in Transient Spray Conditions. ICLASS-85, 3rd International Conference on Liquid Atomization and Spray Systems, Vol. 1, P. Eisenklam and A. Yule, eds., Institute of Energy, London, 1985, pp. VC/4/1 - VC/4/15.

5. Buchele, D.R.: Particle Sizing by Measurement of Forward-Scattered Light at Two Angles. NASA TP-2156, 1983.

6. Bachalo, W.D.; and Houser, M.J.: Phase/Doppler Spray Analyzer for Simultaneous Measurements of Drop Size and Velocity Distributions. Opt. Eng., vol. 23, no. 5, Sept.-Oct. 1984, pp. 583-590.

7. Knollenberg, R.G.: The Use of Low Power Lasers in Particle Size Spectrometry. Practical Applications of Low Power Lasers, SPIE vol. 92, D.D. Eden and J.S. Chivian, eds., SPIE, 1976, pp. 137-152.

8. Shuen, J-S., et al.: Structure of Particle-Laden Jets: Measurements and Predictions. AIAA J., vol. 23, no. 3, Mar. 1985, pp. 396-404.

9. Solomon, A.S.P., et al.: Measurements and Predictions of the Structure of Evaporating Sprays. J. Heat Trans., vol. 107, no. 3, Aug. 1985, pp. 679-686.

10. Shuen, J-S.; Solomon, A.S.P.; and Faeth, G.M.: Drop-Turbulence Interactions in a Diffusion Flame. AIAA J., vol. 24, no. 1, Jan. 1986, pp. 101-108.

TABLE I. - DROPLET-SIZE INSTRUMENT COMPARISON

	Forward-Scattering Spectrometer Probe, FSSP	Optical Array Probe, OAP	Malvern 2600	Scattered-Light Scanner	Phase/Doppler Particle Analyzer, P/DPA
Size range	1 to 16 2 to 32 2 to 47 5 to 95	20 to 300	1.3 to 128 1.9 to 188 5.7 to 564	6 to 120 MVD	$D_{max}/D_{min} = 35$
Number of bins	15	15	15	NA	68
Overall size range	1 to 95	20 to 300	1.3 to 564	6 to 250 MVD	1 to 1000
Velocity limits	5 to 100 m/sec	5 to 100 m/sec	None	None	3.2 x fringe spacing 41 m/sec
Measurement theory	Scattering amplitude	Particle shadow size	Fraunhofer diffraction	Fraunhofer diffraction	Geometric optics
Type of measurement	Single-particle counter	Single-particle counter	Ensemble average	Ensemble average	Single-particle counter
Probe volume	0.218-mm (diam) x 2.61 mm	4.8 mm (diam) x 6 cm	Line of sight x 9 mm diam	Line of sight x 50 mm or 18 mm	0.160 mm (diam) x 0.050 mm
Comments	Flight-instrument icing research		Measures volume distribution (best for MVD)		Size-velocity correlation

AIR-ASSIST FLOW

WATER
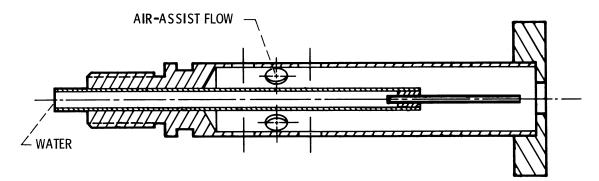
Figure 1. - IRT nozzle.

AIR-ASSIST
PRESSURE,
MPa

○ .17
□ .31
◇ .44
△ .58
▽ .78
◊ 1.05

MEDIAN-VOLUME DROP SIZE, μm

WATER PRESSURE-AIR-ASSIST PRESSURE, MPa
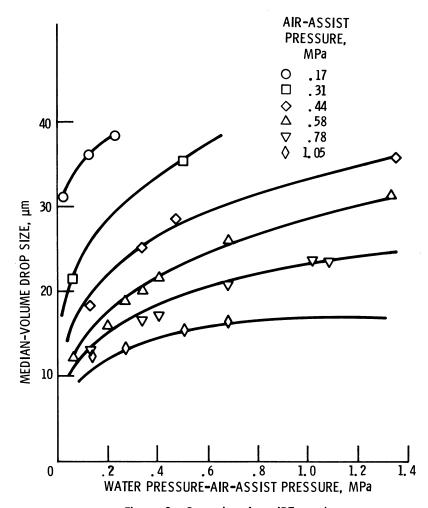
Figure 2. - Drop sizes from IRT nozzle.
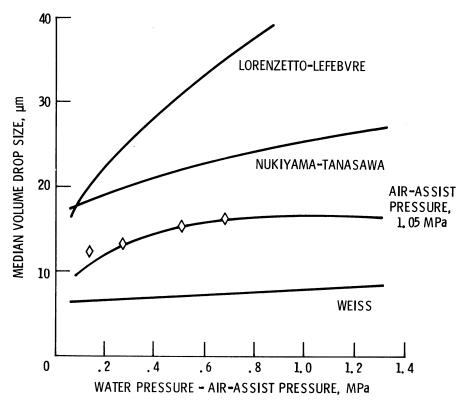
Figure 3. - Comparison of IRT nozzle drop-size data with correlations.

CD-85-17628
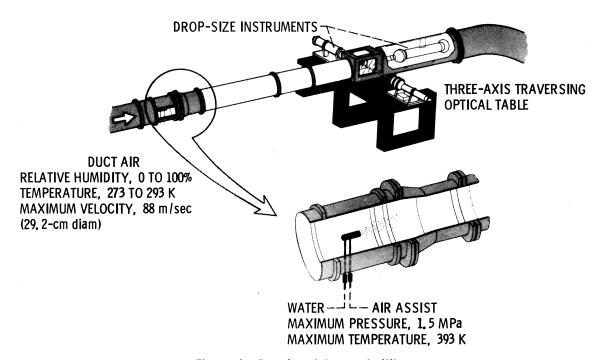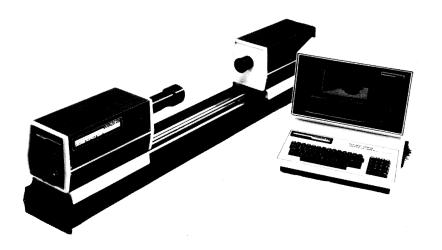
Figure 4. - Experimental spray facility.

74
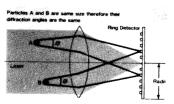
PRINCIPLE OF DIFFRACTION SIZING

MEASURING MOVING PARTICLES

SMALL PARTICLES DIFFRACT LIGHT
THROUGH LARGE ANGLES AND
LARGE PARTICLES THROUGH SMALL
ANGLES

WHEN A FOURIER TRANSFORM
LENS IS USED, THE LIGHT DIF-
FRACTED BY PARTICLES OF A
GIVEN SIZE AT ANY POSITION
IN SPACE ALWAYS FALLS ON
THE SAME PART OF THE DE-
TECTOR

Figure 5. - Malvern spray analyzer.

SIZING
ARRAY
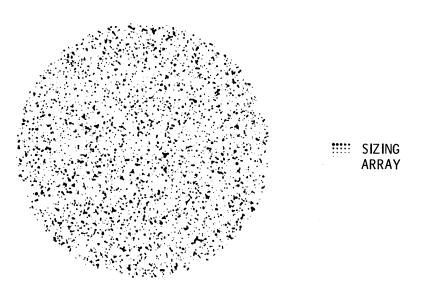
Figure 6. - Photograph of sample area and quality control array of Hirleman
calibration reticle (RR-50-3.0-0.08-102-CF-#115). Magnification 10x.

CD-85-17399

75

WIDE-ANGLE REFRACTION THROUGH DROP, CAN BE NEGLECTED

MEDIUM-ANGLE DIFFRACTION AROUND DROP, $\theta = \lambda/\pi D$, MEASURED

SMALL-ANGLE DIFFRACTION NEAR ENVELOPE OF LASER BEAM, PREVENTS MEASUREMENT AT SMALL ANGLES
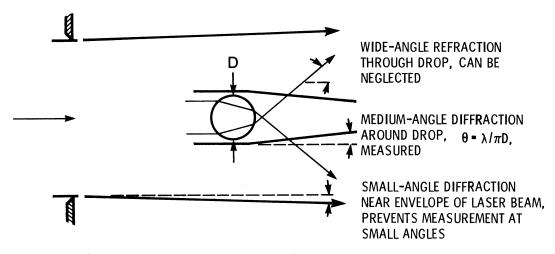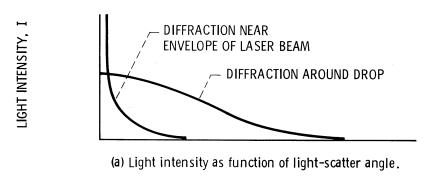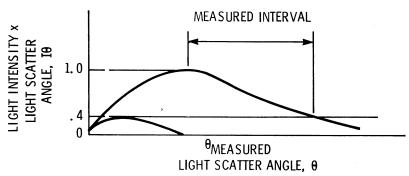
Figure 7. - Three principal components of scattered light at test section.

CD-85-17397

DIFFRACTION NEAR ENVELOPE OF LASER BEAM

DIFFRACTION AROUND DROP

(a) Light intensity as function of light-scatter angle.

MEASURED INTERVAL

θMEASURED

LIGHT SCATTER ANGLE, θ

CD-85-17413

(b) Product of light intensity and light-scatter angle as function of light-scatter angle.

Figure 8. - Intensity of forward-scattered light.

76

$$\text{DISPERSION} = 2(D_{.9} - D_{.1})/(D_{.9} + D_{.1})$$
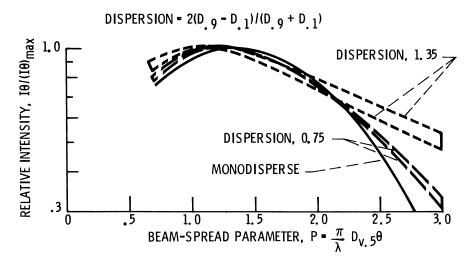
Figure 9. – Envelope of scattered light for five volume–distribution functions and three dispersions.

CD-85-17629
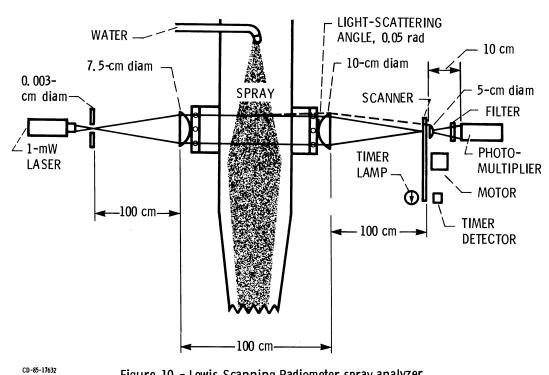
Figure 10. – Lewis Scanning Radiometer spray analyzer.

CD-85-17632

77
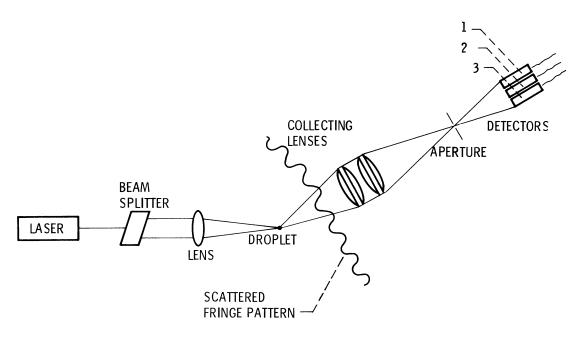
Figure 11. - Phase/Doppler detection technique.

CD-85-17395

(a) Optical system.

(b) Instrument response curves.

(c) Scattered-light interference pattern.

CD-85-17631

(d) Filtered Doppler burst signals.
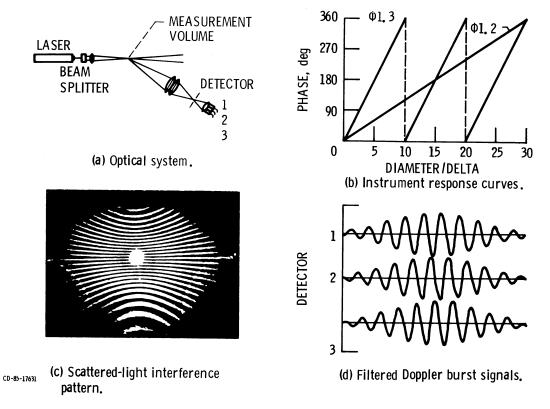
Figure 12. - Schematic of Phase/Doppler Spray Analyzer technique.
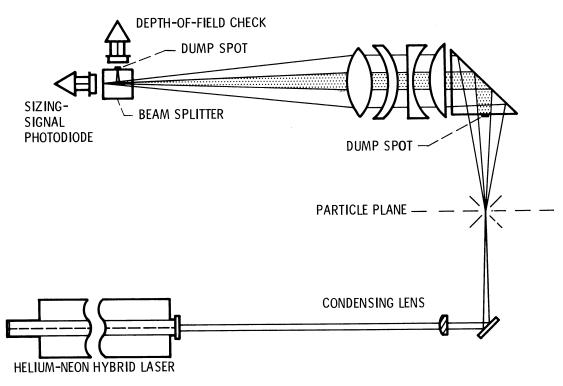
Figure 13. - FSSP optical path.

CD-85-17405
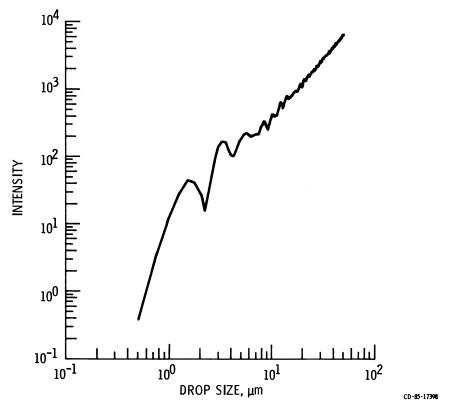
Figure 14. - Forward- Scattering Spectrometer Probe (FSSP) light scattering as function of drop size. Light intensity measured at scattering angles of 4° to 14°.

CD-85-17398

79
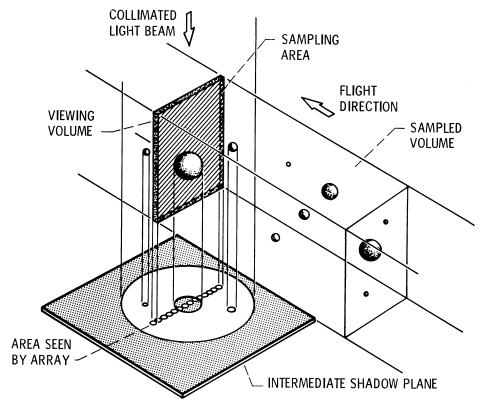
Figure 15. – Optical Array Probe (OAP) operating principle.
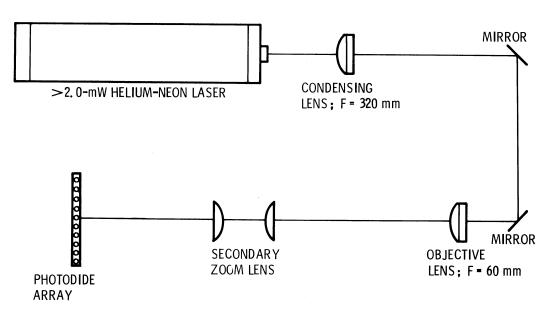
Figure 16. – Optical Array Probe (OAP) optical path.

80
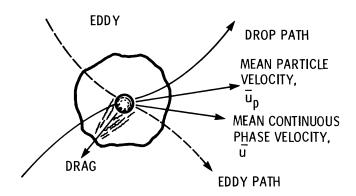
Figure 17. - Phase interactions for particle-laden flow.

$(\bar{u} + u')_i = (\bar{u}_p + u'_p)_i$
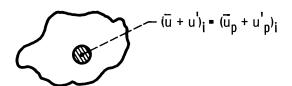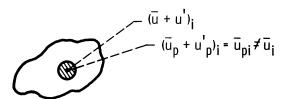
Figure 18. - Locally homogeneous flow (LHF) model.

ASSUMPTION: FINITE INTERPHASE TRANSPORT
RATES BUT PARTICLES ONLY
RESPOND TO MEAN MOTION

$$(\bar{u} + u')_i$$

$$(\bar{u}_p + u'_p)_i = \bar{u}_{pi} \neq \bar{u}_i$$

NOTES: I - PARTICLE DISPERSION IGNORED - ONLY
VALID FOR "LARGE" PARTICLES

II - MOST WIDELY USED APPROXIMATION
IN CURRENT MODELS OF COMBUSTING
SPRAYS AND PULVERIZED COAL

III - FLOW FIELD FOUND FROM EULERIAN
CALCULATION WITH DISTRIBUTED SOURCE
TERMS DUE TO PARTICLES. LAGRANGIAN
CALCULATION DETERMINES PARTICLE
TRAJECTORIES

Figure 19. - Deterministic separated flow (DSF) model.

CD-85-17406
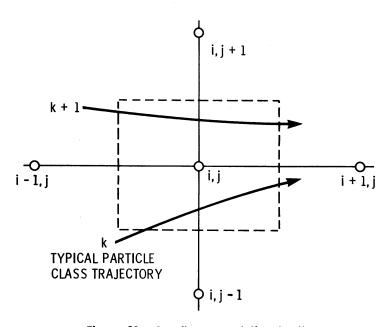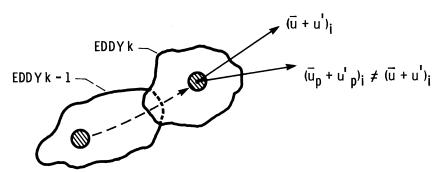
Figure 20. - Gas-flow computational cell.

CD-85 17408

ASSUMPTION: FINITE, INTERPHASE TRANSPORT RATES WITH PARTICLES
INTERACTING WITH INDIVIDUAL EDDIES WHOSE PROPERTIES
ARE FOUND BY RANDOM SAMPLING OF LOCAL TURBULENCE
PROPERTIES

$$(\bar{u} + u')_i$$

EDDY k

EDDY k - 1

$$(\bar{u}_p + u'_p)_i \neq (\bar{u} + u')_i$$

NOTES: I - INVOLVES ADDITIONAL ASSUMPTIONS CONCERNING THE
PROPERTIES, SIZE, AND LIFETIME OF EDDIES

II - COMPUTATIONS SIMILAR TO DSF MODELS, BUT MONTE CARLO
TECHNIQUES USED TO FIND STATISTICALLY SIGNIFICANT
NUMBER OF PARTICLE TRAJECTORIES - CAUSING ADDED
COMPUTATIONS

Figure 21. - Stochastic separated flow (SSF) model.

CD-85-17411

EDDY

PARTICLE TRAJECTORY

y

z

x
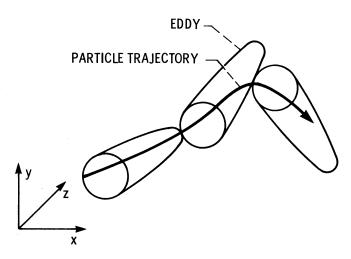
Figure 22. - Particle-eddy interaction.

CD-85-17407

83
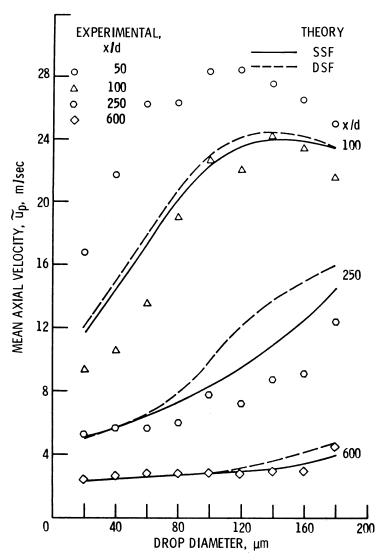
Figure 23. - Mean axial-drop velocities along axis. Non-evaporating spray; case 2.

THEORY

—————— SSF
— — — DSF
- - - - - LHF
○ EXPERIMENTAL

FLUX RATIO, $\widetilde{G}/\widetilde{G}_c$

(a) x/d = 50.

(b) x/d = 100.

(c) x/d = 250.

(d) x/d = 600.

RATIO OF RADIAL TO AXIAL DISTANCE, r/x
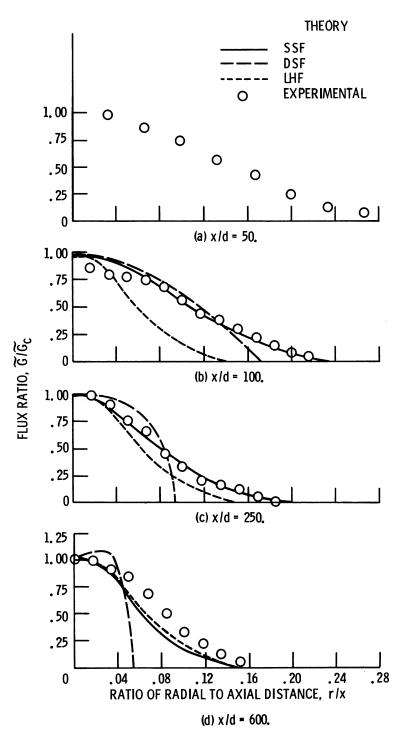
Figure 24. - Radial variation of mean liquid flux. Non-evaporating spray; case 1.

THEORY   EXPERIMENTAL
———— SSF   □ CASE 1
– – – DSF   ○ CASE 2

(a) Nonevaporating sprays.

(b) Evaporating sprays.
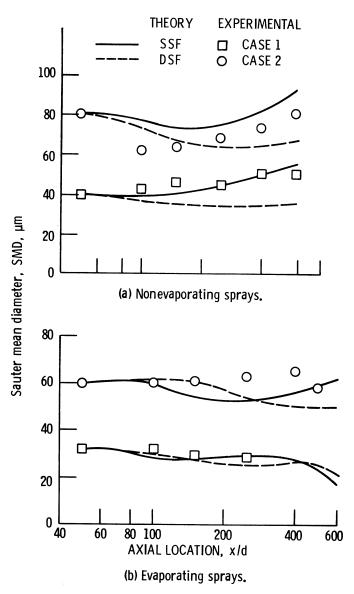
Figure 25. - Sauter mean diameter (SMD) along axis.

Sauter mean diameter, SMD, μm

AXIAL LOCATION, x/d

MOVABLE SCREENED ENCLOSURE

LDA RECEIVING OPTICS

MINICOMPUTER

TERMINAL

INJECTION TUBE WITH
AXIAL TRAVERSE

LDA SENDING OPTICS

COUNTER

2-W ARGON-ION LASER

EXHAUST

rms
VOLTMETER

ENCLOSURE TRACK
(X-Y TRAVERSE)

PARTICLE-
LADEN JET

OSCILLOSCOPE

INTEGRATING DIGITAL
VOLTMETER
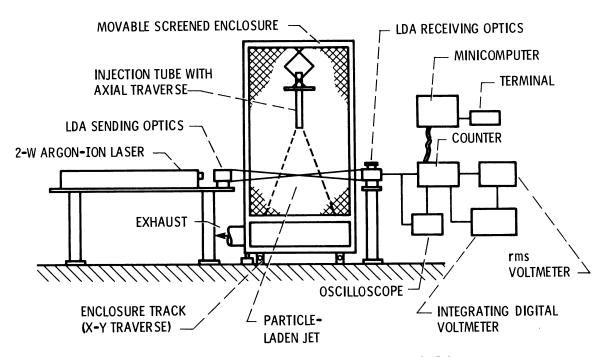
Figure 26. - Particle-laden swirling-flow experiment.

COMBUSTION RESEARCH ACTIVITIES AT THE GAS TURBINE RESEARCH INSTITUTE

Shao Zhongpu
Gas Turbine Research Institute
Jiangyou County of Sichuan, People's Republic of China

The Gas Turbine Research Institute (GTRI) is responsible mainly for basic research in aeronautical propulsion. The combustion research activities primarily cover the following areas: annular diffuser for the turbofan augmentor, combustor ignition performance, combustor airflow distribution, fuel injectors, vaporizer fuel injector, and airblast atomizer.

RESEARCH ON THE ANNULAR DIFFUSER FOR THE TURBOFAN AUGMENTOR

It is well known that the inlet velocity profile has a very strong influence on diffuser performance. The inlet velocity and temperature profiles are not uniform: both change with flight condition. The diffuser enlarges the inlet velocity distortion; that is, the nonuniformity of the velocity increases with the diffusion process occurring in the diffuser. The nonuniform inlet velocity profile encourages the airstream to separate from the diffuser wall or inner cone, induces flame stabilization in the separated flow region, and causes augmentor components to burn or to induce combustion instability. To obtain a desirable fuel-air distribution, it is necessary to understand the velocity and temperature profiles in the augmentor. In other words, since the velocity and temperature profiles at the exit of the diffuser must be known some experimental research was carried out on the annular diffuser of the turbofan augmentor.

The test model and the instrumentation locations are shown in figure 1. The test was run at the following conditions:

(1) Inlet Mach number, 0.08 to 0.60
(2) Inlet temperature, 300 to 600 K
(3) Inlet Reynolds number, $>5 \times 10^4$
(4) Diffuser outlet to inlet area ratio, 1.54
(5) Inner to outer annular area ratio, ≈ 1.0
(6) Inner cone, three configurations
(7) Cone angles, 20°, 30°, and 40°

The static-pressure recovery coefficients, velocity profiles, and temperature profiles along the axial distance were measured. The flow separation in the diffuser was studied by tuft observation method for low-temperature airflow under different inlet outer-inner velocity ratios and different inner-cone configurations. Typical inlet velocity and temperature profiles of the diffuser are shown in figures 2 and 3.

We found the following results:

(1) Within the range of the test Mach number (M_i or $M_e < 0.6$), the static-pressure recovery coefficients at different axial stations were independent of Mach number. As shown in figure 4, the inlet Mach number had little influence on the diffuser internal flow. Thus, the effect of inlet Mach number

can be neglected when testing or analyzing the performance of an annular diffuser for a turbofan augmentor.

(2) We also obtained an important nondimensional flow parameter,

$$S_D = \left(\bar{\rho}_e \bar{v}_e^2\right)\left(\bar{\rho}_i \bar{v}_i^2\right) = \left(\bar{v}_e \bar{T}_e^{-0.5}\right)\left(\bar{v}_i \bar{T}_i^{-0.5}\right)$$

If we use a diffuser with the same geometry and a similar inner velocity profile and maintain S_D = constant, then the change of static-pressure recovery coefficients and nondimensional, combined velocity-temperature combination distributions along the diffuser axial distance is the same, regardless of whether the test is done with low- or high-temperature air, as shown in figures 5 and 6. It is possible to use the low-temperature test to simulate real turbofan augmentor diffuser flow; low-temperature airflow separation can also be used to understand high-temperature airflow separation.

RESEARCH ON COMBUSTOR IGNITION PERFORMANCE

Under the high-altitude relight condition, the combustion chamber inlet pressure can be as low as 0.2 kg/cm^2, and the inlet temperature can be as low as -50 °C. Because it is important for combustion engineers to understand the relation between ignition performance and combustor inlet parameters, we studied the effect of inlet parameters on the ignition performance of combustors with different fuel-injection systems.

This test was performed on the high-altitude ignition test rig shown in figure 7. Three combustor configurations were used. The first configuration was a gas turbine combustor with a pressure swirl atomizer. (This combustor is similar to a JT-3D engine combustor with one flame tube.) The second configuration was a one-quarter sector of a full annular combustor with three T-shaped vaporizers, as shown in figure 8. The third configuration was similar to the second one - the only difference being that the three vaporizers had been replaced by three airblast atomizers.

A high-energy ignition plug was used for every configuration. The stored energy of the ignition system was 20 J, 12 J, and 8 J, respectively. The ignition procedures were repeated three times under every test condition. If all three ignitions were successful, then each was judged a successful ignition at its specific condition.

We drew the following conclusions from this experiment:

(1) The inlet pressure has a significant effect on the ignition performance of the combustors. Figure 9 shows the optimum fuel-air ratio as a function of inlet pressure for the three configurations. From figure 9 we can see the effect of the inlet air pressure on ignition performance of the combustors, especially at low pressure.

(2) The inlet air temperature has a strong effect on the ignition performance of the combustors. The effects of the inlet air temperature on maximum ignitable reference velocity and on optimum fuel-air ratio for the three configurations are shown in figures 10 and 11. As the inlet air temperature decreases, the maximum ignitable reference velocity decreases. At higher inlet

air temperatures, the effect of the inlet air temperature on the optimum ignitable fuel-air ratio is very weak; however, at lower inlet air temperatures the effect is very strong, especially for the vaporizer combustor.

Figures 12(a), (b), and (c) show the combined effects of inlet air pressure and temperature on ignition performance for the three configurations.

EXPERIMENTAL STUDY ON AIRFLOW DISTRIBUTION OF THE COMBUSTOR

The airflow distribution characteristics of a combustor directly affect the performance of the combustor such as combustion efficiency, range of stable operation, and temperature profile at the combustor exit. A 90° segment of the annular combustor was used for this study. The test assembly is shown in figure 13.

The goals of the study were as follows:

(1) To determine the effect of Mach number at the combustor inlet on the airflow distribution at an air temperature of 291 K
(2) To compare the changes of airflow distributions with and without burning in the combustor

Figure 13 shows the eight instrumentation sections on the test assembly. The flow rate G_{hi} through the holes on the wall of the flame tube can be calculated as follows:

$$G_{hi} = C_{di} A_{hi} \sqrt{2g\gamma \Delta P}$$

where
C_{di} airflow discharge coefficient of the holes

A_{hi} area of the holes

γ specific gravity of air

ΔP pressure drop through the holes, $= P_{ai}^* - P_{li}$

g acceleration of gravity

The flow rate (in percent) through each row of holes that is relative to the total is

$$\bar{G}_i = 100 \left(G_{hi} \bigg/ \sum_{i=1}^{N} G_{hi} \right)$$

The relative area (in percent) of the holes of each row of holes is

$$\bar{A}_i = 100 \left(A_{hi} \bigg/ \sum_{1}^{N} A_{hi} \right)$$

91

The following conclusions were obtained from this experimental study:

(1) At the range tested, there is no apparent influence on the airflow distribution by the Mach number at the combustor inlet, as shown in figures 14(a) and (b).

(2) Under the conditions

$$T^*_{in} = 291 \text{ K}$$

$$T^*_{ex}/T^*_{in} = 1 \sim 2.44$$

the airflow distributions have no obvious change, regardless of whether burning is present or not, as shown in figures 15(a) and (b). However, we are not certain that this would be true under real operating conditions.

EXPERIMENTAL STUDY ON FUEL INJECTORS

The fuel injector is one of the most important components of a combustor or afterburner. In order to determine the effects of geometric parameters, airflow parameters, and fuel rate on the fuel-spray characteristics, we have made an initial study of a vaporizer and an airblast atomizer.

The test rig assembly is shown in figure 16. The airflow rate G_a through the fuel injector was measured by a turbine flowmeter. The air velocity at the injector exit was

$$V_a = G_a(R)T_2/AP$$

The fuel rate G_f was also obtained by a turbine flowmeter where the air-fuel ratio is given by

$$AFR = G_a/G_f$$

The Sauter mean diameter (SMD) of the fuel spray drops was measured by a Malvern laser particle sizer.

EXPERIMENTAL STUDY ON VAPORIZER FUEL INJECTOR

Since we tried to understand the spray characteristics - not the vaporizing condition - for different vaporizer fuel injectors, we studied the spray characteristics under low inlet air temperature only and did not heat the vaporizer. Some of the test vaporizers are shown in figures 17 and 18.

The following conclusions were made:

(1) The air velocity V_a at the vaporizer exit is the most important factor affecting fuel atomization. As shown in figure 19, SMD decreases with increasing V_a.

(2) The effect of air-fuel ratio on fuel atomization is related to the air velocity at the vaporizer exit. If AFR <4 and the air velocity is low, then, as AFR increases, SMD will decrease. When the air velocity is much higher, the effect is not apparent, as shown in figures 20 and 21.

(3) The method and the pressure of injecting fuel into the vaporizer has no significant influence on fuel atomization, as shown in figure 22.

EXPERIMENTAL STUDY OF THE AIR-BLAST ATOMIZER

The geometric parameters of the airblast atomizers we have tested are listed in the following table:

Number	Inner channel feature	Outer channel feature	Total exit area, mm
0	Straight flow	Tangent flow holes	295.4
11	With swirl vane	Tangent flow holes	295.4
21	Straight flow	Rectangular flow holes	359.5
7	Straight flow	Rectangular flow holes	295.4
17	Straight flow	Rectangular flow holes	235.1
10	With swirl vane	Rectangular flow holes	295.4

The test atomizers are shown in figures 23 and 24.

The conclusions were as follows:

(1) Under the test conditions, SMD decreased with increasing airspray velocity, as shown in figure 25.

(2) When AFR <4, SMD decreased with increasing AFR. When AFR >4, there was no significant influence on SMD, as shown in figure 26.

(3) For the same conditions, SMD decreased as the exit area of the atomizer increased (fig. 27). The reason for such a result has not been determined yet.

There are many interesting subjects related to combustion such as combustor exit temperature profile, the procedure to control exhaust emission, combustor diagnostics, swirl combustion, and cooling techniques. We are prepared to do further experimental study.
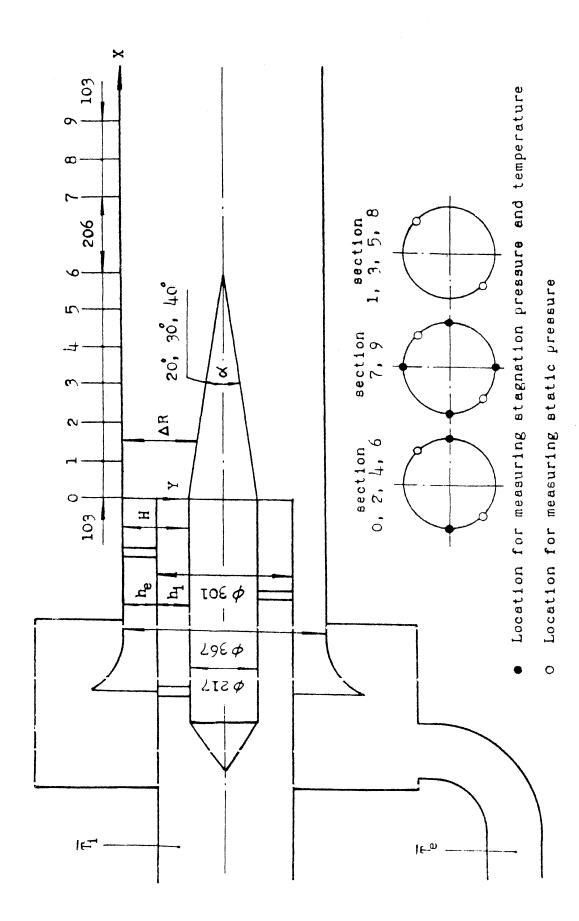
Figure 1. - Test section and measurement locations.

- • Location for measuring stagnation pressure and temperature
- ○ Location for measuring static pressure

section 1, 3, 5, 8

section 7, 9

section 0, 2, 4, 6

94

Y/ΔR

0.1
0.2
0.3
0.4
0.5
0.6
0.7
0.8
0.9
1.0

flow splitter position

test number
004-1

$0\quad 0.2\ 0.4\ 0.6\ 0.8\ 1.0$

T/T_{max}

Figure 3. - Typical, nondimensional diffuser inlet velocity profile.

Y/ΔR

0.1
0.2
0.3
0.4
0.5
0.6
0.7
0.8
0.9
1.0

flow splitter position

test number
008-1   ○
004-1   ●

$0\quad 0.2\ 0.4\ 0.6\ 0.8\ 1.0$

v/v_{max}

Figure 2. - Typical, nondimensional diffuser inlet velocity profile.

Figure 5. – Static-pressure recovery coefficient as function of diffuser axial distance under different nondimensional diffuser flow parameters. A, 024-1 + 024-2; B, 024-3 + 024-4; C, 024-5 + 024-6; D, 024-7 + 024-8.

Figure 4. – Static-pressure recovery coefficient as function of nondimensional axial distance; $\bar{T}_i \sqrt{T_e}$ = constant, $\bar{V}_i \sqrt{V_e}$ = constant.
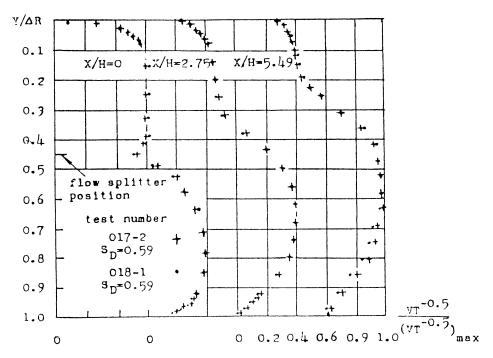
Figure 6. - Nondimensional velocity-temperature combination distribution under constant S_D value for low-temperature and high-temperature tests.
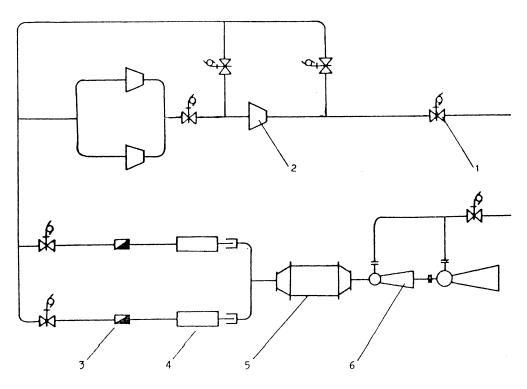
Figure 7. - Air system for high-altitude ignition rig. Solenoid valve, 1; expansion turbine, 2; flow measurement nozzle, 3; test combustor, 4; cooling device, 5; ejector, 6.
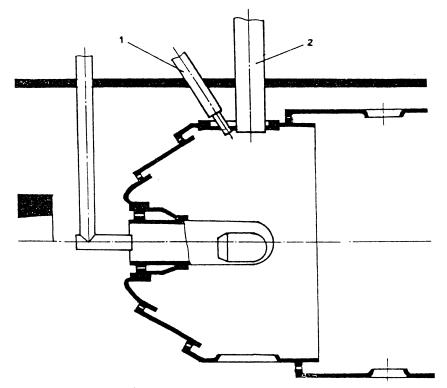
Figure 8. - Installation of ignition plug in vaporizer combustor. Starting fuel injector, 1; high-energy ignition plug, 2.
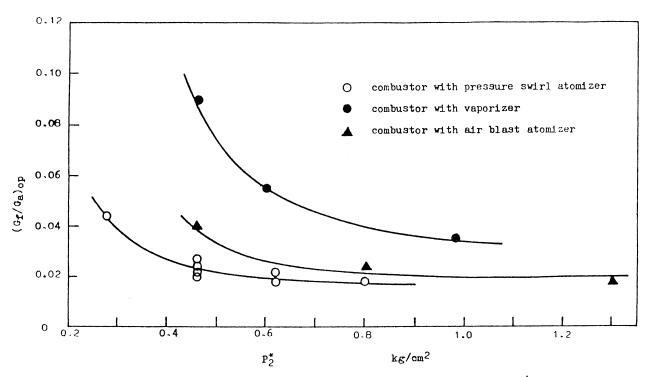
Figure 9. - Optimum fuel-air ratio versus inlet pressure; $T_2^* = 293$ K.
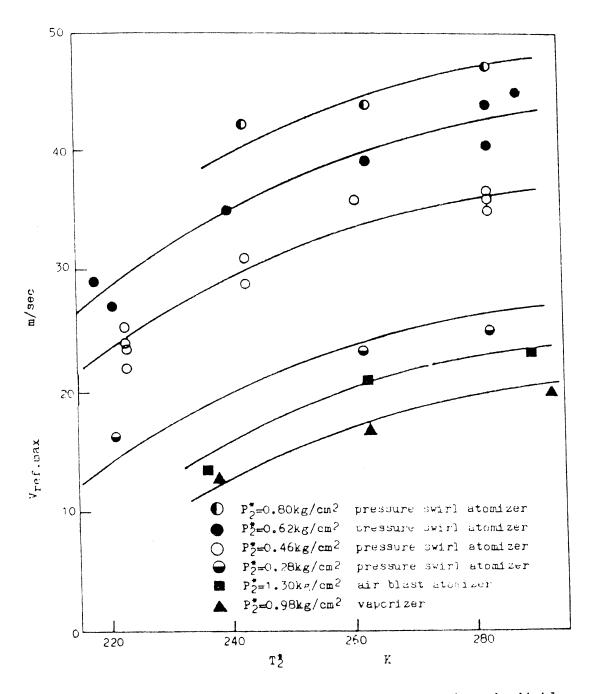
Figure 10. – Effect of inlet temperature on maximum ignitable reference velocity.
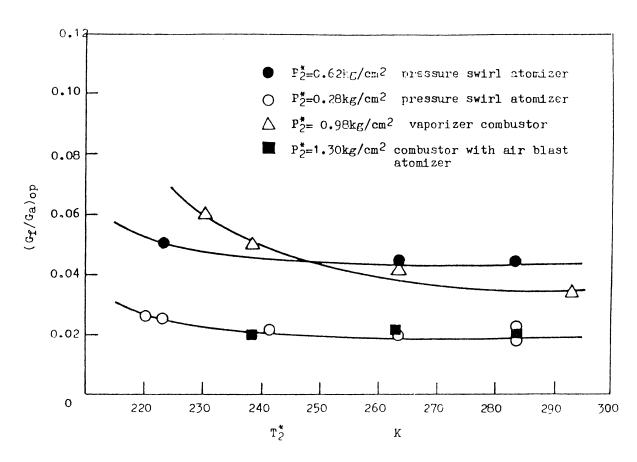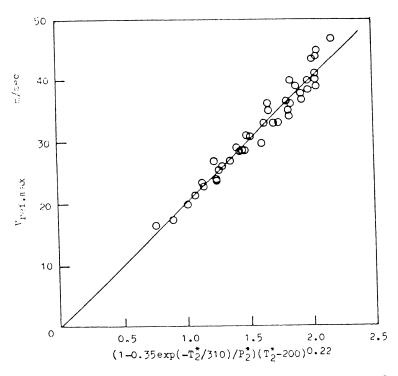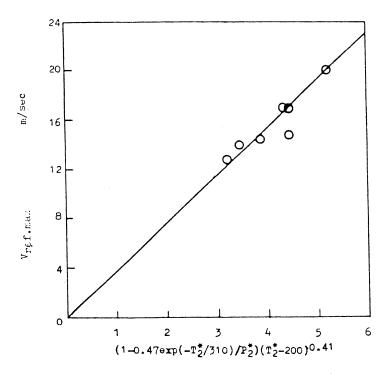
Figure 11. – Effect of inlet temperature on optimum fuel-air ratio.
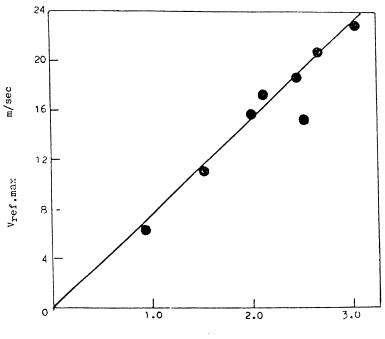
(a) Experimental combustor with pressure swirl atomizer.

(b) Experimental combustor with vaporizer.

Figure 12. - Correlation of maximum ignitable reference velocity with inlet parameters.

101

(c) Experimental combustor with air-blast atomizer.

Figure 12. - Concluded.
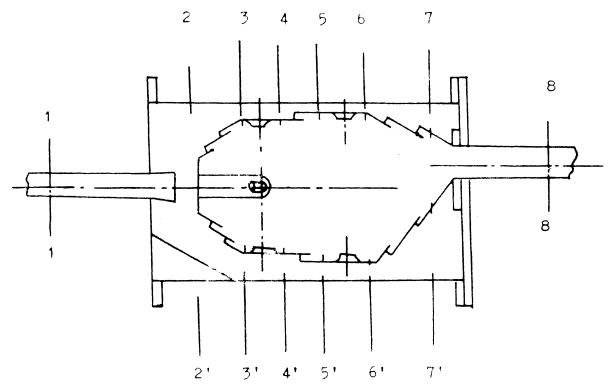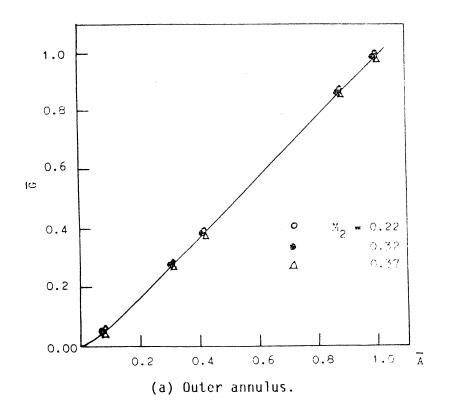
Figure 13. - Test combustor and instrumentation on locations.

(a) Outer annulus.

(b) Inner annulus.
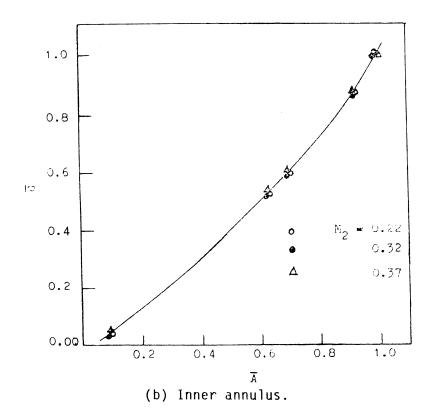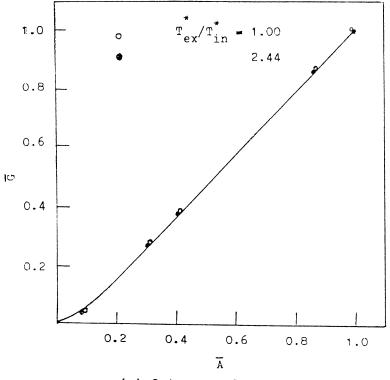
Figure 14. – Effect of Mach number on air-flow
distribution of annulus; $T_{in}^* = 291$ K, $T_{ex}^*/T_{in}^* = 1$.

(a) Outer annulus.

(b) Inner annulus.
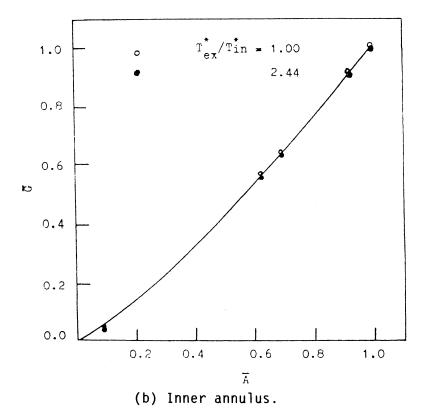
Figure 15. — Effect of combustion on air-flow distribution of annulus.
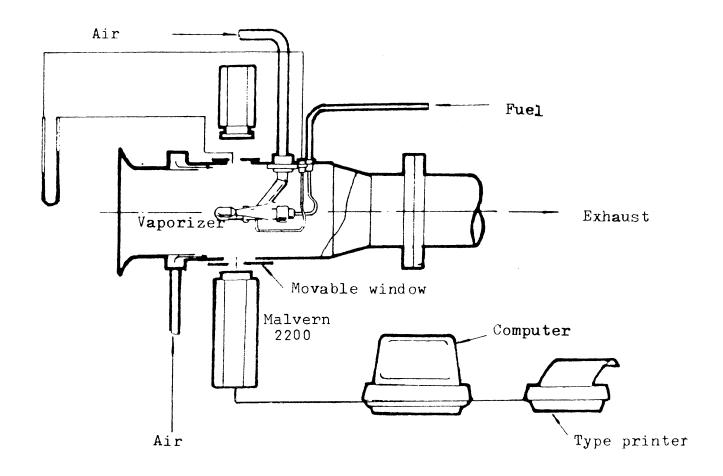
Figure 16. – Test rig assembly.

Figure 17. – Test vaporizers.

Figure 18. – Test vaporizer.

Figure 20. – Effect of air-fuel ratio on SMD for
vaporizer fuel injector #1; L = 50 mm.
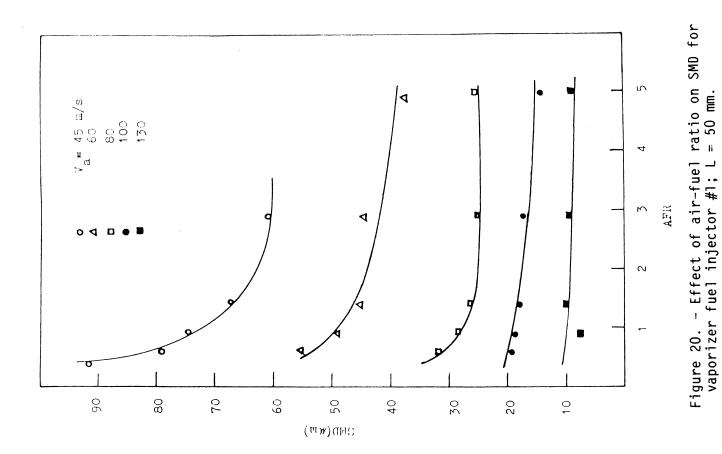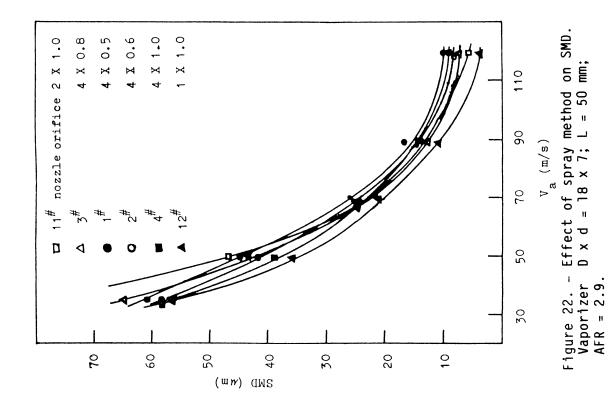
Figure 19. – Effect of air velocity on SMD
for vaporizer fuel injector #1.

107

Figure 22. - Effect of spray method on SMD.
Vaporizer D x d = 18 x 7; L = 50 mm;
AFR = 2.9.

Figure 21. - Effect of air-fuel ratio on SMD for
vaporizer fuel injector #12; L = 50 mm.
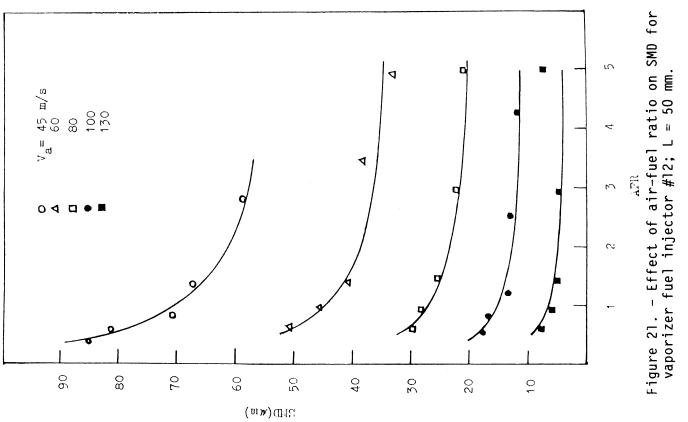
Figure 23. - Test air-blast atomizer.
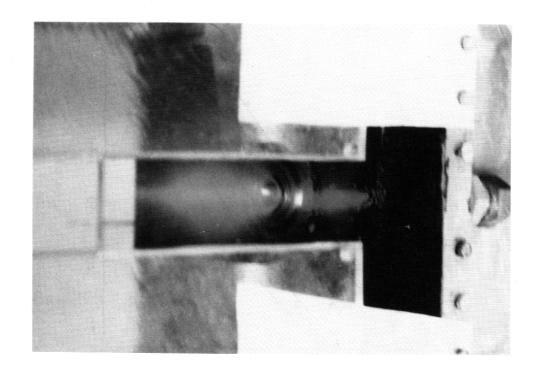
Figure 24. - Test atomizer.
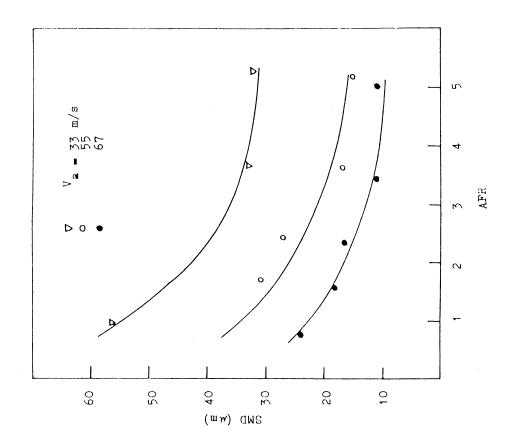
Figure 26. – Effect of air-fuel ratio on SMD for air-blast atomizer #11; L = 38 mm.
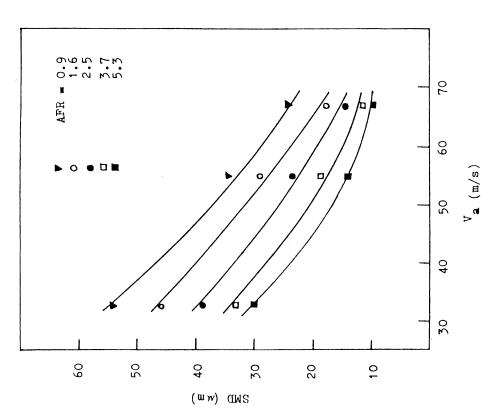
Figure 25. – Effect of air velocity on SMD for air-blast atomizer #11; L = 38 mm.
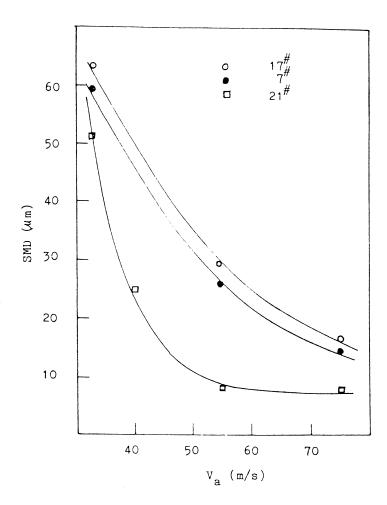
Figure 27. - Effect of nozzle outlet area
on SMD; AFR = 2.5.

THERMODYNAMICS AND COMBUSTION MODELING

Frank J. Zeleznik
Lewis Research Center
Cleveland, Ohio

Modeling fluid phase phenomena blends the conservation equations of continuum mechanics with the property equations of thermodynamics. The thermodynamic contribution becomes especially important when the phenomena involve chemical reactions as they do in combustion systems. The successful study of combustion processes requires (1) the availability of accurate thermodynamic properties for both the reactants and the products of reaction and (2) the computational capabilities to use the properties. A discussion is given of some aspects of the problem of estimating accurate thermodynamic properties both for reactants and products of reaction. Also, some examples of the use of thermodynamic properties for modeling chemically reacting systems are presented. These examples include one-dimensional flow systems and the internal combustion engine.

INTRODUCTION

Modeling fluid phase phenomena always requires a combination of the conservation equations of continuum mechanics with the property functions of thermodynamics. For some applications it is possible to idealize the model so drastically that the continuum equations virtually disappear and the computation becomes wholly thermodynamic. In other situations the thermodynamic properties are so highly idealized that the computation deals solely with the continuum equations. Consequently, thermodynamics and continuum mechanics are often viewed as independent disciplines. However, the complementary nature of the two disciplines is manifested in attempts to generate realistic models of physical systems in which combustion occurs.

The roles of thermodynamics and the conservation equations are easily discerned by examining the relevant equations. The conservation equations (refs. 1 and 2) for mass, species, energy, and momentum are shown in equation (1), where the summation convention is used for an index repeated as a subscript and a superscript:

$$\frac{\partial m}{\partial t} + \nabla_k(mv^k) = 0 = \frac{\delta m}{\delta t} + m\nabla_k v^k$$

$$\frac{\partial(mn_\lambda)}{\partial t} + \nabla_k(mn_\lambda v^k + d_\lambda^k) = R_\lambda$$

$$\frac{\partial(mu)}{\partial t} + \nabla_k(muv^k) = -\nabla_k(q^k + \mu^\lambda d_\lambda^k) + \tau^{kj}\nabla_j v_k - m\frac{\partial\Omega}{\partial t} - v^k f_k = m\frac{\delta u}{\delta t} \qquad (1)$$

$$m\frac{\delta v^k}{\delta t} = F^k = -mg^{ki}\nabla_i\Omega + f^k + \nabla_j\tau^{kj}$$

$$\tau^{kj} = -pg^{kj} + \Delta\tau^{kj}$$

In these equations, m is the mass density, u the internal energy per unit mass, n_λ the moles per unit mass of species λ, v^k the velocity, q^k the heat flux, μ^λ the chemical potential per mole of species λ, d_λ^k the diffusive flux of species λ, and R_λ the volumetric rate of production of species λ. In the momentum equation, g^{ki} is the metric tensor for three-dimensional space, τ^{kj} is the stress tensor, Ω is the potential energy, and f^k represents all volumetric forces over and above those produced by the stress and the potential energy. The stress tensor is composed of a contribution from the pressure p and the dissipative stresses. The symbol t represents time, ∇_k is the covariant derivative with respect to the spatial coordinates, and $\delta/\delta t = \partial/\partial t + v^k \nabla_k$ is known as the absolute, substantial, or convective derivative. The thermodynamic property functions for pressure, internal energy, and the chemical potentials are shown in equation (2). These properties may be regarded as functions of mass density, temperature T, and moles per unit mass of the species:

$$p = p(m,T,n_\lambda)$$

$$u = u(m,T,n_\lambda) \tag{2}$$

$$\mu^\lambda = \mu^\lambda(m,T,n_\tau)$$

Substitution of the thermodynamic internal energy function into the conservation equation for internal energy converts it into an equation for the temperature, and the resulting equation now contains explicit contributions from changes in composition and mass density. In reacting fluids the temperature largely reflects the energy released or absorbed by chemical reactions. Thus, we see that the thermodynamic property of internal energy determines the temperature and, consequently, the amount of energy released or absorbed. Of course, the temperature, in turn, strongly affects reaction rates and other physical properties of the reacting fluid. The thermodynamic pressure equation (an equation of state) appears in the equation for the conservation of momentum and thus helps to define the local flow field. Clearly, the successful modeling of combustion processes requires two ingredients: (1) accurate thermodynamic properties for both the reactants and the products of reaction and (2) computational capabilities to use the properties in modeling combustion systems.

I shall briefly describe some aspects of our work on the two topics of property estimation and property utilization. First, I shall discuss the estimation of free radical properties in the ideal gas state and the properties of nonideal solutions. Following the discussion of properties, I shall illustrate some of our computational capabilities to use these properties to model the physical systems in which reactions take place.

ESTIMATION OF FREE RADICAL PROPERTIES

Free radicals are highly reactive species which are usually present at low concentrations in chemically reacting systems. These species play an important role in the chemical reaction mechanisms of combustion. They are involved in both the endothermic (heat absorbing) initiation steps of the mechanism and the exothermic (heat releasing) recombination steps. Recently Bauer and Zhang (ref. 3) and others have conjectured that free radicals are also important

species in the mechanism of soot formation in hydrocarbon flames. Hence, the thermodynamic properties of free radicals are of considerable interest. Unfortunately, relatively little is known about the thermodynamic properties of radicals over the extended temperature range encountered in combustion systems. Hence, we have found it necessary to estimate the thermodynamic properties of the phenyl, phenoxy, and biphenyl free radicals which are likely to be important species in the combustion of hydrocarbons and in soot formation. Because of their low concentrations and because most combustion processes take place at relatively low pressures and high temperatures, it is usually adequate to estimate free radical properties in the ideal gas state.

Thermodynamic properties for any species in an ideal gas state can be estimated from the canonical partition function using the formulas of statistical thermodynamics. This requires knowledge of the species' molecular structure, its vibrational and rotational energy levels, any barriers to internal rotation, and the standard state heat of formation. The difficulty is that this information is seldom available for free radicals. As a result it becomes necessary to estimate these data from similar, stable species whose molecular properties have been measured. These stable, related species are called the parent species of the radicals. The species benzene, phenol and biphenyl are suitable parent species for the radicals phenyl, phenoxy and o-biphenyl, respectively. The relation between these parent species and the radicals is shown in figure 1. This estimation procedure is based on the work of Forgeteg and Berces (ref. 4). In this method it is usual to assume that the bond lengths and bond angles of the radical are identical to those of the parent. Also the radical's vibrational frequencies are taken to be the same as those of the parent molecule except that three frequencies are eliminated for each atom which appears in the parent molecule but not in the radical. In some cases, where additional information about the radical is available, the assumed structure and vibrational frequencies can be adjusted to take into account this extra information.

One of the difficulties with this method of estimation is the selection of the appropriate frequencies for elimination. The reason for this is that a molecule's frequencies correspond to vibrations of the molecule as a whole rather than vibrations of a particular bond. Naturally this introduces some uncertainty into the resulting properties. To ascertain the degree of uncertainty one might try eliminating different frequencies or, perhaps, perform the estimation with a different parent species.

Comparisons of the results of our estimation of phenyl and phenoxy properties (ref. 5) with estimates made by Benson, et al. (refs. 6 and 7) are shown in tables I and II for entropy and heat capacity. Our estimation of the phenyl properties from benzene and phenol agree surprisingly well with each other and with the room temperature values estimated by Benson. Our estimates of the phenoxy properties estimated from phenol also agree very well with Benson's estimates which, for this species, were available over an extended temperature range.

NONIDEAL SOLUTION MODELS

The properties of fuels and oxidizers must be accurately known if combustion processes are to be modeled properly. Since reactants, especially fuels, are often multicomponent, nonideal, liquid solutions, it is desirable

to have accurate mathematical representations of the composition dependence of their thermodynamic properties. Such representations (solution models) can be used to analyze, interpolate and extrapolate thermodynamic measurements of nonideal solutions. Solution models can also be used for the calculation of equilibria. The utility of a solution model is directly proportional to its ability to handle both a wide range of nonideal behaviors and a great diversity of multicomponent systems.

Many solution models have been proposed, but most of them have a limited capacity to treat nonideality. Some of them either are only able to deal with relatively small deviations from ideality or cannot handle the complete composition range. Others are limited to binary or ternary solutions. Still others exhibit undesirable mathematical behavior. Many contain nonlinear parameters which greatly complicate the analysis of experimental measurements. I have proposed a solution model (ref. 8) which overcomes most of these difficulties. The model is applicable to solutions containing an arbitrary number of constituents. It can treat highly nonideal solutions, electrolyte and non-electrolyte, over the complete composition range. It has a relatively simple mathematical form, and all parameters appear linearly in the model. Finally, it contains both ideal and regular solutions as special cases. The model's expression for the Gibbs free energy is given in equation (3) where G is the Gibbs free energy, x_i is the mole fraction of species i, $\varphi^{(\ell)}$ represents the elementary symmetric functions, and $\mu_{jk}^{(\ell)}$, and $\epsilon_{jk}^{(\ell)}$ are functions of temperature and pressure.

$$G = \sum_{\ell=1}^{N} \varphi^{(\ell)}(x_i;N) \sum_{j=1}^{N} \sum_{k=1}^{N} \left(\mu_{jk}^{(\ell)} + \epsilon_{jk}^{(\ell)} \ln x_j \right) x_j x_k$$

$$= \sum_{\ell=1}^{N} \varphi^{(\ell)}(x_i;N) G^{(\ell)}(x_i) \qquad (3)$$

I shall illustrate the flexibility and the capabilities of the model by demonstrating how it handles three very different, highly nonideal solutions (ref. 9).

The first solution is the ethanol-heptane binary system, for which there are three sets of excess enthalpy measurements at 30 °C. The solution is endothermic, and measurements extend into the very dilute solution range. The representation of the measurements by the solution model is shown in figure 2. Clearly the model reproduces the data very well over the complete composition range, including the steep gradient that occurs in the dilute ethanol region. The second solution is the chloroform-ethanol binary solution at 50 °C, whose excess enthalpy exhibits exothermic behavior over a part of the composition range and endothermic behavior over the rest of the range. The representation of the data is shown in figure 3, and again the data are well represented by the model. These two solutions display very different behavior yet both can be accommodated easily by the same solution model.

The first two examples were nonelectrolyte solutions. The last example is an electrolyte solution of sodium chloride in water. Measurements for this system extend from the very dilute solutions to saturated solutions and cover a temperature range of almost 200 °C. A comparison between the measurements and the model are shown in figures 4 to 7, where the composition is given as

molality (g mol of solute/kg solvent). Figures 4 to 6 show the integral heats of solution while the excess heat capacity is shown in figure 7. Once again the model gives more than an adequate representation of the experimental measurements.

CHEMICAL REACTION EQUILIBRIA

Sometimes the behavior of chemically reacting systems can be predicted quite well on the basis of chemical equilibrium. Over the years we have developed a capability to perform computations reliably for several applications involving chemical reactions (refs. 10 to 16). The calculations are based on free energy minimization and assume that the gaseous phase behaves ideally, that the condensed phases are pure liquids and solids, and that the volume of the condensed phases is negligible. The computations can evaluate composition and, also, thermodynamic and transport properties for complex chemical systems involving up to 20 chemical elements and 600 reaction products.

Composition and properties can be calculated for a thermodynamic state defined by pressure and one of the three variables: temperature, enthalpy, or entropy. Alternatively, the thermodynamic state can be specified by assigning the volume and one of the three variables temperature, internal energy, or entropy. In addition to the calculation of compositions and properties for an assigned thermodynamic state, we can also compute the results for three different one-dimensional flow processes neglecting heat transfer effects: (1) rocket nozzle expansions, (2) incident and reflected shocks, and (3) Chapman-Jouguet detonations. The rocket nozzle and shock calculations can be performed for either equilibrium or frozen compositions. Table III is an example of the calculation of the composition and of the thermodynamic and transport properties for a simple system composed of hydrogen and oxygen at assigned pressures and temperatures. Table IV illustrates the results for the calculation of a one-dimensional shock in a hydrogen-oxygen mixture diluted with argon.

MODELING THE SPARK-IGNITED INTERNAL COMBUSTION ENGINE

The spark-ignited internal combustion engine is an example of a chemically reacting system for which purely thermodynamic predictions are inadequate. A realistic model must take into account not only thermodynamic properties but also heat transfer rates, finite rate chemistry (chemical kinetics), and intake and exhaust flow rates. These effects lead to a complex model and difficult calculations.

A schematic representation of the operation of the spark-ignited internal combustion engine is shown in figure 8. Each cycle of the operation can be described qualitatively by dividing the cycle into four parts, each part spanning π radians (180°) of crankangle. Each part corresponds approximately to one of four processes taking place in the engine. The parts are given names which are reasonably descriptive of the four processes: (1) the intake stroke, (2) the compression stroke, (3) the power stroke and (4) the exhaust stroke. A fuel-air mixture enters the cylinder during the intake stroke and is compressed by the piston during the compression stroke. The compressed working fluid is ignited and expanded during the power stroke and is expelled from the

cylinder during the exhaust stroke. Because matter enters and leaves the cylinder, the internal combustion engine is an open system. Furthermore, the burned gases are not completely expelled from the cylinder, and thus the residual gases provide a "memory" of each cycle for the subsequent cycle. Each cycle occurs rapidly with a cycle repetition rate which ranges from about 25 to 250 msec. This cycle repetition rate is comparable to the time scale for the complex chemistry which takes place during combustion, and thus the rates of chemical reactions become important. The engine has a movable boundary (the piston) and a complex geometry. Finally, the operation of the engine is nonrepeatable, and the engine experiences "cycle-to-cycle" variations. These features of the internal combustion engine make its modeling difficult indeed. Additionally, often there is insufficient information to describe completely the details of the engine operation even if it were mathematically and numerically possible.

I have chosen to develop (ref. 17) a hierarchy of models of differing complexity in order to accommodate the varying amounts of information available in particular cases. The models range from a simple model requiring only thermodynamic properties (modeling level 1) to a complex model demanding full combustion kinetics, transport properties and poppet valve flow characteristics (modeling level 5). The members of the hierarchy are classified according to their treatment of several important features of the internal combustion engine as shown in table V. The description of the operation of the internal combustion engine as being divided into four parts is adequate for a qualitative description. It is, however, inadequate to describe the operation of a real engine corresponding to modeling at levels 4 and 5. The timing for the initiation and cessation of important events in a more realistic cycle is sketched in figure 9. This figure, often referred to as an indicator diagram, is a plot of working fluid pressure as a function of cylinder volume for one complete cycle spanning 4π radians (720°) of crankangle. It should be noted that between stations 7 and 2 the intake and the exhaust valves are simultaneously open; this corresponds to what is called the valve-overlap portion of the cycle.

I shall use the fuel-rich combustion of gaseous propane with air as an example of modeling the internal combustion engine at level 5. The air is humidified (75 percent relative humidity), and recirculated exhaust gas is 10 percent of the charge. The calculation was a multicycle calculation, but only cycle 11 is shown. The modeling parameters and a summary of results for cycle 11 are given in table VI. The combustion of propane was given a full kinetic treatment using a mechanism of 121 reactions. Figures 10 to 15 are plots of some of the calculated quantities. Straight line segments are apparent on some of these plots. These are not indicative of the accuracy of the calculations but rather reflect both the number of points saved for plotting and the scale of the plots. Figure 10 shows the indicator diagram for cycle 11. Figure 11 shows the fraction of working fluid which has been converted to burned, but still reacting, gas during the combustion phase of the cycle. The burned and unburned gas temperatures are shown in figure 12 (both temperatures were calculated during the combustion phase of the cycle). The quenching effect of the endothermic initiation reactions is clearly visible. The carbon monoxide concentration in mole percent is shown in figure 13. Here we can easily see the freezing of carbon monoxide early in the power stroke. A similar plot for nitric oxide, as parts per million in mole fraction, also shows freezing in figure 14. Finally, in figure 15 is a history of the mass content of the cylinder during cycle 11.

REFERENCES

1. Zeleznik, Frank J.: Thermodynamics J. Math. Phys., vol. 17, no. 8, Aug. 1976, pp. 1579-1610.

2. Zeleznik, Frank J.: Thermodynamics. II. The Extended Thermodynamic System. J. Math. Phys., vol. 22, no. 1, Jan. 1981, pp 161-178.

3. Bauer, S.H.; and Zhang, L.M.: Shock-Tube Pyrolysis of Polycyclic Aromatics-Detection of Soot Precursors. Shock Tubes and Waves. Proceedings of the 14th International Symposium on Shock Tubes and Shock Waves. R.D. Archer, and B.E. Milton, eds., Sydney Shock Tube Symposium Publishers, Sydney, Australia, 1983, pp. 654-661.

4. Forgeteg, S.; and Berces, T.: Estimation of Entropy and Heat of Formation of Free Radicals. I. Statistical Thermodynamic Calculation of Entropies. Acta Chim. Acad. Sci. Hung., vol. 51, no. 2, 1967, pp. 205-215.

5. Burcat, Alexander; Zeleznik, Frank J.; and McBride, Bonnie J.: Ideal Gas Thermodynamic Properties for the Phenyl, Phenoxy and o-Biphenyl Radicals. NASA TM-83800, 1985.

6. Benson, S.W.: Thermochemical Kinetics. Second ed., Wiley, 1976.

7. Colussi, A.J.; Zabel, F; and Benson, S.W.: The Very Low-Pressure Pyrolysis of Phenyl Ethyl Ether, Phenyl Allyl Ether, and Benzyl Methyl Ether and the Enthalpy of Formation of the Phenoxy Radical. Int. J. Chem. Kinet., vol. 9, no. 2, 1977, pp. 161-177.

8. Zeleznik, Frank J.: A Class of Nonideal Solutions. I-Definition and Properties. NASA TP-1929, 1983.

9. Zeleznik, Frank J.; and Donovan, Leo F.: A Class of Nonideal Solutions. II- Application to Experimental Data. NASA TP-1930, 1983.

10. Gordon, Sanford; McBride, Bonnie J.; and Zeleznik, Frank J.: Computer Program for Calculation of Complex Chemical Equilibrium Compositions and Applications. Supplement I-Transport Properties. NASA TM-86885, 1984.

11. Gordon, Sanford; and McBride, Bonnie J.: Computer program for Calculation of Complex Chemical Equilibrium Compositions, Rocket Performance, Incident and Reflected Shocks, and Chapman-Jouguet Detonations. NASA SP-273, 1976.

12. Svehla, Roger A.; and McBride, Bonnie J.: Fortran IV Computer Program for Calculation of Thermodynamic and Transport Properties of Complex Chemical Systems. NASA TN D-7056, 1973.

13. Zeleznik, F.J.; and Gordon, S.: Calculation of Complex Chemical Equilibria. Ind. Eng. Chem., vol. 60, no. 6, June 1968, pp. 27-57.

14. Gordon, Sanford; and Zeleznik, Frank J.: A General IBM 704 or 7090 Computer Program for Computation of Chemical Equilibrium Compositions, Rocket Performance, and Chapman-Jouguet Detonations. Supplement 1 - Assigned Area-Ratio Performance. NASA TN D-1737, 1963.

15. Zeleznik, Frank J.; and Gordon, Sanford: A General IBM 704 or 7090 Computer Program for Computation of Chemical Equilibrium Compositions, Rocket Performance, and Chapman-Jouguet Detonations. NASA TN D-1454, 1962.

16. Gordon, Sanford; Zeleznik, Frank J.; and Huff, Vearl N.: A General Method for Automatic Computation of Equilibrium Compositions and Theoretical Rocket Performance of Propellants. NASA TN D-132, 1959.

17. Zeleznik, Frank J.; and McBride, Bonnie J.: Modeling the Internal Combustion Engine. NASA RP-1094, 1985.

TABLE I. - COMPARISON OF PROPERTIES FOR
PHENYL RADICAL[a]

Property	Benson (ref. 6)	Estimated from benzene	Estimated from phenol
S^0_{300}	69.4	69.03	69.30
$C^0_{p\,300}$	18.8	18.96	19.51
$C^0_{p\,500}$	----	31.03	31.70
$C^0_{p\,1000}$	----	46.59	46.93
$C^0_{p\,3000}$	----	59.04	59.09

[a]All values as eu (cal/g-mol K).

CD-85-17235

TABLE II. - COMPARISON OF PROPERTIES
FOR PHENOXY RADICAL[a]

Property	Benson (ref. 6)	From phenol
S^0_{300}	73.7	73.70
$C^0_{p\,300}$	22.5	22.64
$C^0_{p\,400}$	29.8	29.82
$C^0_{p\,500}$	35.8	35.80
$C^0_{p\,600}$	40.6	40.57
$C^0_{p\,800}$	47.5	47.48
$C^0_{p\,1000}$	52.3	52.17

[a]All values as eu (cal/g-mol K).

CD-85-17236

120

TABLE III.

THERMODYNAMIC EQUILIBRIUM PROPERTIES AT ASSIGNED

TEMPERATURE AND PRESSURE

CASE NO. 6668

	WT FRACTION (SEE NOTE)	ENERGY KJ/KG-MOL	STATE	TEMP DEG K
CHEMICAL FORMULA				
FUEL H 2.00000	1.000000	-9012.332	L	20.27
OXIDANT O 2.00000	1.000000	-12978.762	L	90.18

O/F= 7.9370   PERCENT FUEL= 11.1894   EQUIVALENCE RATIO= 1.0000   PHI= 1.0000

THERMODYNAMIC PROPERTIES

P, MPA	0.10132	0.10132	0.10132	0.10132	0.10132	0.10132	0.10132	0.10132	0.10132	0.10132	0.10132
T, DEG K	5500.0	5000.0	4500.0	4000.0	3500.0	3000.0	2500.0	2000.0	1500.0	1000.0	500.0
RHO, KG/CU M	1.3416-2	1.4967-2	1.7468-2	2.3376-2	3.8936-2	6.2488-2	8.5005-2	1.0938-1	1.4635-1	2.1955-1	4.3909-1
H, KJ/KG	55513.9	52669.0	47251.0	33833.1	12360.5	-1457.79	-6953.36	-9278.31	-10745.6	-11979.6	-13038.5
U, KJ/KG	47961.3	45899.1	41450.5	29498.5	9758.19	-3079.30	-8145.34	-10204.6	-11438.0	-12441.1	-13269.2
G, KJ/KG	-123677.1	-107511.2	-91736.2	-76960.8	-64513.3	-54702.2	-46385.9	-38774.8	-31609.1	-24892.6	-18767.8
S, KJ/(KG)(K)	32.5802	32.0360	30.8861	27.6985	21.9640	17.7481	15.7730	14.7483	13.9090	12.9130	11.4586
M, MOL WT	6.055	6.141	6.450	7.672	11.182	15.383	17.438	17.951	18.013	18.015	18.015
(DLV/DLP)T	-1.00811	-1.02147	-1.06320	-1.15917	-1.16898	-1.06245	-1.01196	-1.00121	-1.00004	-1.00000	-1.00000
(DLV/DLT)P	1.0831	1.2419	1.7935	3.2778	3.8474	2.2710	1.2997	1.0382	1.0015	1.0000	1.0000
CP, KJ/(KG)(K)	4.6981	7.2046	16.3371	38.8059	39.0979	17.2068	6.6083	3.3997	2.6424	2.2907	1.9548
GAMMA (S)	1.5032	1.3668	1.2355	1.1639	1.1268	1.1106	1.1235	1.1705	1.2124	1.2523	1.3091
SON VEL,M/SEC	3369.4	3041.9	2677.0	2246.2	1712.4	1341.9	1157.2	1041.3	916.2	760.2	549.6

TRANSPORT PROPERTIES (GASES ONLY)
   CONDUCTIVITY IN UNITS OF MILLIWATTS/(CM)(K)

VISC,MILLIPOISE	1.3674	1.2723	1.1761	1.0869	1.0207	0.94586	0.83841	0.70639	0.55364	0.37747	0.17324

WITH EQUILIBRIUM REACTIONS

CP, KJ/(KG)(K)	4.6844	7.2044	16.3359	38.8069	39.1072	17.2071	6.6077	3.3935	2.6423	2.2907	1.9548
CONDUCTIVITY	12.6667	16.4726	31.4208	70.9281	79.3619	34.1601	9.6648	3.2468	1.7354	0.9740	0.3603
PRANDTL NUMBER	0.5057	0.5564	0.6115	0.5947	0.5030	0.4764	0.5732	0.7383	0.8430	0.8878	0.9398

WITH FROZEN REACTIONS

CP, KJ/(KG)(K)	3.5289	3.5100	3.4743	3.3857	3.2373	3.1124	2.9951	2.8393	2.6140	2.2907	1.9548
CONDUCTIVITY	10.3699	9.6043	8.7109	7.4819	5.8067	4.3630	3.3449	2.4942	1.7049	0.9740	0.3603
PRANDTL NUMBER	0.4653	0.4650	0.4691	0.4918	0.5691	0.6747	0.7507	0.8041	0.8488	0.8878	0.9398

MOLE FRACTIONS

H	0.66077	0.65095	0.61751	0.50212	0.25268	0.05763	0.00517	0.00012	0.00000	0.00000	0.00000
HO2	0.00000	0.00000	0.00000	0.00003	0.00008	0.00005	0.00001	0.00000	0.00000	0.00000	0.00000
H2	0.00387	0.01037	0.03230	0.10047	0.18534	0.13479	0.04283	0.00581	0.00020	0.00000	0.00000
H2O	0.00002	0.00018	0.00213	0.02961	0.23353	0.64341	0.91089	0.98950	0.99968	1.00000	1.00000
O	0.33098	0.32663	0.31048	0.24985	0.11877	0.02421	0.00182	0.00003	0.00000	0.00000	0.00000
OH	0.00363	0.00967	0.02972	0.08948	0.15096	0.09367	0.02331	0.00214	0.00004	0.00000	0.00000
O2	0.00073	0.00219	0.00786	0.02845	0.05865	0.04624	0.01596	0.00238	0.00009	0.00000	0.00000

ADDITIONAL PRODUCTS WHICH WERE CONSIDERED BUT WHOSE MOLE FRACTIONS WERE LESS THAN 0.50000E-05 FOR ALL ASSIGNED CONDITIONS

H2O2   O3   H2O(S)   H2O(L)

CD-85-17226

TABLE IV.

SHOCK WAVE PARAMETERS ASSUMING
EQUILIBRIUM COMPOSITION FOR INCIDENT SHOCKED CONDITIONS

CASE NO.   1207

		MOLES	ENERGY CAL/MOL	STATE	TEMP DEG K
	CHEMICAL FORMULA				
FUEL	H 2.00000	0.050000	13.324	G	300.00
FUEL	O 2.00000	0.050000	12.952	G	300.00
FUEL	AR 1.00000	0.900000	9.191	G	300.00

O/F= 0.0000 PERCENT FUEL= 100.0000   EQUIVALENCE RATIO= 0.5000   PHI= 0.0000

INITIAL GAS (1)

MACH NO.	3.3528	3.5052	3.6576	3.8100	3.9624	4.1148	4.2672	4.4196	4.5720	4.7244
U1, M/SEC	1100.00	1150.00	1200.00	1250.00	1300.00	1350.00	1400.00	1450.00	1500.00	1550.00
P, ATM	0.01316	0.02632	0.02632	0.02632	0.02632	0.02632	0.02632	0.02632	0.02632	0.02632
T, DEG K	300.0	300.0	300.0	300.0	300.0	300.0	300.0	300.0	300.0	300.0
RHO, G/CC	2.0126-5	4.0252-5	4.0252-5	4.0252-5	4.0252-5	4.0252-5	4.0252-5	4.0252-5	4.0252-5	4.0252-5
H, CAL/G	0.25457	0.25457	0.25457	0.25457	0.25457	0.25457	0.25457	0.25457	0.25457	0.25457
U, CAL/G	-15.578	-15.578	-15.578	-15.578	-15.578	-15.578	-15.578	-15.578	-15.578	-15.578
G, CAL/G	-371.94	-360.97	-360.97	-360.97	-360.97	-360.97	-360.97	-360.97	-360.97	-360.97
S, CAL/(G)(K)	1.2407	1.2041	1.2041	1.2041	1.2041	1.2041	1.2041	1.2041	1.2041	1.2041
M, MOL WT	37.654	37.654	37.654	37.654	37.654	37.654	37.654	37.654	37.654	37.654
CP, CAL/(G)(K)	0.1372	0.1372	0.1372	0.1372	0.1372	0.1372	0.1372	0.1372	0.1372	0.1372
GAMMA (S)	1.6249	1.6249	1.6249	1.6249	1.6249	1.6249	1.6249	1.6249	1.6249	1.6249
SON VEL,M/SEC	328.1	328.1	328.1	328.1	328.1	328.1	328.1	328.1	328.1	328.1

SHOCKED GAS (2)--INCIDENT--EQUILIBRIUM

U2, M/SEC	666.94	602.16	576.32	560.44	549.22	540.35	532.52	524.96	517.29	509.40
P, ATM	0.10778	0.27659	0.32363	0.36873	0.41405	0.46053	0.50878	0.55917	0.61191	0.66707
T, DEG K	1528.1	1693.3	1817.1	1932.4	2044.1	2153.0	2258.8	2360.3	2456.7	2547.3
RHO, G/CC	3.3195-5	7.6873-5	8.3812-5	8.9778-5	9.5277-5	1.0057-4	1.0582-4	1.1118-4	1.1672-4	1.2248-4
H, CAL/G	91.697	114.97	132.65	149.45	166.17	183.16	200.60	218.59	237.18	256.35
U, CAL/G	13.067	27.830	39.138	49.982	60.929	72.259	84.165	96.788	110.22	124.45
G, CAL/G	-1940.61	-2079.42	-2225.77	-2363.02	-2496.51	-2627.06	-2753.88	-2875.57	-2990.89	-3098.89
S, CAL/(G)(K)	1.3300	1.2959	1.2979	1.3002	1.3026	1.3052	1.3080	1.3109	1.3140	1.3172
M, MOL WT	38.619	38.617	38.614	38.608	38.597	38.579	38.551	38.510	38.452	38.378
(DLV/DLP)T	-1.00001	-1.00002	-1.00005	-1.00011	-1.00021	-1.00041	-1.00073	-1.00123	-1.00193	-1.00286
(DLV/DLT)P	1.0003	1.0008	1.0019	1.0038	1.0070	1.0125	1.0209	1.0330	1.0492	1.0695
CP, CAL/(G)(K)	0.1403	0.1420	0.1443	0.1478	0.1532	0.1613	0.1728	0.1883	0.2078	0.2308
GAMMA (S)	1.5795	1.5700	1.5576	1.5403	1.5165	1.4859	1.4497	1.4110	1.3734	1.3400
SON VEL,M/SEC	720.9	756.6	780.6	800.6	817.2	830.3	840.4	848.0	854.1	859.9

TRANSPORT PROPERTIES (GASES ONLY)
  CONDUCTIVITY IN UNITS OF MILLICALORIES/(CM)(K)(SEC)

VISC,MILLIPOISE	0.72845	0.77927	0.81611	0.84959	0.88129	0.91160	0.94048	0.96775	0.99326	1.0169

  WITH EQUILIBRIUM REACTIONS

CP, CAL/(G)(K)	0.1396	0.1415	0.1431	0.1478	0.1522	0.1613	0.1728	0.1882	0.2078	0.2308
CONDUCTIVITY	0.1536	0.1678	0.1786	0.1992	0.2158	0.2576	0.3087	0.3799	0.4721	0.5823
PRANDTL NUMBER	0.6619	0.6573	0.6539	0.6304	0.6215	0.5706	0.5264	0.4796	0.4371	0.4031

  WITH FROZEN REACTIONS

CP, CAL/(G)(K)	0.1396	0.1401	0.1405	0.1408	0.1411	0.1413	0.1416	0.1418	0.1420	0.1422
CONDUCTIVITY	0.1536	0.1658	0.1747	0.1829	0.1907	0.1984	0.2058	0.2131	0.2201	0.2270
PRANDTL NUMBER	0.6619	0.6587	0.6563	0.6540	0.6519	0.6495	0.6669	0.6440	0.6406	0.6368
P2/P1	8.191	10.511	12.298	14.012	15.734	17.500	19.334	21.248	23.253	25.349
T2/T1	5.094	5.644	6.057	6.441	6.814	7.177	7.529	7.868	8.189	8.491
M2/M1	1.0256	1.0256	1.0255	1.0253	1.0250	1.0246	1.0238	1.0227	1.0212	1.0192
RHO2/RHO1	1.6493	1.9098	2.0822	2.2304	2.3670	2.4984	2.6290	2.7621	2.8997	3.0428
V2(U1-U2)M/SEC	433.06	547.84	623.68	689.56	750.78	809.65	867.48	925.04	982.71	1040.60

MOLE FRACTIONS

AR	9.2306-1	9.2302-1	9.2294-1	9.2279-1	9.2254-1	9.2211-1	9.2144-1	9.2045-1	9.1909-1	9.1732-1
H	1.2073-7	8.7884-7	4.2747-6	1.5554-5	4.7175-5	1.2409-4	2.8829-4	5.9812-4	1.1195-3	1.9103-3
HO2	4.6101-8	1.5001-7	2.8252-7	4.7303-7	7.3544-7	1.0786-6	1.5029-6	1.9983-6	2.5453-6	3.1190-6
H2	2.6458-6	1.1305-5	3.5151-5	8.8613-5	1.9569-4	3.8922-4	7.0587-4	1.1754-3	1.8088-3	2.5906-3
H2O	5.1241-2	5.1163-2	5.1019-2	5.0770-2	5.0361-2	4.9725-2	4.8791-2	4.7502-2	4.5833-2	4.3804-2
H2O2	6.699-10	2.448 -9	4.449 -9	7.237 -9	1.097 -8	1.574 -8	2.147 -8	2.796 -8	3.485 -8	4.173 -8
O	2.8572-6	1.2578-5	3.9852-5	1.0208-4	2.2885-4	4.6242-4	8.5400-4	1.4542-3	2.3021-3	3.4157-3
OH	7.5326-5	2.0713-4	4.3641-4	8.0004-4	1.3432-3	2.1036-3	3.0994-3	4.3177-3	5.7144-3	7.2211-3
O2	2.5622-2	2.5587-2	2.5527-2	2.5430-2	2.5285-2	2.5082-2	2.4818-2	2.4497-2	2.4133-2	2.3738-2

ADDITIONAL PRODUCTS WHICH WERE CONSIDERED BUT WHOSE MOLE FRACTIONS WERE LESS THAN 0.50000E-08 FOR ALL
  ASSIGNED CONDITIONS

O3   H2O(S)   H2O(L)

CD-85-17225

TABLE V. - MODELING LEVELS

Feature	Modeling level				
	5	4	3	2	1
Flow	Poppet valve formulas		Zero-pressure-drop flow; flow reversal only at $\theta = 0$ or $\theta = 3\pi$, where discontinuities are possible		
Flame	Kinetic	Equilibrium			
Flame propagation	Mass burning formulas				Instantaneous
Burned-gas chemistry	Finite rate			Equilibrium	
Heat transfer	Nonzero				Zero

TABLE VI.

INTERNAL COMBUSTION ENGINE MODEL ZMOTTO   CYCLE 11   LEVEL 5   CASE NO.   111
    REF: ZELEZNIK, FRANK J.; AND MCBRIDE, BONNIE J.: MODELING THE INTERNAL COMBUSTION ENGINE. NASA RP-1094, 1985.

COMPRESSION RATIO = 10.5   RPM = 3500.0   EGR = 0.100   T(EGR) = 900.6 K   SPARK ADVANCE = 20.00 DEG
FUEL PRESSURE = 1.00000 ATM   MANIFOLD PRESSURE = 0.42760 ATM   EXHAUST PRESSURE = 1.00000 ATM
FLOWS ARE ISENTROPIC
BORE = 10.922 CM   STROKE = 10.312 CM   ROD = 17.145 CM   CHAMBER AREA =129.030 SQ CM   WALL TEMP = 360.0 K
TOTAL VOLUME = 1067.83 CC   DISPLACEMENT VOLUME = 966.13 CC

IVOPEN = 699.00 DEG   IVSHUT = 265.00 DEG   EVOPEN = 465.00 DEG   EVSHUT = 45.00 DEG

HEAT TRANSFER PARAMETERS   C1 =   0.000000   C2 = 0.387200E 00   C3 =   0.000000   A = 0.4000   B = 0.8000

    KINETIC FLAME   FINITE BURNING INTERVAL = 88.7 DEG   WIEBE   COMBUSTION   TAU =0.8930E-04 SEC   BETA =   3.200

		CHEMICAL FORMULA			WT FRACTION	ENERGY CAL/MOL	STATE	TEMP DEG K
FUEL	C 3.00000 H 8.00000				1.000000	-24821.770	G	298.15
AIR	N 1.56168 O 0.41959	AR 0.00936	C 0.00032		*1.000000	-1386.340	G	298.15
	* AIR INCLUDES 0.02348 MOLE FRACTION WATER				RELATIVE HUMIDITY= 0.7500			

            A/F= 12.5823   PERCENT FUEL=   7.3625   EQUIVALENCE RATIO= 1.2500   PHI=   1.2647
                        PERFORMANCE PARAMETERS FOR ONE CYLINDER

MASS PER CYCLE (G)		MEAN INLET MASS FLOW RATE (G/SEC)		MEAN EXHAUST MASS FLOW RATE (G/SEC)	
TOTAL	0.49685	CHARGE	12.6027	EXHAUST	13.2527
FUEL	0.02860	FUEL	0.8351	CO	0.71753
AIR	0.35987	AIR	10.5073	NOX	0.00013
		NET	12.6376	NET	13.2526

ENERGY PER CYCLE (JOULES)		AVERAGE ENERGY RATE - POWER (KW)		CYCLE EFFICIENCIES	
INDICATED WORK	404.672	INDICATED POWER	11.803	NET WORK	0.243361
INDICATED PUMP WORK	-86.886	INDICATED PUMP POWER	-2.534	HEAT LOSS	0.269577
HEAT LOSS	352.020	HEAT LOSS RATE	10.267	EXHAUST	0.435675
CHEM. ENERGY	1305.823	EXHAUST POWER	16.593		

                                    MISCELLANEOUS
            INDICATED MEAN EFFECTIVE PRESSURE (ATM)   4.1338
            PUMP MEAN EFFECTIVE PRESSURE (ATM)   -0.8876
            MEAN TORQUE (NEWTON-METERS)   25.2886

COMPOSITE EXHAUST GAS MOLE FRACTIONS AT 900.63 K AND 1.0000 ATM   MOLECULAR WEIGHT = 26.947
    AR   0.007952   CH4   0.000914   CO   0.052088   CO2   0.077497   C2H2   0.002239
    C2H4   0.000131   H2   0.026569   H2O   0.169476   NO   0.000009   N2   0.663041
    O2   0.000070

FRESH CHARGE MOLE FRACTIONS AT 292.50 K AND 0.4276 ATM   MOLECULAR WEIGHT = 29.192
    AR   0.000861   CH4   0.000099   CO   0.005643   CO2   0.008395   C2H2   0.000243
    C2H4   0.000014   H2   0.002878   H2O   0.018359   N2   0.071827   O2   0.000008
    C3H8   0.043867   AIR   0.847803

NOTE: INLET AND EXHAUST VALUES CALCULATED WHEN THE VALVES CLOSE.

COMPUTER CYCLE TIME= 48.858 SEC

PHENYL

H   •   H
 \ / \ /
  | |
 / \ / \
H   H
    H

BENZENE

    H
    |
H   H
 \ / \ /
  | |
 / \ / \
H   H
    |
    H

PHENOXY

    •
    O
H   H
 \ / \ /
  | |
 / \ / \
H   H
    H

PHENOL

    OH
    |
H   H
 \ / \ /
  | |
 / \ / \
H   H
    |
    H

o-BIPHENYL

H   H H   H
 \ | | /
H —   — H
 / | | \
H   H H   H

BIPHENYL

H   H H   H
 \ | | /
H —   — H
 / | | \
H   H H   H
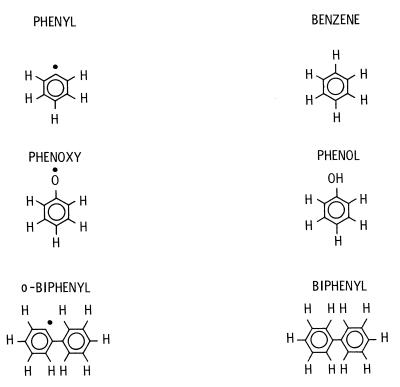
Figure 1. - Radicals and parent species.
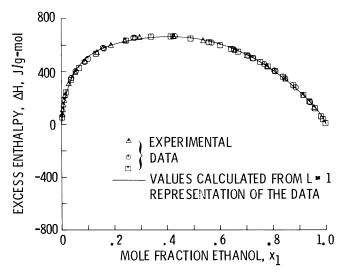

Figure 2. - Excess enthalpy of ethanol (1) - heptane
(2) binary system at 30 °C.
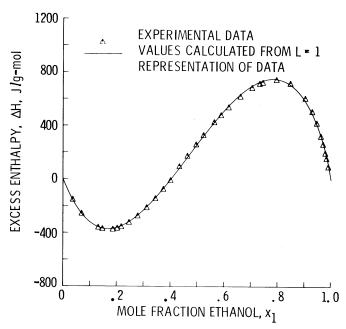
Figure 3. - Excess enthalpy of chloroform (1) -
ethanol (2) binary system at 50 °C.
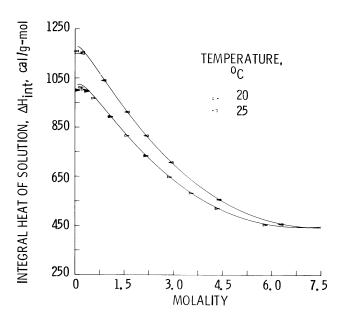
Figure 4. - Integral heat of solution of sodium
chloride in water.
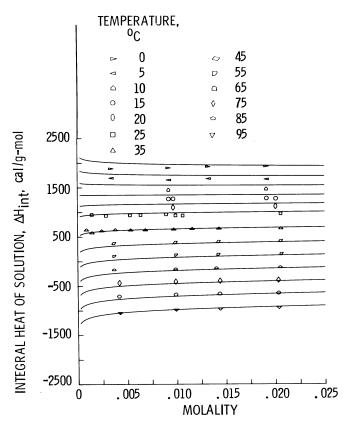
Figure 5. – Integral heat of solution of sodium
chloride in water.

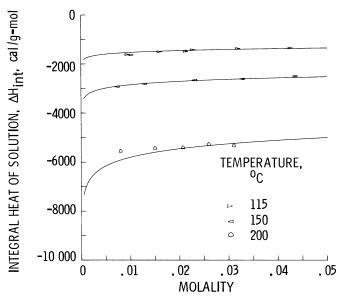Figure 6. – Integral heat of solution of sodium
chloride in water.
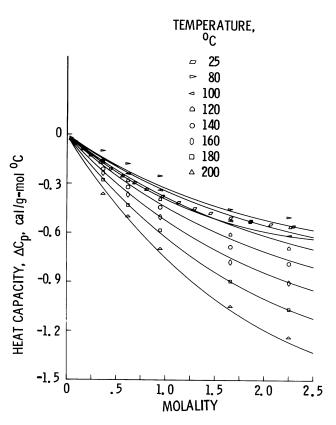
Figure 7. - Excess heat capacity of aqueous
sodium chloride solutions.

INTAKE STROKE, $0 \leq \theta \leq \pi$

COMPRESSION STROKE, $\pi \leq \theta \leq 2\pi$

POWER STROKE, $2\pi \leq \theta \leq 3\pi$

EXHAUST STROKE, $3\pi \leq \theta \leq 4\pi$

CD-85-17217
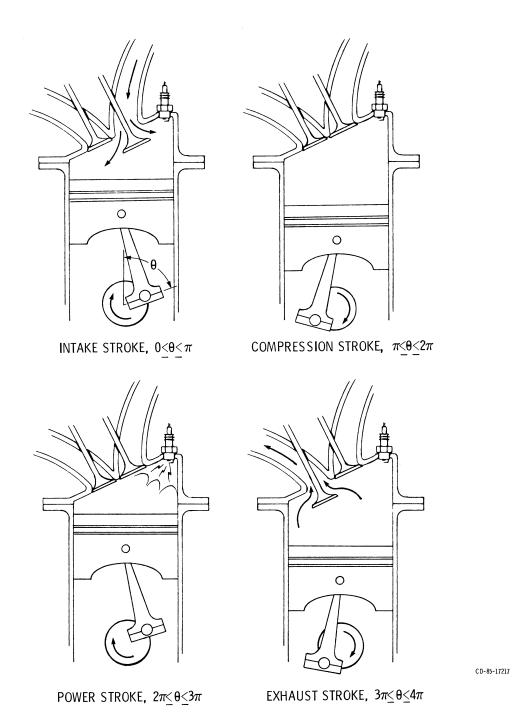
Figure 8. - Four-stroke operation of spark-ignited internal combustion engine.

STATION	CRANKANGLE
1	0
2	$\theta_C^{(-)}$ (EXHAUSE VALVE CLOSES)
3	$\theta_C^{(+)}$ (INTAKE VALVE CLOSES)
4	θ_0 (BURNING BEGINS)
5	θ^* (BURNING ENDS)
6	$\theta_0^{(-)}$ (EXHAUST VALVE OPENS)
7	$\theta_0^{(+)}$ (INTAKE VALVE OPENS)
8	720^0

CD-85-17234
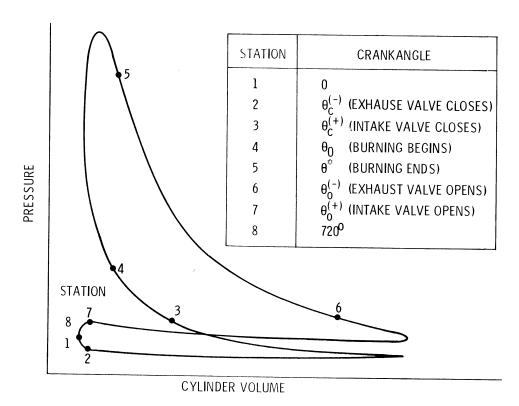
Figure 9. - Stations for modeling levels 4 and 5.

OTTO CYCLE INDICATOR DIAGRAM

08/27/85
CASE   111
CYCLE   11

CD-85-17221

Figure 10.

130

OTTO CYCLE BURNED MASS AND VOLUME FRACTIONS

08/27/85
CASE   111
CYCLE   11

VOLUME

MASS

MB/M AND VB/V

CRANKANGLE, DEG

CO-85-17220

Figure 11.

OTTO CYCLE TEMPERATURE

08/27/85
CASE   111
CYCLE   11

BURNED

UNBURNED

TEMPERATURE, DEG K

CRANKANGLE, DEG

CO-85-17223

Figure 12.

131

CO CONCENTRATION (BURNED GAS DURING COMBUSTION)

Figure 13.

NO CONCENTRATION (BURNED GAS DURING COMBUSTION)

Figure 14.

132

Figure 15.

EFFECT OF FLAME-TUBE HEAD STRUCTURE ON COMBUSTION CHAMBER PERFORMANCE

Gu Minqqi
Shenyang Aero-Engine Research Institute
Shenyang, People's Republic of China

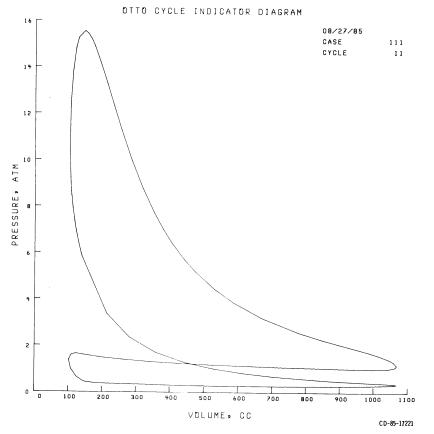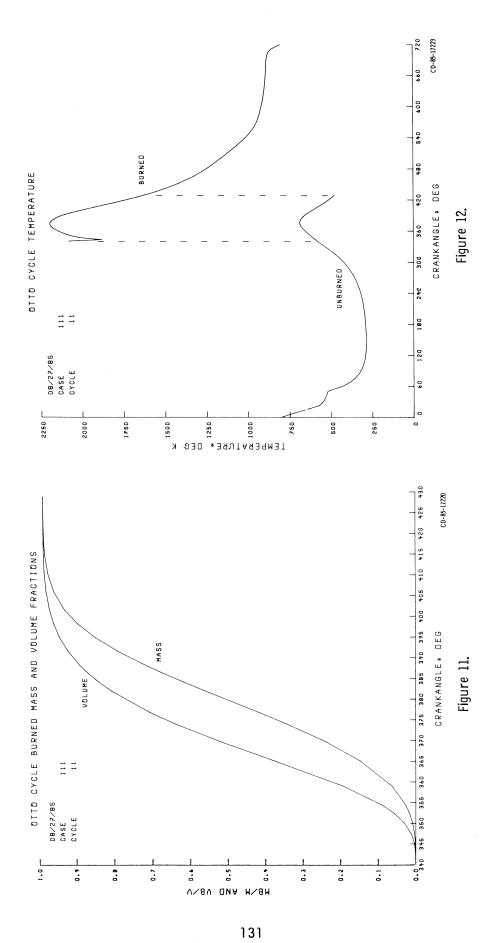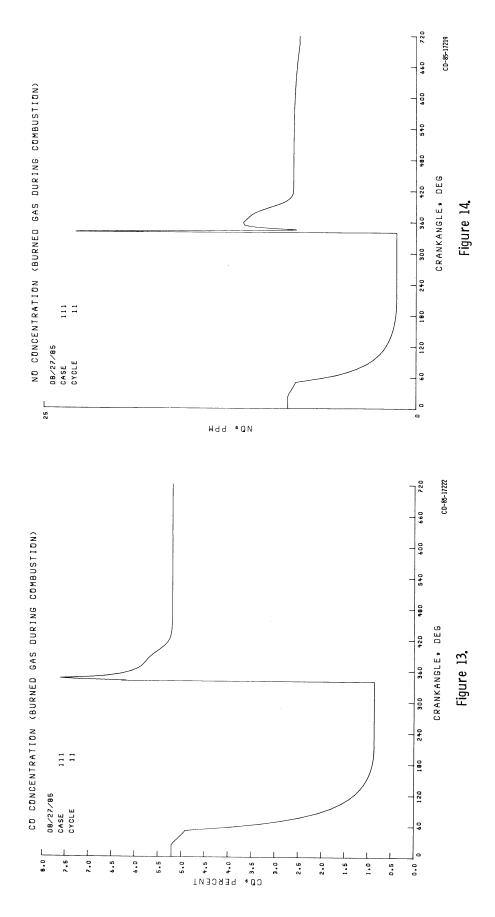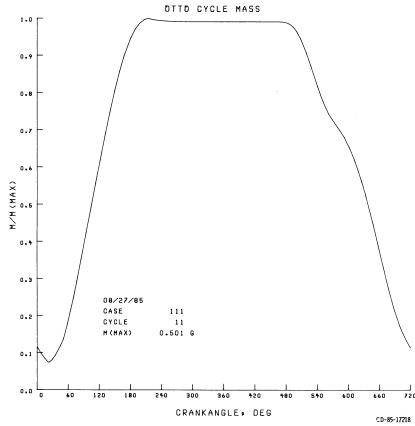This paper presents the experimental combustion performance of a pre-mixed, pilot-type flame tube with various head structures. The test study covers an extensive area: efficiency of the combustion chamber, quality of the outlet temperature field, limit of the fuel-lean blowout, ignition performance at ground starting, and carbon deposition. As a result of these tests, a nozzle was found which fits the premixed pilot flame tube well. The use of this nozzle optimized the performance of the combustion chamber.

The tested models had premixed pilot chambers with two types of air-film-cooling structures, six types of venturi-tube structures, and secondary fuel nozzles with two small spray-cone angles.

INTRODUCTION

After a period of engine operation, a premixed pilot-type flame tube (fig. 1) with a pressurized fuel nozzle may have difficulty in starting. Sometimes the pilot chamber may not ignite at all; this seriously affects the starting performance of the engine. This problem is generally believed to be due to carbon deposition in the premixed pilot chamber (8 g carbon deposited in a single premixed pilot chamber after 190 min of running). In the case of high-load running, the gas temperature in the center of the premixed pilot chamber can be raised as high as 1200 °C; this can make the high-density fuel spray crack and deposit on the downstream section of the nozzle. In addition, the wall temperature would be high, causing the fuel spray to form coke on the wall, which (coupled with fuel deposition) would make the wall rough. Then the carbon particles would hit the cores of deposition and would be deposited on the wall. Thus, the wall becomes uneven and very rough. When the fuel spray again hits the wall and flows on its uneven soft carbon layer, the fuel film is also very uneven (unlike the film on a smooth metal wall). As a result, the spray quality becomes very poor and the engine fails to start.

The objective of this experiment was to improve the ground starting performance while not damaging the other types of combustion performance. The study concentrated on the effect of premixed pilot chamber structures and nozzle spray angles on combustion performance.

This paper presents a study of the effect on combustion of (1) pre-mixed pilot chambers with air-film-cooling and venturi-tube structures and (2) small-angle secondary nozzles. It emphasizes their effects on ground starting performance and on carbon deposition within the pilot chambers.

TEST MODELS

Premixed Pilot Chamber With Air-Film-Cooling Structure

It is known that the air-film-cooling structure enables free carbon particles to be carried away by the film-cooling air flow, thus reducing or

avoiding the contact of these particles with the wall. This helps reduce the wall temperature. Two models were evaluated (fig. 2). Eighty film-cooling holes (ϕ2) were added to the wall of these two premixed pilot chambers. The ratio of the cooling-hole opening area to the total opening area in the flame tube wall was 0.022. The air velocity in the outlet of the air-film-cooling ring was 15 to 26 m/sec.

Premixed Pilot Chamber With Venturi-Tube Structure

A venturi tube was mounted in the rear of the swirler (fig. 3). It made the fuel injected from the nozzle hit the venturi-tube wall and then mix with the air coming from the inner section of the swirler, thus avoiding contact of the fuel with the flame tube wall. In addition, because the venturi tube was used, the position of the recirculation zone moved further downstream of the nozzle; as a result, the temperature of the carbon-generating zone downstream of the fuel nozzle was reduced. This helped reduce the carbon particles.

Six venturi tubes of different sizes were evaluated. (See table I and fig. 4.) The ratio of the outer to the inner area of the swirler was 1.16 when the venturi tube was mounted.

Secondary Nozzle With Small Spray Angle

Fuel entered from the centrifugal nozzle in the ignition process in order to reduce or eliminate the probability of the sprayed fuel hitting the wall. Two kinds of small spray-angle secondary nozzles were studied. (See table II and fig. 5.) The spray angle was made small enough that the spray would not hit the inner wall of the premixed pilot chamber. Thus, the fuel spray cone was not impaired. The fuel-air ratio was appropriate near the ignitor, and a good starting performance was maintained (even if there was carbon deposition in the pilot chamber).

RESULTS AND ANALYSIS

Amount of Carbon Deposition in Premixed Pilot Chamber

The experimental results for various models are listed in table III. (Results for the original flame tube are included for comparison.) The results indicate that the venturi tube is the best structure for eliminating carbon deposition. There was almost no carbon deposition in the pilot chamber, and there was only a small amount of carbon deposition in the 20- to 30-mm position downstream of the pilot chamber exit. The objective of reducing carbon deposition in the pilot chamber was achieved.

Results from the water analog test indicate that there was no recirculation zone in the venturi tube. The recirculation zone in the premixed pilot chamber was located far downstream of the nozzle (fig. 6). The heat radiation from the flame-tube center to the nozzle was blocked outside of the venturi tube, thus reducing the temperature downstream of the nozzle. This had a determinate effect on the reduction of the carbon particles. It was for

this reason that the amount of carbon deposition in the flame tube with a venturi tube was obviously reduced.

Adding an air-film-cooling structure in the premixed pilot chamber helped reduce carbon deposition. The reduction rate was usually as much as 20 to 30 percent near the air-film exits. But, at the exits of the air films, the air velocity was small, so was the air-flow momentum. Nevertheless, the momentum of the fuel injected from the nozzle was rather large, so the film flow could not prevent the fuel droplets from hitting the wall. It is only possible for the film air to bring away free carbon particles. For this reason, this structure is not very effective in reducing carbon deposition.

Ground Starting Performance

The results for five models at the ground starting ignition condition are shown in figures 7 and 8 where V_2 is the inlet velocity of the combustion chamber. The curves of figure 7 indicate that there is an optimal value for each curve. This velocity ranges from 15 to 20 m/sec. The ignition performance was best for the flame tube with a model I venturi tube.

Figure 8 indicates that the ground starting ignition performance improved greatly when model I and II nozzles were used under carbon deposition conditions in the premixed pilot chamber. At 17.5 m/sec of inlet velocity the fuel-lean ignition limit improved; the limiting air-fuel ratio increased from 36.8 to 63.2. It is readily seen from these results that, under the carbon deposition condition in the premixed pilot chamber, adoption of a small-angle secondary nozzle obviously improves the ground starting ignition performance.

In addition, it is known from the curves that when carbon is deposited in the premixed pilot chamber the air-fuel ratio of the fuel-lean ignition limit decreases from 47 to 36. This confirms that carbon deposition in the premixed pilot chamber deteriorates the ground starting ignition performance.

Outlet Temperature Field of Combustion Chamber

Table IV shows the test results of various venturi-tube models. It is readily seen from the table that the size of the venturi tube mounted in the premixed pilot chamber has a great effect on the combustor outlet temperature field. The outlet temperature distribution factor (OTDF, table IV) of the model V combustion chamber was 0.155; this was much better than that for the original model (0.229). The OTDF's of models I and II were similar to that of the original model, but those of models IV and VI were inferior to that of the original model.

The convergent angle of the front section and the outlet angle of the venturi tube have an obvious effect on the combustor outlet temperature distribution. When the convergent angle of the front section of the venturi tube increases, the uniformity of the combustor outlet temperature field decreases. When the convergent angle was increased from 27°34' to 67°22', the OTDF increased from 0.209 to 0.301. When the venturi-tube outlet angle became rather small, excessive fuel concentrated in the center of the flame tube; this caused the temperature to rise in the center region and the outlet

temperature distribution to deteriorate. For example, reducing the outlet angle of the venturi tube from 88° to 56° increased the OTDF from 0.155 to 0.301.

Adoption of a secondary nozzle with a small spray angle also improved the uniformity of the combustor outlet temperature field - the OTDF of model II was 0.175, the radial temperature distribution factor (RTDF, table IV) was 0.077.

Stability of Combustion Chamber

Figure 9 shows experimental results of the fuel-lean blowout limit for various models. The shapes of the curve are nearly the same for various models. The fuel-lean blowout limit for the model II venturi tube was wider because this venturi tube had no throat section; thus, a small recirculation zone was formed inside the venturi tube. The size of the recirculation zone was limited to the nozzle diameter range (fig. 10).

The fuel-lean blowout limits of the model III, IV, and V venturi tubes were narrower. It is known from water analog test results that there is a high-speed rotating flow in the throat section of a venturi tube (fig. 11). This unstable flow deteriorates the fuel-lean blowout limit.

When a secondary nozzle with a small spray angle was adopted, the fuel-lean blowout limit improved in the wide velocity range.

CONCLUSIONS

This study led to the following conclusions:

(1) Adoption of the secondary nozzle with a small spray angle not only solves the engine's starting ignition problem when there is carbon deposition in the premixed pilot chamber but also extends the ground starting ignition range and improves the uniformity of the combustor outlet temperature field.

(2) Adoption of an air-film-cooling structure reduces the amount of carbon deposition on the wall of the premixed pilot chamber. But since there is only limited cooling air available, it is not easy to totally eliminate the carbon deposition in the premixed pilot chamber.

(3) Mounting the venturi tube in the rear of the swirler is effective in eliminating carbon deposition in the premixed pilot chamber. But the geometry of the venturi tube affects the uniformity of the combustor outlet temperature field and the ground starting ignition performance; therefore, characteristic geometric parameters of the venturi tube have to be elaborately adjusted.

BIBLIOGRAPHY

Gu, M.Q.: Study of Premixed Pilot Chamber With Air Film Cooling Structure. December 13, 1980.

Liu, Q.G.: Investigation of Carbon Deposition Performance on the Wall of a Flame Tube. April 28, 1980.

Shang, M.Z.: Effect on Igniting Performance for Different Flame Tubes and Fuel Nozzles. June 10, 1982.

Yang, A.L.: Report of Water Analog on Solving the Carbon Deposition Failure of Flame Tubes. April 10, 1982.

Yang, X.Z.: Test Report of Ground Starting Ignition of a Combustion Chamber. September 20, 1981.

TABLE I. - CHARACTERISTIC DIMENSIONS OF VENTURI TUBE

Model	Inlet Diameter, mm	Length, mm	Throat diameter, mm	Outlet cone angle, deg	Outlet diameter, mm
I	42	36	30	56°	40
II		25	42	36°32'	45.3
III		25	30	56°	40
IV		20	30	56°	35
V		20	30	88°	40
VI		15	15	0°	15

TABLE II. - CHARACTERISTICS OF NOZZLE

Model	Spray angle, α_{sec}, deg	Fuel flow, $G_{f_{sec}}$, liter/hr	α_{double}, deg	$G_{f_{double}}$, liter/hr
	Fuel supply pressure, $P_{T_{sec}} = 10$ kg/cm^2		Fuel supply pressure, $P_{T_{double}} = 30$ kg/cm^2	
Original	91	24.6	103	602.4
I	51	24.6	100	602.4
II	62	23.16	100	593.4

TABLE III. - EFFECT OF VARIOUS MODELS
ON CARBON DEPOSITION

[Test conditions at inlet of combustion chamber: air pressure, P_2^*, 6 kg/cm^2; air temperature, T_2^*, 595 K; air flow, G_a, 3.135 kg/sec; air-fuel ratio, a/f, 70; test duration, 2.5 hr.]

Model	Amount of carbon deposition, g	Relative percentage
Original flame tube	1.3	100
Model I venturi tube	.072	5.54
Model VI venturi tube	0	0
Model I air film cooling	1.076	82.8
Model II air film cooling	.932	71.7

TABLE IV. - EFFECT OF VENTURI-TUBE GEOMETRY ON PERFORMANCE OF COMBUSTION CHAMBER

[Test conditions at inlet of combustion chamber: air pressure, P_2^*, 6 kg/cm^2; air temperature, T_2^*, 695 K; air flow, G_a, 3 kg/sec; air-fuel ratio, a/f, 52.2.]

Model	Original	I	II	III	IV	V	VI
Inlet convergent angle	------	27°34'	------	62°	67°22'	67°22'	122°
Outlet cone angle	------	56°	------	56°	56°	88°	------
^{a}OTDF	0.229	0.209	0.223	0.236	0.301	0.155	0.406
^{a}RTDF	.083	.143	.098	.133	.138	.085	.110
$^a n_c$	.984	.984	.975	.988	.997	.979	.929

^{a}OTDF $= (T_{3max}^* - T_2^*)/(T_{3av}^* - T_2^*)$; RTDF $= (T_{3max(h)} - T_2^*)/(T_{3av}^* - T_2^*)$; and

n_c = efficiency of combustion chamber where T_{3av}^* is the average combustion

outlet temperature, T_{3max}^* the maximum combustor outlet temperature, and $T_{3max(h)}^*$

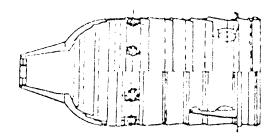the maximum combustor outlet temperature along the blade height.

140

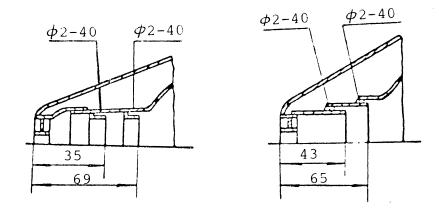Figure 1. - Flame tube with premixed pilot
chamber (original model).

Figure 2. - Scheme of air-film-cooling structure.
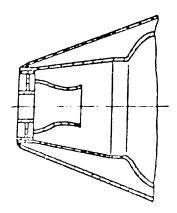(See table I.)
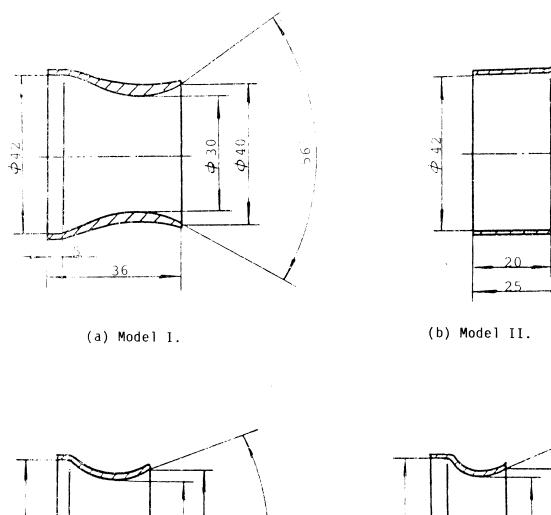
Figure 3. - Scheme of head of flame tube with
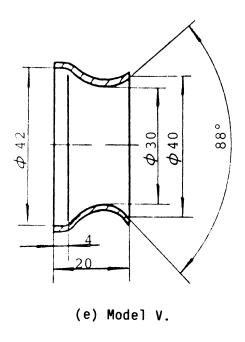venturi tube.

(a) Model I.

(b) Model II.

(c) Model III.

(d) Model IV.
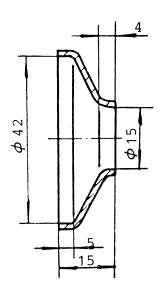
Figure 4. - Structures of venturi-tube models I to VI.

142

(e) Model V.   (f) Model VI.

Figure 4. – Concluded.
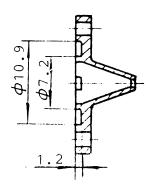
Figure 5. – Secondary nozzle.

143
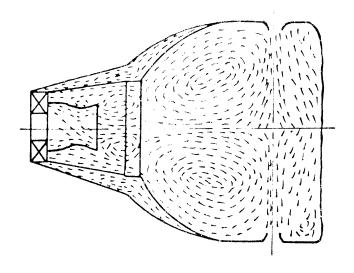
Figure 6. - Flow spectrum in flame-tube head
with model I venturi tube.
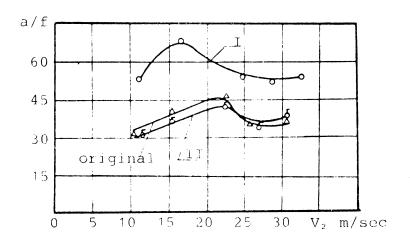
Figure 7. - Effect of venturi-tube size on
ground ignition performance. Test condi-
tions at combustion chamber inlet: air
pressure, P_2^*, 1.04 kg/cm^2; air tempera-
ture, T_2^*, 331 K.
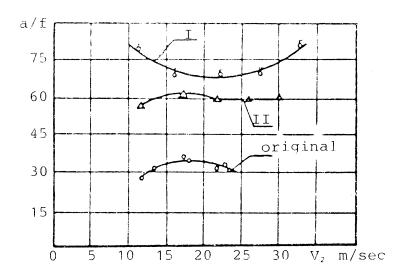
Figure 8. - Effect of fuel spray angle on
ground ignition performance with carbon
deposition in premixed pilot chamber.
Test conditions at combustion chamber
inlet: air pressure, P_2^*, 104 kg/cm^2;
air temperature, T_2^*, 311 K.

Figure 9. - Fuel-lean limits of various models. Test conditions at combustion chamber inlet: air pressure, P_2^*, 4.75 kg/cm², air temperature, T_2^*, 655 K.
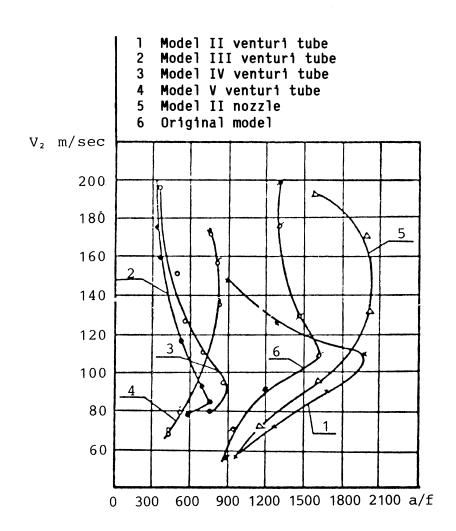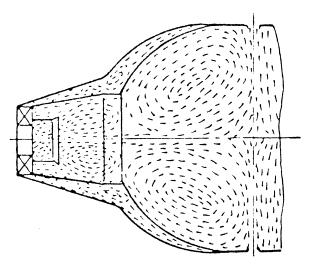
Figure 10. - Flow spectrum in flame-tube head
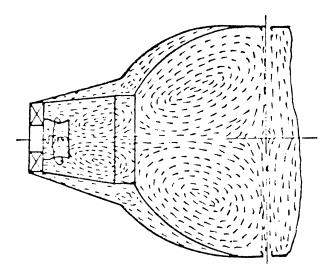with model II venturi tube.

Figure 11. - Flow spectrum in flame-tube head
with model III venturi tube.

EXPERIMENTS AND MODELING OF DILUTION JET FLOW FIELDS

James D. Holdeman
NASA Lewis Research Center
Cleveland, Ohio

This paper presents experimental and analytical results of the mixing of single, double, and opposed rows of jets with an isothermal or variable-temperature main stream in a straight duct. This study was performed to investigate flow and geometric variations typical of the complex, three-dimensional flow field in the dilution zone of gas-turbine-engine combustion chambers.

The principal results, shown experimentally and analytically, were the following: (1) variations in orifice size and spacing can have a significant effect on the temperature profiles; (2) similar distributions can be obtained, independent of orifice diameter, if momentum-flux ratio and orifice spacing are coupled; (3) a first-order approximation of the mixing of jets with a variable-temperature main stream can be obtained by superimposing the main-stream and jets-in-an-isothermal-crossflow profiles; (4) the penetration of jets issuing from slanted slots is similar to that of jets from circular holes, but the mixing is slower and is asymmetric with respect to the jet centerplanes, which shift laterally with increasing downstream distance, (5) double rows of jets give temperature distributions similar to those from a single row of equally spaced, equal-area circular holes; (6) for opposed rows of jets, with the orifice centerlines in line, the optimum ratio of orifice spacing to duct height is one-half the optimum value for single-side injection at the same momentum-flux ratio; and (7) for opposed rows of jets, with the orifice centerlines staggered, the optimum ratio of orifice spacing to duct height is twice the optimum value for single-side injection at the same momentum-flux ratio.

In illustrating these results, the mean temperature measurements are compared with profiles calculated using an empirical model based on assumed vertical profile similarity and superposition and with distributions calculated using a three-dimensional elliptic code that had a standard $k-\varepsilon$ turbulence model. The empirical model predictions are very good within the range of the generating experiments, and the numerical model results, although they exhibit too little mixing, correctly describe the effects of the principal flow and geometric variables.

SYMBOLS

A_j/A_m jet to main-stream area ratio, $A_j/A_m = (\pi/4)/[(S/H_0)(H_0/D)^2]$

for one-side injection and $(\pi/2)/[(S/H_0)(H_0/D)^2]$ for two-side

injection

C $(S/H_0)\sqrt{J}$, eq. (3)

C_d orifice discharge coefficient

D orifice diameter

D_j	$D\sqrt{C_d}$
DR	jet to main-stream density ratio, $DR \cong T_m/T_j$
H_0	duct height
J	jet to main-stream momentum-flux ratio, $J = (DR)R^2$
M	jet to main-stream mass-flux ratio, $M = (DR)R$
R	jet to main-stream velocity ratio, $R = V_j/U_m$
S	spacing between orifice centers
S_x	spacing between orifice rows
T	temperature
T_j	jet exit temperature
T_m	main-stream temperature
U	velocity
U_m	main-stream velocity
V_j	jet velocity
$W_{1/2}^{+-}$	jet half-widths above (+) or below (-) the centerline (ref. 5)
w_j/w_T	jet to total mass-flow ratio, $w_j/w_T = \sqrt{(DR)J}\,(C_d)\,(A_j/A_m)/\left(1 + \sqrt{(DR)J}\,(C_d)(A_j/A_m)\right)$
x	downstream coordinate (x = 0 at injection plane)
y	cross-stream (radial) coordinate (y = 0 at wall; y = y_c at location of minimum temperature in a line x = constant and z = constant)
z	lateral (circumferential) coordinate (z = 0 at centerplane)
θ	$(T_m - T)/(T_m - T_j)$, eq. (1)
θ_c	temperature difference ratio at y_c
θ_{min}^{+-}	minimum temperature difference ratio above (+) or below (-) the centerline, (fig. 4)

INTRODUCTION

The problem of jets in crossflow has been rather extensively treated in the literature, to the point that it can almost be called a classical three-dimensional flow problem. Although these studies have all contributed to the understanding of the general problem, the information obtained in any given

study is naturally determined by the motivating application and therefore may not satisfy the specific needs of diverse applications.

Consideration of dilution zone mixing in gas-turbine combustion chambers has motivated several previous studies of the mixing characteristics of jets injected normally into a ducted crossflow (refs. 1 to 12). One factor making the combustor dilution zone jet-in-crossflow application unique is that it is a confined mixing problem - 10 to 50 percent of the total flow enters through the dilution jets. The result is that the equilibrium temperature of the exiting flow may differ significantly from that of the entering main-stream flow. To control or tailor the combustor exit temperature pattern, we must be able to characterize the exit distribution in terms of the upstream flow and geometric variables. This requires that the entire flow field be either known or modeled.

Empirical correlation of experimental data can provide an excellent predictive capability within the parameter range of the generating experiments (e.g., refs. 4 to 6), but empirical models must be used with caution, or not at all, outside this range. Physical modeling, in various levels of sophistication and complexity, may be used to obviate this weakness. In this regard, several one- and two-dimensional, integral and differential jet-in-crossflow models have been developed and shown to give, for example, trajectory predictions that are in good agreement with experiments. These models may provide insight into the dominant physical mechanism(s) and may predict some of the characteristic parameters well, but they rarely provide sufficient information to quantify the flow field in three coordinate directions.

Recently, rapid advances have been made in the capability of computational fluid dynamics models and in their application to complex flows such as jets in crossflow (refs. 13 to 16). These models are, however, still in the development and verification stage. They have been shown to be capable of predicting trends in complex flows, but their capability to provide accurate, quantitive, and grid-independent calculations of these flows has not yet been demonstrated (refs. 14 to 16).

PREVIOUS RESULTS AND THE CURRENT STUDY

The study in references 17 to 19 was performed to extend the available experimental data on, and the empirical correlations of, the thermal mixing of multiple jets in crossflows so that they would include geometric and flow variations characteristic of gas turbine combustion chambers - namely, variable temperature main stream, flow area convergence, noncircular orifices, and double and opposed rows of jets. These experiments are a direct extension of those in reference 1. The effect on the dimensionless temperature distributions of varying the jet to main-stream density ratio, the momentum-flux ratio, and the orifice size and spacing are presented in reference 2.

From the data in reference 1, an empirical model was developed (refs. 4 and 5) for predicting the temperature field downstream of a row of jets mixing with a confined crossflow. The effects of separately varying the independent flow and geometric variables and the relations among these variables which optimize the mixing are reviewed in reference 12. This study was conducted using an interactive microcomputer program that is based on the empirical model of reference 5.

The results of these investigations may be summarized as follows: (1) mixing improves with increasing downstream distance; (2) the momentum-flux ratio is the most significant flow variable; (3) the effect of density ratio is small at constant momentum-flux ratio; (4) at any given momentum-flux ratio, decreasing orifice spacing while maintaining a constant orifice diameter reduces penetration and increases lateral uniformity; (5) increasing orifice diameter while maintaining a constant spacing-to-diameter ratio improves penetration but increases lateral nonuniformity; (6) increasing orifice diameter at a constant orifice spacing increases the magnitude of the temperature difference, but jet penetration and profile shape remain similar; (7) profiles for conditions with equivalent coupling of orifice spacing and momentum-flux ratio show similar distributions; and (8) smaller momentum-flux ratios (larger spacing) require a greater downstream distance for equivalent mixing.

Results from the experiments in references 17 to 19 that are considered in this paper include the effects of variations in orifice size and spacing, coupled spacing and momentum-flux ratio, variable temperature main stream, noncircular orifices, and double and opposed rows of inline and staggered jets. Also, temperature field measurements from several experiments are compared with distributions calculated using an empirical model based on assumed vertical profile similarity and superposition (refs. 17 to 19) and using a three-dimensional elliptic code with a standard k-ε turbulence model (ref. 14). The results show the capability of these models to predict the effects of the principal flow and geometric variables.

A more complete presentation of the experimental results and a discussion of the empirical modeling performed in this study are given in references 1, 4, and 17 to 19. Selected experimental and analytical results from these studies and from reference 14 are also given in references 2, 5, and 20 to 23.

FLOW FIELD DESCRIPTION

Figure 1 shows a schematic of the dilution jet flow field for jet injection from the top wall. The temperature field results are presented in three-dimensional oblique views of the temperature difference ratio θ:

$$\theta = \frac{T_m - T}{T_m - T_j} \tag{1}$$

A sequence of experimental profiles of this parameter at several locations downstream of the injection plane is shown in figure 2. In the three-dimensional plots the temperature distribution is shown in the y,z-planes normal to the main flow direction x. The coordinates y and z are, respectively, normal and parallel to the orifice row. Note that the jet fluid is identified by the larger values of the θ parameter (i.e., $\theta = 1$ if $T = T_j$, and $\theta = 0$ if $T = T_m$). The equilibrium θ for any configuration is equal to the fraction of the total flow entering through the dilution jets w_j/w_T.

The orifice configurations investigated are shown in figure 3. The primary independent geometric variables for each orifice configuration are the spacing between adjacent orifices S, the orifice diameter D (for noncircular orifices, this is taken as the diameter of a circle of equal area), and, for double rows, the axial spacing between rows S_x. These are expressed in

dimensionless form as the ratio of the orifice spacing to duct height S/H_0, the ratio of the duct height to orifice diameter H_0/D, and the ratio of the axial spacing to the duct height S_x/H_0.

EXPERIMENTAL CONSIDERATIONS

The dilution-jet mixing characteristics were determined by measuring temperature and pressure distributions with a vertical-rake probe positioned at different axial and lateral stations. This probe had 20 thermocouple elements. A 20-element total-pressure rake and a 20-element static-pressure rake were located nominally 5 mm ($0.05 H_0$) on each side of the thermocouple rake. The center-to-center spacing between sensors on each rake was $0.05 H_0$.

This probe traversed a matrix of 48 to 64 z,x-plane survey locations. The flow field was mapped in the z-direction over a distance of 1 or 1.5 times the hole spacing S at intervals of $S/10$. For most tests, the x,y-plane containing the orifice centerline (centerplane) was at the center of the span surveyed; that is, data surveys were from midplane to midplane.

Measurements in the x-direction were made at up to five planes with $0.25 < X/H_0 < 2$. Because the objective in this application is to identify dilution-zone configurations that will provide a desired mixing pattern within a given combustor length, the downstream stations are defined in intervals of the duct height H_0 rather than intervals of the orifice diameter D.

FLOW FIELD MODELS

Empirical

The empirical model for the temperature field downstream of jets mixing with a confined crossflow is based on the observation that properly nondimensionalized vertical temperature profiles can be expressed in the following self-similar form (ref. 5) for any location in the flow field:

$$\frac{\theta - \theta_{min}^+}{\theta_c - \theta_{min}^+} = \exp\left[- \ln 2 \ \frac{(y - y_c)^2}{w_{1/2}^+} \right] \tag{2}$$

where θ is the temperature difference ratio at vertical location y, and θ_{min}^+, θ_{min}^-, $w_{1/2}^+$, $w_{1/2}^-$, θ_c, and y_c are scaling parameters as shown in figure 4. Correlations have been developed for each of these in terms of the independent variables J, S/D, H_0/D, Z/S, and x/H_0. The correlations in reference 5 for a single row of jets in a uniform temperature crossflow have been extended for predicting the temperature field downstream of single, double, or opposed rows of jets, either inline or staggered, injected into an isothermal or nonisothermal main stream, with or without flow-area convergence (refs. 17 to 19).

153

Numerical

The numerical code used in this investigation is based on the USARTL three-dimensional, fully elliptic, turbulent flow model (ref. 24) and uses pressure and velocity as the main hydrodynamic variables. This code, or similar versions thereof, has been used in previous validation and assessment studies (refs. 14 to 16).

The governing equations are represented by finite-difference approximations on a staggered grid system. The differencing technique employed is hybrid for convective terms with central differencing of all other terms. The velocity-pressure coupling is handled by the SIMPLE algorithm of Patankar and Spalding (refs. 25 and 26). Uniform velocities and mass flow rates were used at all inflow boundaries. The code contained a conventional $k-\varepsilon$ turbulence model, and standard values of the constants C_D, C_1, and C_2 were used (i.e., $C_D = 0.09$, $C_1 = 1.44$, $C_2 = 1.92$). The rms turbulence intensity was chosen to be 4.5 percent of the local mean velocity, the inlet length scale was 2 percent of the jet diameter and duct height for the jet and main stream, respectively, and the turbulent Prandtl number was 0.9 for all calculations.

RESULTS AND DISCUSSION

The following paragraphs describe the experimental results and compare them with those of the empirical and numerical model calculations, and illustrate the effects of the primary independent variables. The flow and geometry conditions corresponding to the figures shown are given in table I.

Orifice Size and Spacing

At constant orifice area, changes in orifice size and spacing can have a significant influence on the θ profiles. This is shown by the experimental profiles in figure 5 where jets from closely spaced small orifices underpenetrate and remain near the injection wall (fig. 5(a)), and jets from widely spaced larger orifices overpenetrate and impinge on the opposite wall (fig. 5(b)). In this figure, and in several others in which the orifice spacing is different for different parts of the figure, a duct cross-section is included to indicate the region for which data are shown.

The data for these conditions, at $x/H_0 = 0.5$, are compared with calculated distributions in figure 6. The empirical model reproduces the data very well in the small orifice case because the data are consistent with the major assumption in the empirical model, namely that all vertical temperature distributions can be reduced to similar Gaussian profiles. The empirical model does not do as well in the larger orifice case, however, because the impingement of the jets on the opposite wall results in vertical profiles which are not similar.

The numerical model calculations were made with approximately 20 000 nodes. Although these are in qualitative agreement with the data, they show temperature gradients that are too steep, especially in the transverse direction. Underprediction of the mixing was also seen in the single-jet calculations of reference 13 where it is shown that the $k-\varepsilon$ type of turbulence model

underestimates the intensity. The result in figure 6 is typical of the numerical model calculations shown in this paper.

For the small-orifice case a coarse-grid calculation using less than 6000 nodes was also performed. This calculation is shown on the right side of figure 6(a) and illustrates the significant influence that grid selection can have on the solution obtained, and the smearing of the profiles which can occur as a result of numerical diffusion.

Coupled Spacing and Momentum-Flux Ratio

Examination of the experimental data revealed that similar jet penetration is obtained, independent of orifice diameter, if orifice spacing and momentum-flux ratio are coupled (refs. 2, 5, 12, and 22). For example, low momentum-flux ratios require large, widely spaced holes, whereas smaller, closely spaced holes are appropriate for high-momentum flux ratios, as shown in figure 7. The duct cross section is shown to the right of the three-dimensional oblique and isotherm contour plots for each configuration. It follows that for low momentum-flux ratios (large spacing) a greater axial distance is required for equivalent mixing.

In general, jet penetration and centerplane profiles are similar when the orifice spacing and the square root of the momentum-flux ratio are inversely proportional; that is,

$$C = (S/H_0) \sqrt{J} \tag{3}$$

For single-side injection, the centerplane profiles are approximately centered across the duct height and approach an isothermal distribution in the minimum downstream distance when $C = 2.5$. This appears to be independent of orifice diameter, as shown in both the calculated and experimental profiles in figure 8. In equation (3), values of C that are a factor of 2 or more smaller or larger than the optimum values correspond to underpenetration or overpenetration, respectively. (Figs. 5 and 6 and table I). A summary of the spacing and momentum-flux ratio relationships for single-side injection is given in table II.

Variable Temperature Main Stream

The influence of a nonisothermal main-stream flow on measured profiles for intermediate momentum-flux ratios with $S/H_0 = 0.5$ and $H_0/D = 4$ is shown in figure 9. The corresponding isothermal main-stream case is shown in the top row. In the center row of the figure, the upstream profile (left frame) is coldest near the injection wall, whereas in the bottom row, the upstream profile (left frame) is coldest near the opposite wall. For the definition of θ in this figure, T_m is the hottest temperature in the main stream for each case.

Experimental, empirical, and numerical results for the top-cold case are shown in figure 10. The empirical calculations are from a superposition of the upstream profile and the corresponding jets-in-an-isothermal-main-stream distribution (ref. 22). Although this gives a good first-order approximation, it should be noted that with a variable temperature main stream there can be

155

cross-stream thermal transport due to the flow of main-stream fluid around the jets (and hence, to different y locations), and this is not accounted for when the distributions are superimposed. This becomes apparent if the local main-stream temperature $T_m(y)$, is used in the definition of θ in equation (1).

In the variable temperature main-stream case, the numerical model results agree well with the experimental data, especially on the jet centerplane, but the transverse mixing is underpredicted, as in the corresponding isothermal main-stream case shown in figure 8(b).

Slanted Slots

Figure 11 shows experimental and calculated three-dimensional oblique θ distributions for slanted slots at intermediate momentum-flux ratios. These slots had an aspect ratio (length/width) of 2.8, with their major axes slanted at 45° to the main-stream flow direction. The orifice spacing and size are $S/H_0 = 0.5$ and $H_0/D = 4$, respectively. The temperature distributions in this figure may be compared with those for equivalent-area circular holes in figure 8(b). As noted in reference 23, the penetration and mixing of jets from the slanted slots are noticeably less than those of jets from the circular holes. The normally symmetric vortex pair is asymmetric in this case, as is apparent in the experimental profiles in figure 11 (and in the figures in ref. 23). These profiles also show that the centerplanes of the jets shift laterally with increasing downstream distance.

The empirical model calculations include a modification to account for the observed centerplane shift, but they do not model the asymmetry (refs. 19 and 23). The numerical calculations for this case exhibit both the centerplane shift and the asymmetry, and they are good in the context of the qualitative agreement seen throughout the comparisons given in this paper.

Double Rows of Holes

Figure 12 shows experimental and calculated temperature distributions for an orifice plate with two inline rows of jets ($S_x/H_0 = 0.5$) from circular orifices. It was observed from the experimental profiles in reference 23 that the two configurations have very similar temperature distributions, and this is seen in the calculated profiles as well. In this case the empirical model calculations are derived by superimposing the distributions from the two rows.

Both experimental and calculated temperature distributions are shown in figure 13 for a double-row configuration when $S_x/H_0 = 0.25$ and the trailing row has twice as many orifices as the lead row. Note that the orifice area is the same for both rows. These profiles show the dominance of the lead row in establishing the jet penetration and first-order profile shape (ref. 23). As with the double row of inline holes, the empirical calculations for this case were obtained by superimposing separate calculations for the two rows.

Opposing Rows of Jets

The remainder of this paper presents results for two-side injection from opposing rows of jets with (1) the top and bottom jet centerlines directly opposite each other and (2) the top and bottom jet centerlines staggered in the z direction. The experimental results are shown and compared with the single-side results in figures 14 and 16. In these figures, a duct cross section, drawn to scale, is to the left of the data.

Opposed Rows of Inline Jets

Figure 14 shows a comparison at intermediate momentum-flux ratios for single-side and opposed-jet injection. For these momentum-flux ratios, an appropriate orifice-spacing-to-duct-height ratio for optimum single-side mixing is approximately 0.5 (see eq.(2)), as confirmed by the profiles in figure 7.

For opposed-jet injection, with equal momentum-flux ratios on both sides, the effective mixing height is half the duct height because, as reference 3 shows, the effect of an opposite wall is similar to that of the plane of symmetry in an opposed-jet configuration. Thus, the appropriate orifice-spacing-to-duct-height ratio for opposed-jet injection at these intermediate momentum-flux ratios would be about $S/H_0 = 0.25$. Dimensionless temperature distributions downstream of jets with this spacing are shown in the bottom row of figure 14, and the two streams do indeed mix very rapidly. Note that since the orifices in figures 14(a) and (b) are the same size, the jet to main-stream flow ratio is four times greater for opposed-jet injection than for single-side injection. If it is desired to maintain an equal flow rate, the orifice diameter must be halved, since there is injection from both sides and opposed-jet injection requires twice as many holes in the row as optimum single-side injection.

Figure 15 shows experimental and calculated profiles for opposed rows of jets with identical orifice spacing and diameter and with the orifice centerlines in line. The empirical model predicts opposed-jet injection very well, as the experimental profiles on both sides of the plane of symmetry support the Gaussian profile assumption. The penetration and profile shape calculated with the numerical model are in good agreement with the data, but the mixing is otherwise underpredicted, as evidenced by the steep transverse and lateral gradients seen in almost all the previous calculations also.

Opposed Rows of Staggered Jets

Figure 16 shows comparisons of single-side and staggered jet injection for intermediate momentum-flux ratios. Since the effective mixing height for opposed inline injection was half the duct height, it was assumed that the effective orifice spacing for staggered jets would be half the actual spacing. Thus, to maintain an optimum coupling of the effective spacing and the momentum-flux ratio, the orifice spacing for opposed staggered configurations should be double that which is appropriate for single-side injection.

This hypothesis is verified by the rapid mixing of the two streams in the bottom row of profiles in figure 16. This figure shows clearly that a config-

uration which mixes well with one-side injection performs even better when every other orifice is moved to the opposite wall.

Empirical and numerical model calculations for an opposed row of staggered jets are compared with the data in figure 17. The empirical model does not handle this complex case well, as the fluid dynamic interactions here are not amenable to a direct extension of the simple Gaussian profile and superposition type of modeling appropriate for most of the single-side and opposed-jet cases of interest. The numerical model calculations are not in appreciably better agreement with the data than are the empirical model results, however, because the mixing is underpredicted here as in the previous cases.

A summary of the spacing and momentum-flux ratio relationships which give optimum mixing for opposed rows of inline and staggered jets is given in table II.

LIMITATIONS AND APPLICABILITY

Empirical

The empirical model results presented here show that correlating experimental data can provide an excellent predictive capability within the parameter range of the generating experiments, provided the experimental results are consistent with the assumptions made in the empirical model. These models must, however, be used with caution, or not at all, outside this range.

The ranges of the experimental variables on which this empirical model was based are given in table III. The density ratio, momentum-flux ratio, orifice spacing, and orifice size were the primary independent variables. This table also gives ratios that are derived from the primary variables: the orifice to main-stream area ratio, the jet-to-total mass flow split, and the parameter coupling the spacing and momentum-flux ratio. Not all combinations of the primary variables in the table were tested; only those combinations which are within the range given for the derived variables represent conditions that are within the range of the experiments.

Examining the results in figures 5 to 17 in the context of equation (3) suggests that, in general, the empirical model provides good temperature field predictions for single-side injection when $1 < C < 5$. Similarly, good predictions are obtained for opposed inline jets provided that $0.5 < C < 2.5$. This model does not work well for impinging flows because the experimental temperature distributions are not consistent with the assumption of Gaussian profile similarity in the empirical model. The experimental profiles for conditions giving optimum mixing in opposed staggered-jet configurations are also somewhat at variance with the model assumptions; in these cases, satisfactory agreement with the data must be considered fortuitous.

A major weakness of the empirical model used here in (refs. 17 to 19) and in previous versions (refs. 4 and 5) is that the form of the correlations precludes their use for semi-confined flows (large H_0/D or S/D), single-jet flows, or flows in which it is known a priori that the primary assumptions in the model will be invalid.

Numerical

The numerical model is not subject to the inherent limitation of the empirical model regarding profile shape and confinement. Thus, three-dimensional codes can provide calculations for complex flows for which the assumptions in the empirical model are known to be invalid or outside the range of available experiments. Furthermore, numerical models provide calculations for all flow field parameters of interest, not just those that happen to have been empirically correlated.

The numerical calculations correctly show the trends which result from variation of the independent flow and geometric variables, although the results consistently exhibit too little mixing. The numerical model calculations for the slanted slots and staggered jet cases are encouraging because the experimental data for these cases show profiles that are not consistent with the primary assumptions in the empirical model.

The numerical calculations performed are shown to be grid sensitive, and false diffusion is known to be present. Uncertainties also exist in these calculations regarding the validity of turbulence model assumptions and due to unmeasured (and hence assumed) boundary conditions. The results shown here are not intended to represent the best agreement possible from numerical models at this time. Better temperature field agreement could undoubtedly have been achieved by adjusting model constants and/or inlet boundary conditions. But, since this was not necessary to satisfy the present objective of evaluating the potential of these codes vis-a-vis combustor dilution zone flow fields, and because the mean temperature was the only parameter compared, no adjustments were made.

Thus, as with previous assessments in references 14 to 16, three-dimensional calculations, such as those in this paper, should be considered as only qualitatively accurate at this time, and three-dimensional codes of this type are useful primarily in guiding design changes or in perturbation analyses. The three-dimensional code used herein, although sufficiently promising to justify further development and assessment, is not a practical tool for general engineering use in its present form. Codes with improved numerics, accuracy, and turbulence models should provide more quantitative predictions.

CONCLUSIONS

The principal conclusions from the experimental results reviewed herein are as follows:

1. Variations of momentum-flux ratio and of orifice size and spacing have a significant effect on the flow distribution.

2. Similar distributions can be obtained, independent of orifice diameter, when momentum-flux ratio and orifice spacing are coupled.

3. A first-order approximation of the mixing of jets with a variable-temperature main stream can be achieved by superimposing the jets-in-an-isothermal-main-stream and upstream profiles.

4. The penetration and mixing of jets issuing from 45° slanted slots are less than those from equivalent-area circular holes.

5. With the same orifice spacing in (at least) the lead row, double rows of jets have temperature distributions similar to those from a single row of equally spaced, equivalent-area circular orifices.

6. For opposed rows of jets, with the orifice centerlines in line, the optimum ratio of orifice spacing to duct height is one-half the optimum value for single-side injection at the same momentum-flux ratio.

7. For opposed rows of jets with the orifice centerlines staggered, the optimum ratio of orifice spacing to duct height is twice the optimum value for single-side injection at the same momentum-flux ratio.

Temperature field measurements from the experiments cited previously are compared with distributions calculated using an empirical model based on assumed vertical profile similarity and superposition and with calculations made using a three-dimensional elliptic code with a standard k-ε turbulence model. The results can be summarized as follows:

Empirical model calculations provide very good results for modeled parameters within the range of experiments whenever the primary assumptions in the model are satisfied.

Three-dimensional code calculations made in this study correctly approximate the trends which result from varying the independent flow and geometric variables, but they consistently exhibit too little mixing. (The advantage of these models is that they can predict all flow field quantities, flows outside the range of experiments, or flows where empirical assumptions are invalid.) Numerical calculations should yield more quantitative predictions with improvements in numerics, accuracy, and turbulence models.

REFERENCES

1. Walker, R.E.; and Kors, D.L.: Multiple Jet Study. NASA CR-121217, 1973.

2. Holdeman, J.D.; Walker, R.E.; and Kors, D.L.: Mixing of Multiple Dilution Jets with a Hot Primary Airstream for Gas Turbine Combustors. AIAA Paper 73-1249, Nov. 1973.

3. Kamotani, Y.; and Greber, I.: Experiments on Confined Turbulent Jets in Cross Flow. NASA CR-2392, 1974.

4. Walker, R.E.; and Eberhardt, R.G.: Multiple Jet Study Data Correlations. NASA CR-134795, 1975.

5. Holdeman, J.D.; and Walker, R.E.,: Mixing of a Row of Jets with a Confined Crossflow. AIAA J., vol. 15, no. 2, Feb. 1977, pp. 243-249.

6. Cox, G.B. Jr.: Multiple Jet Correlations for Gas Turbine Engine Combustor Design. J. Eng. Power, vol. 98, no. 2, Apr. 1976, pp. 265-273.

7. Cox, G.B. Jr.: An Analytical Model for Predicting Exit Temperature Profile from Gas Turbine Engine Annular Combustors. AIAA Paper 75-1307, Sept. 1975.

8. Riddlebaugh, S.M.; Lipshitz, A.; and Greber, I.: Dilution Jet Behavior in the Turn Section of a Reverse-Flow Combustor. AIAA Paper 82-0192, Jan. 1982.

9. Khan, Z.A.; McGuirk, J.J.; and Whitelaw, J.H.: A Row of Jets in a Crossflow. Fluid Dynamics of Jets with Application to V/STOL, AGARD-CP-308, Technical Editing and Reproduction, London, 1982, pp. 10-1 to 10-11.

10. Atkinson, K.N.; Khan, Z.A.; and Whitelaw, J.H.: Experimental Investigation of Opposed Jets Discharging Normally into a Cross-Stream. J. Fluid Mech., vol. 115, Feb. 1982, pp. 493-504.

11. Wittig, S.L.K.; Elbahar, O.M.F.; and Noll, B.E.: Temperature Profile Development in Turbulent Mixing of Coolant Jets with a Confined Hot Cross Flow. J. Engr. Gas Turbines Power, vol. 106, no. 1, Jan. 1984, pp. 193-197.

12. Holdeman, J.D.: Perspectives on the Mixing of a Row of Jets with a Confined Crossflow. AIAA Paper 83-1200, June 1983.

13. Claus, R.W.: Calculation of a Single Jet in Crossflow and Comparison with Experiment. AIAA Paper 83-0238, Jan. 1983.

14. Srinivasan, R., et al: Aerothermal Modeling Program: Phase I. (Garrett 21-4742, Garrett Turbine Engine Co.; NASA Contract NAS3-23523) NASA CR-168243, 1983.

15. Kenworthy, M.J.; Correa, S.M.; and Burrus, D.L.: Aerothermal Modeling, Phase I. NASA CR-168296, 1983.

16. Sturgess, G.J.: Aerothermal Modeling Program, Phase I. (PWA-5907-19, Pratt and Whitney Aircraft; NASA Contract NAS3-23524) NASA CR-168202, 1983.

17. Srinivasan, R.; Berenfeld, A.; and Mongia, H.C.: Dilution Jet Mixing Phase I. (Garrett-21-4302, Garrett Turbine Engine Co.; NASA Contract NAS3-22110) NASA CR-168031, 1982.

18. Srinivasan, R.; Coleman, E.; and Johnson, K.: Dilution Jet Mixing Program, Phase II. (Garrett 21-4804, Garrett Turbine Engine Co.; NASA Contract NAS3-22110) NASA CR-174624, 1984.

19. Srinivasan, R., et al: Dilution Jet Mixing, Phase III. (Garrett 21-5418, Garrett Turbine Engine Co.; NASA Contract NAS3-22110). NASA CR-174884, 1985.

20. Holdeman, J.D.; and Srinivasan, R.: Modeling of Dilution Jet Flowfields. Combustion Fundamentals Research, NASA CP-2309, 1984, pp. 175-187.

21. Holdeman, J.D.; and Srinivasan, R.: On Modeling Dilution Jet Flowfields. AIAA Paper 84-1379, June 1984.

22. Holdeman, J.D.; Srinivasan, R.; and Berenfeld, A.: Experiments in Dilution Jet Mixing. AIAA J., vol. 22, no. 10, Oct. 1984, pp. 1436-1443.

23. Holdeman, J.D., et al: Experiments in Dilution Jet Mixing - Effects of Multiple Rows and Non-circular Orifices. AIAA Paper 85-1104, July 1985.

24. Bruce, T.W.; Mongia, H.C.; and Reynolds, R.S.: Combustor Design Criteria Validation. AiResearch Manufacturing Co., AIRESEARCH-75-211682(38)-1,-2, and -3, 1979 (USARTL-TR-78-55A, B, and C) (AD-A067657, AD-A067689, AD-A066793).

25. Patankar, S.V.; and Spalding, D.B.: A Calculation Procedure for Heat, Mass and Momentum Transfer in Three-Dimensional Parabolic Flows. Int. J. Heat Mass Trans., vol. 15, no. 10, Oct. 1972, pp. 1787-1806.

26. Patankar, S.Y.; and Spalding, D.B.: A Computer Model for Three-Dimensional Flow in Furnaces. 14th Symposium (International) on Combustion, The Combustion Institute, Pittsburgh, 1973, pp. 605-614.

TABLE I. - FLOW AND GEOMETRY CONDITIONS

Figure	S/H_0	H_0/D	A_j/A_m	C_d	DR	$\sqrt{J}$	w_j/w_T	C^a
2	0.5	4	0.10	0.76	2.2	26.2	0.36	2.56
5(a), 6(a)	.25	8	.05	.60	2.1	22.4	.17	1.18
5(b), 6(b)	1.0	4	.05	.67	2.2	23.5	.19	4.85
7(a)	1.0	4	.05	.73	2.1	5.3	.11	2.30
7(b), 14(a)	.5	8	.025	.61	2.2	28.4	.11	2.66
7(c)	.25	8	.05	.61	2.3	92.7	.30	2.60
8(a)	.5	5.7	.05	.71	2.2	25.4	.21	2.52
8(b), 9(a), 16(a)	.5	4	.10	.61	2.1	18.6	.27	2.16
b9(b), 10	.5	4	.10	.61	1.8	31.3	.31	2.80
c9(c)	.5	4	.10	.68	2.2	24.4	.31	2.47
d11	.5	4	.10	.66	2.2	27.1	.33	2.60
12	.5	5.7	.05	.65	2.2	26.3	.33	2.56
	.5	5.7	.05	.66	2.2	26.9	----	2.59
13	.5	5.7	.05	.69	2.2	26.8	.34	2.59
	.25	8	.05	.70	2.2	26.6	----	1.29
14(b), 15	.25	8	.10	.65	2.1	25.0	.32	1.25
16(b), 17	1.0	4	.10	.65	2.1	27.6	.33	5.25

$^aC = (S/H_0)\sqrt{J}$.
^{b}Top cold.
^{c}Top hot.
^{d}45° slanted slots.

TABLE II. – SPACING AND MOMENTUM-FLUX RATIO

RELATIONS

Configuration	$C = (S/H_0) \sqrt{(J)}$
Single-side injection Underpenetration Optimum Overpenetration	<1.25 2.5 >5
Opposed rows of jets Inline optimum Staggered optimum	1.25 5

TABLE III. – RANGE OF INDEPENDENT FLOW

AND GEOMETRIC VARIABLES INVESTI-

GATED IN REFERENCES 17 TO 19

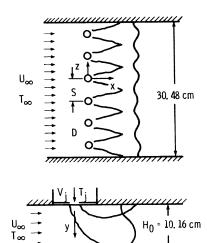|	
DR	0.5 to 2.5
J	5 to 105
S/H_0	0.125 to 1
H_0/D	4 to 16
A_j/A_m	0.025 to 0.1
w_j/w_T	0.075 to 0.33
$C = (S/H_0) \sqrt{J}$	0.5 to 10

Figure 1. - Schematic of multiple jet flow.
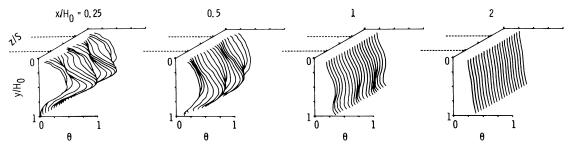
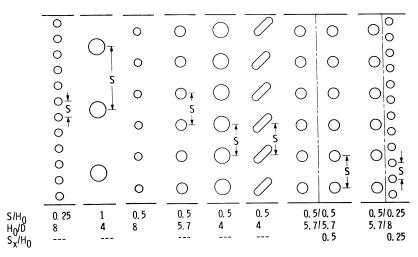Figure 2. - Experimental mean temperature distributions (J = 26.2, S/H_0 = 0.5, H_0/D = 4).

S/H$_0$	0.25	1	0.5	0.5	0.5	0.5	0.5/0.5	0.5/0.25
H$_0$/D	8	4	8	5.7	4	4	5.7/5.7	5.7/8
S$_x$/H$_0$	---	---	---	---	---	---	0.5	0.25

Figure 3. - Dilution-jet mixing orifice configurations.
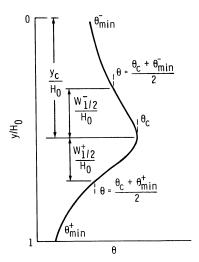
Figure 4. - Schematic of typical vertical temperature profile showing scaling parameters in empirical model.
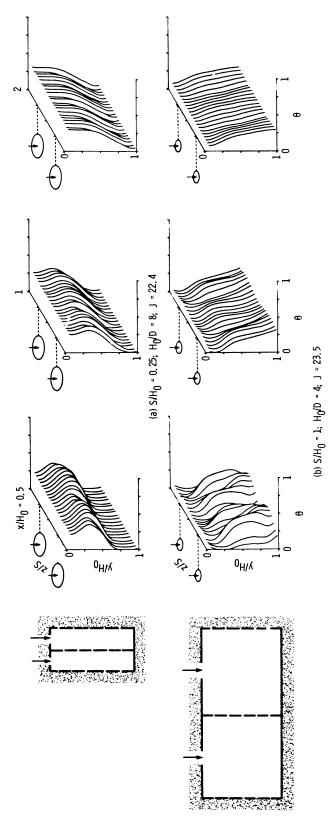
(a) $S/H_0 = 0.25$; $H_0/D = 8$; $J = 22.4$

(b) $S/H_0 = 1$; $H_0/D = 4$; $J = 23.5$

Figure 5. – Effect on temperature distributions of varying orifice spacing at constant area ($A_j/A_m = 0.05$).

166

EXPERIMENTAL   EMPIRICAL   NUMERICAL

(a) $S/H_0 = 0.25$; $H_0/D = 8$; $J = 22 4$.
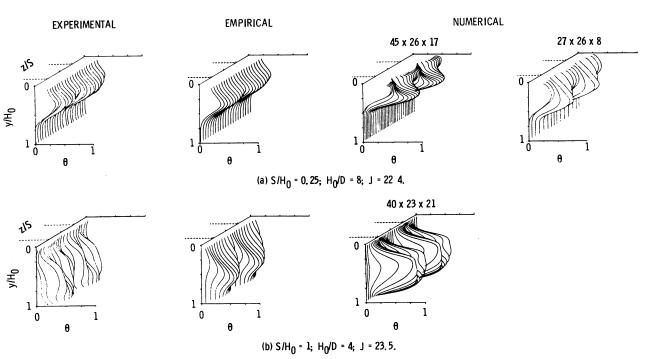
(b) $S/H_0 = 1$; $H_0/D = 4$; $J = 23.5$.

Figure 6. – Effect of varying orifice spacing at constant area on measured and calculated temperature distributions when $x/H_0 = 0.5$ ($A_j/A_m = 0.05$).
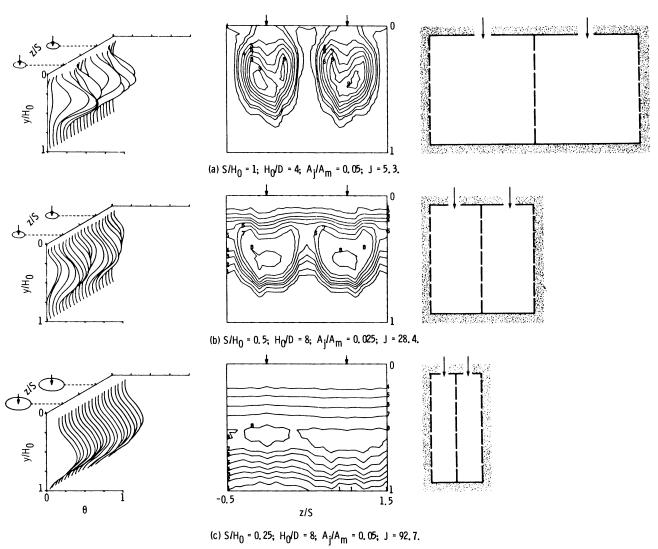
167

(a) $S/H_0 = 1$; $H_0/D = 4$; $A_j/A_m = 0.05$; $J = 5.3$.

(b) $S/H_0 = 0.5$; $H_0/D = 8$; $A_j/A_m = 0.025$; $J = 28.4$.

(c) $S/H_0 = 0.25$; $H_0/D = 8$; $A_j/A_m = 0.05$; $J = 92.7$.

Figure 7. - Oblique profile plots and isotherm contours when $x/H_0 = 0.5$ for coupled orifice spacing and momentum-flux ratio.

168

(a) $H_0/D = 5.7$; $A_j/A_m = 0.05$; $J = 25.5$.

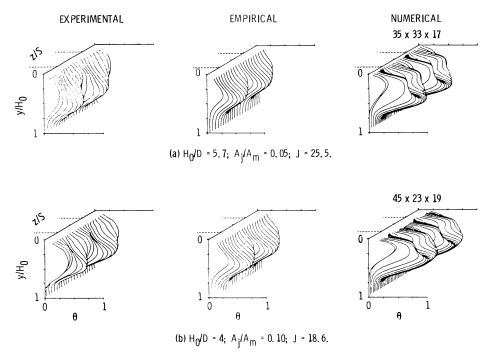45 x 23 x 19

(b) $H_0/D = 4$; $A_j/A_m = 0.10$; $J = 18.6$.

Figure 8. – Effect of varying orifice diameter at constant spacing on measured and calculated temperature distributions when $x/H_0 = 0.5$ ($S/H_0 = 0.5$).
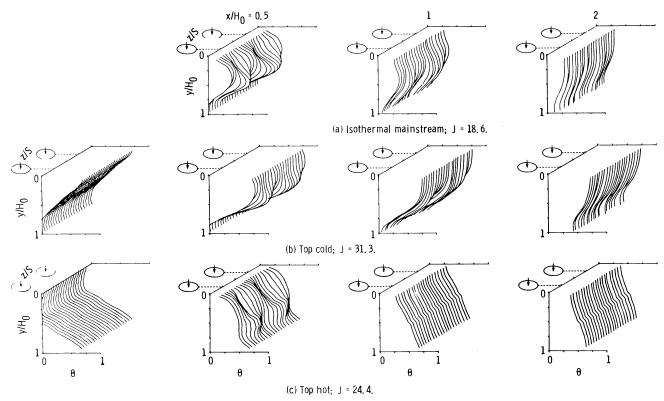

(a) Isothermal mainstream; $J = 18.6$.

(b) Top cold; $J = 31.3$.

(c) Top hot; $J = 24.4$.

Figure 9. – Influence of nonisothermal mainstream on measured temperature profiles ($S/H_0 = 0.5$; $H_0/D = 4$, $A_j/A_m = 0.10$).

169

EXPERIMENTAL   EMPIRICAL   NUMERICAL
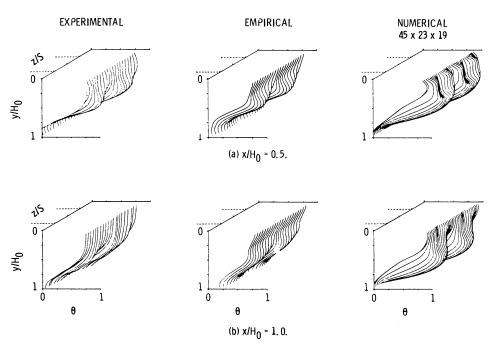45 x 23 x 19

(a) x/H_0 = 0.5.

(b) x/H_0 = 1.0.

Figure 10. - Measured and calculated temperature distribution for jets injected into a nonisothermal mainstream; top cold (S/H_0 = 0.5, H_0/D = 4, J = 31.3).
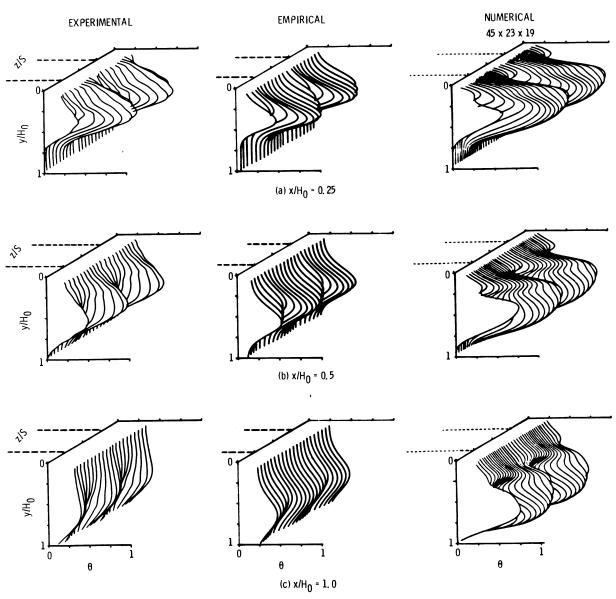
170

EXPERIMENTAL   EMPIRICAL   NUMERICAL
                                         45 x 23 x 19

(a) $x/H_0 = 0.25$

(b) $x/H_0 = 0.5$

(c) $x/H_0 = 1.0$

Figure 11. – Measured and calculated temperature distributions for slanted slots at an intermediate momentum-flux ratio ($S/H_0 = 0.5$, $H_0/D = 4$, $J = 27.1$).

EXPERIMENTAL   EMPIRICAL   NUMERICAL
36 x 29 x 19

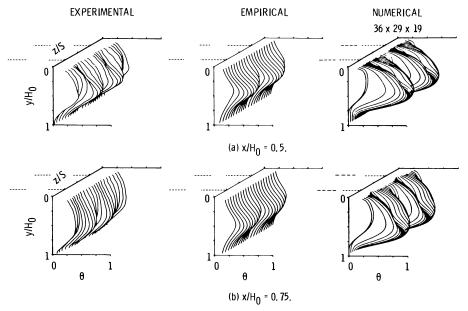
(a) $x/H_0 = 0.5$.

(b) $x/H_0 = 0.75$.

Figure 12. - Measured and calculated temperature distributions for double row of inline jets at an intermediate momentum-flux ratio ($A_j/A_m = 0.10$, $S_x/H_0 = 0.5$. Row 1: $S/H_0 = 0.5$, $H_0/D = 5.7$, $J = 26.3$. Row 2: $S/H_0 = 0.5$, $H_0/D = 5.7$, $J = 26.9$).

EXPERIMENTAL   EMPIRICAL   NUMERICAL
41 x 23 x 21

(a) $x/H_0 = 0.25$.
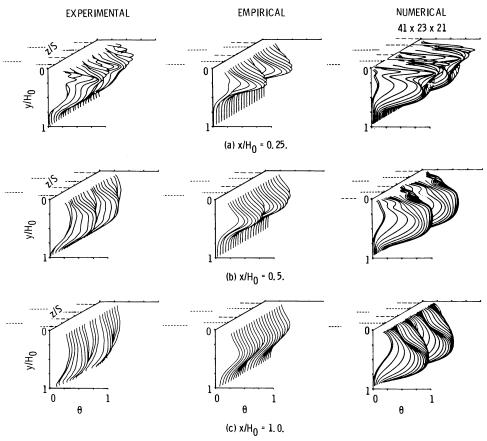

(b) $x/H_0 = 0.5$.

(c) $x/H_0 = 1.0$.

Figure 13. - Measured and calculated temperature distributions for double row of dissimilar jets at an intermediate momentum-flux ratio ($A_j/A_m = 0.10$, $S_x/H_0 = 0.25$. Row 1: $S/H_0 = 0.5$, $H_0/D = 5.7$, $J = 26.8$. Row 2: $S/H_0 = 0.25$, $H_0/D = 8$, $J = 26.6$).
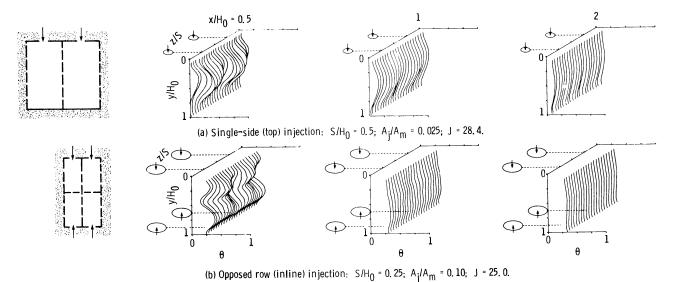
172

(a) Single-side (top) injection: $S/H_0 = 0.5$; $A_j/A_m = 0.025$; $J = 28.4$.

(b) Opposed row (inline) injection: $S/H_0 = 0.25$; $A_j/A_m = 0.10$; $J = 25.0$.

Figure 14. - Comparison between single-side and opposed-jet injection ($H_0/D = 8$).

EXPERIMENTAL

EMPIRICAL
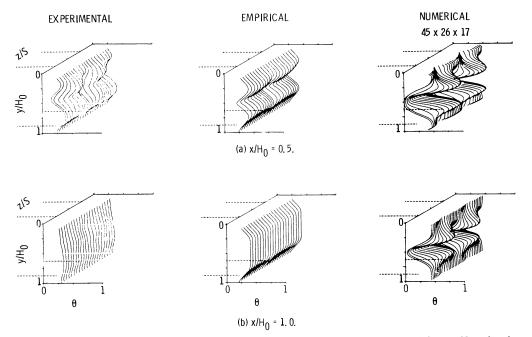
NUMERICAL
45 x 26 x 17

(a) $x/H_0 = 0.5$.

(b) $x/H_0 = 1.0$.

Figure 15. - Measured and calculated temperature distributions for opposed rows of inline jets ($S/H_0 = 0.25$, $H_0/D = 8$, $A_j/A_m = 0.10$, $J = 25$).
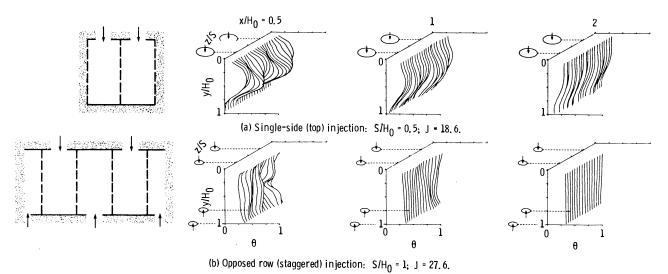
173

(a) Single-side (top) injection: $S/H_0 = 0.5$; $J = 18.6$.

(b) Opposed row (staggered) injection: $S/H_0 = 1$; $J = 27.6$.

Figure 16. - Comparison between single-side and staggered jet injection ($H_0/D = 4$, $A_j/A_m = 0.10$).

EXPERIMENTAL   EMPIRICAL   NUMERICAL
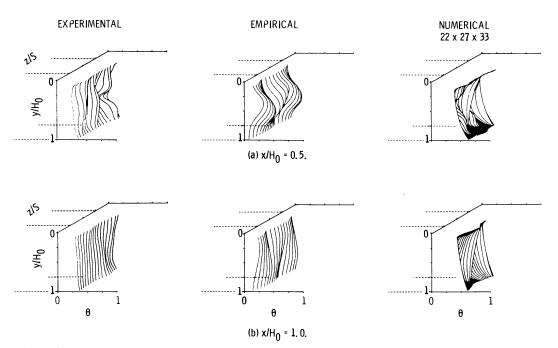22 x 27 x 33

(a) $x/H_0 = 0.5$.

(b) $x/H_0 = 1.0$.

Figure 17. - Measured and calculated temperature distributions for opposed rows of staggered jets ($S/H_0 = 1$, $H_0/D = 4$, $A_j/A_m = 0.10$, $J = 27.6$).

174

THEORETICAL KINETIC COMPUTATIONS IN COMPLEX REACTING SYSTEMS

David A. Bittker
NASA Lewis Research Center
Cleveland, Ohio

This paper describes NASA Lewis' studies of complex reacting systems at high temperature. The changes which occur are the result of many different chemical reactions occurring at the same time. Both an experimental and a theoretical approach are needed to fully understand what happens in these systems. The latter approach is discussed herein. We present the differential equations which describe the chemical and thermodynamic changes, and we describe their solution by numerical techniques using a detailed chemical mechanism. Several different comparisons of computed results with experimental measurements are also given. These include the computation of (1) species concentration profiles in batch and flow reactions, (2) rocket performance in nozzle expansions, and (3) pressure versus time profiles in hydrocarbon ignition processes. The examples illustrate the use of detailed kinetic computations to elucidate a chemical mechanism and to compute practical quantities such as rocket performance, ignition delay times, and ignition lengths in flow processes.

INTRODUCTION

For many years Lewis has been studying complex, reacting gas-phase systems at high temperature. The changes that occur in such systems are the result of many individual chemical reactions occurring at the same time. We use a two-step approach to understand what happens in such a system: (1) experimental measurement of the temporal changes in temperature, pressure, or composition of the system, and (2) theoretical computation of these changes in an attempt to match the experimental results. This report describes our work in the computation of complex-system chemical kinetics as focused on combustion systems. Brabbs describes our experimental efforts in his paper for this symposium. Early attempts to compute the progress of complex reactions involved various simplifications. These were of two types: (1) one or two global reactions were substituted for the actual set of many individual, simultaneous reactions which occur in a gaseous system with several species present, and (2) reactions involving some of the very reactive atoms and radicals were assumed to be very fast and, therefore, always in chemical equilibrium. Differential equations for the rates of change of a few key species were solved analytically. Although both of these approaches have had limited success, they only explain some of the general features of a complex reaction. They are, at best, simplified approximations of the actual process, which are only valid under a limited set of conditions. The most fruitful approach to complex kinetics computations is to numerically integrate a system of differential equations derived from the laws of conservation of mass, energy, and (if flow is involved) momentum. These differential equations involve the rates of change of species concentrations σ_i (moles per unit mass of mixture) and temperature T, and they may also involve density ρ and velocity V for a flow process. When these differential equations are solved, a set of individual reactions is assumed to occur simultaneously among all the species, and these reactions are usually assumed to be reversible (with the ratio of

the forward to reverse rate constant being equal to the equilibrium constant for any reaction).

There are two ways to use these detailed kinetic computations. First, they may be used to elucidate a reaction mechanism or to determine a single unknown rate constant in conjunction with experimental data. On the other hand, they may be used with a known mechanism to compute practical combustion quantities such as

(1) Kinetic rocket or jet engine performance
(2) Composition of engine exhaust gases
(3) Ignition delays in combustible mixtures
(4) Ignition lengths and nozzle performance in supersonic combustion

Examples of some of these computations performed at NASA Lewis are given later in this paper.

GENERAL THEORY

A reacting system containing NS species is assumed to have NR independent chemical reactions proceeding simultaneously. The general set of reactions is written

$$\sum_{i=1}^{NS} v_{ij} S_i \underset{k_{-j}}{\overset{k_j}{\rightleftharpoons}} \sum_{i=1}^{NS} v'_{ij} S_i \qquad j=1,2,\ldots, NR$$

Using the law of mass action, we can write the forward and reverse rate of each reaction as

$$R_j = k_j \prod_{i=1}^{NS} (\rho\sigma_i)^{v_{ij}} \qquad (1)$$

$$R_{-j} = k_{-j} \prod_{i=1}^{NS} (\rho\sigma_i)^{v'_{ij}} \qquad (2)$$

where ρ is the mass density of the mixture and σ_i the concentration of species S_i, (moles per unit mass of mixture). The rate constant for the forward reaction k_j is written in the modified Arrhenius form

$$k_j = A_j T^{n_j} e^{-E_j/RT} \qquad (3)$$

The reverse rate constant k_{-j} is obtained from the law of microscopic reversibility:

$$\frac{k_j}{k_{-j}} = (K_{eq})_j \tag{4}$$

In these last equations,

E_j = activation energy for the jth reaction, energy/mol

T = temperature, K

R = universal gas constant

$(K_{eq})_j$ = equilibrium constant for reaction j

For any reacting system, batch or flow, the appropriate continuity equations are differentiated to give a set of differential equations for the variation of the concentrations and temperature with time. For a flow reaction, differential equations for density and velocity will also be obtained. The resulting system of equations is solved numerically in combination with the ideal gas equation of state:

$$\rho = \frac{p}{RT \sum\limits_{i=1}^{NS} \sigma_i} \tag{5}$$

where p is the pressure of the mixture.

For the case of constant pressure and adiabatic batch reaction, the equations are as follows:

$$\frac{d\sigma_i}{dt} = \frac{W_i}{\rho} \quad i=1,2,\ldots, NS \tag{6}$$

where W_i, the molar rate of formation of species S_i, is given by

$$W_i = \sum\limits_{j=1}^{NR} (v'_{ij} - v_{ij})(R_j - R_{-j}) \tag{7}$$

and

$$\frac{dT}{dt} = - \frac{\sum\limits_{i=1}^{NS} W_i h_i}{\sum\limits_{i=1}^{NS} \sigma_i c_{p,i}} \tag{8}$$

where

h_i = molar enthalpy of species S_i

$c_{p,i}$ = molar heat capacity of species S_i

The standard Runge-Kutta or other explicit numerical techniques cannot be used to solve these equations. Although the differential equations are inherently stable, they have widely different time constants for relaxation to their final equilibrium solution. Therefore, the step sizes required for solution stability are prohibitively small. These systems of equations are called stiff, and the problem of solving them accurately has been studied for many years. Several new implicit integration methods have been developed for solving these stiff equations. Although they have been quite successful in improving the accuracy and efficiency of the solutions, there is still a need for additional development of better methods. Problems of accuracy and of efficient step-size selection can still arise. Methods need to be developed for automatic selection of the optimum integration parameters. Therefore, research is actively proceeding at many institutions to develop more efficient integration methods (refs. 1 to 4).

There is another kinetic combustion model of interest to practical engine designers - namely, highly backmixed reacting flow in what is usually called the well-stirred reactor. We assume the limiting condition of zero-dimensional flow or instantaneous backmixing of the reacted gases with the cold, unreacted gases. Although this model is an oversimplification of highly turbulent reacting flow, it is a very useful first-order approximation for some practical reacting-flow systems.

The process is a constant pressure combustion with mass flow rate $\dot{m}$ through a reactor of constant volume v. The average residence time in the reactor is

$$t_r = \frac{\rho v}{\dot{m}} \tag{9}$$

For each species we can write a continuity relation which says the following: The difference between the species molar flow rate into and out of the reactor is equal to its rate of formation (or destruction) by chemical reaction in the reactor. These continuity equations are

$$\frac{\dot{m}}{v}(\sigma_i^* - \sigma_i) + \sum_{j=1}^{NR}(v_{ij}' - v_{ij})(R_j - R_{-j}) \qquad i=1,2,\ldots, NS \tag{10}$$

The following energy conservation equation can also be written (if we assume that the process is adiabatic):

$$\sum_{i=1}^{NS}(\sigma_i h_i - \sigma_i^* h_i^*) = 0 \tag{11}$$

In these equations $*$ indicates the unreacted gas mixture. Equations (10) and (11) are a set of nonlinear, algebraic equations for σ_i and the

reactor temperature. They are solved by the Newton-Raphson iterative procedure. Logarithmic increments of the variables are used to avoid numerical problems (ref. 5).

NASA GENERAL CHEMICAL-KINETICS CODE

Many computer codes have been published which perform different kinds of chemical-kinetic computations. At NASA Lewis we published a general chemical-kinetics code, GCKP84 (ref. 6). It performs a wide variety of chemical-kinetics computations with convenience and efficiency.

It is designed to perform chemical-kinetics computations for several reaction models, including the following:

(1) General reaction in either a batch system or a one-dimensional, frictionless plug flow
(2) Combustion reaction in a well-stirred reactor (highly backmixed flow)
(3) Reaction behind a shockwave with boundary layer corrections
(4) Ignition processes in either a batch or flow system
(5) Nozzle expansion reactions

For each of these models the following general features of the code apply:

(1) Any chemical system may be used for which reaction rate constant data and species thermodynamic data are known.

(2) The process may be adiabatic, or the heat transfer between the reaction and its environment may be considered.

(3) A new efficient integration technique is employed (ref. 7).

(4) Any chemical reaction of the form $aA + bB \rightleftharpoons dD + eE$ may be used, including photochemical and ionic reactions.

(5) Simplified input for combustion reactions may be used.

The code contains an option to compute rocket performance parameters for nozzle flow and can be conveniently used to compute ignition lengths in supersonic flow. An option is also provided to perform a well-stirred reactor computation and, then, immediately expand the products through an assigned nozzle profile.

EXAMPLES OF CHEMICAL KINETIC COMPUTATIONS WITH GCKP84

Hydrogen-Oxygen Batch Reaction at Constant Temperature

Measurements of hydrogen peroxide formation in the constant-volume, isothermal reaction of hydrogen and oxygen at 500 °C were reported many years ago by Baldwin (ref. 8). The important reactions in the hydrogen-oxygen mechanism are as follows:

$$H_2 + O_2 = OH + OH$$

$$H_2 + OH = H_2O + H$$

$$H + O_2 = OH + O$$

$$O + H_2 = OH + H$$

$$*H + O_2 + M = HO_2 + M$$

$$H + HO_2 = OH + OH$$

$$*H_2O_2 + M = OH + OH + M$$

$$*HO_2 + HO_2 = H_2O_2 + O_2$$

$$*H_2 + HO_2 = H_2O_2 + H$$

The rate constants for many of these reactions have been measured fairly accurately, but some of the reactions involving H_2O_2 and HO_2 still have a significant uncertainty. The reactions important in determining H_2O_2 concentration are indicated by an asterisk. GCKP84 was used to compute the H_2O_2 versus time profile. After making several variations of the rate constants for the two most uncertain and important reactions ($H_2 + HO_2 \rightleftharpoons H_2O_2 + H$ and $HO_2 + HO_2 \rightleftharpoons H_2O_2 + O_2$), we obtained the agreement between the experimental and computed results shown in figure 1. This example illustrates the use of kinetics computations in obtaining better rate-constant values for one or two key reactions when all other reactions in a mechanism are fairly well known. Of course, we cannot say that we have uniquely determined both reaction rate constants since we have two adjustable parameters. But we have put limits on their uncertainty. Of course, this type of exercise can only be done when the experimental variable being matched by computation is sensitive to small variations in the uncertain rate constants. This brings up the following general question: For a given change in any rate constant of the reaction mechanism, how much does each computed variable change? This is the relatively new field of study in chemical kinetics called sensitivity analysis.

In practice, even through a chemical mechanism may contain more than 100 reactions, only the rate constants of 15 or 20 may significantly affect the computed results when their values are changed. Recently, methods have been developed to systematically compute these effects in the form of sensitivity coefficients (refs. 9 to 11). This computation is performed along with the chemical-kinetics computation. The results of the latter computation are used as input to solve a second set of differential equations whose unknowns are sensitivity coefficients of the form

$$S_{i\ell} = \frac{k_\ell}{c_i} \frac{\partial c_i}{\partial k_\ell} \tag{12}$$

$$T_{i\ell m} = \frac{k_\ell k_m}{c_i} \frac{\partial^2 c_i}{\partial k_\ell \partial k_m} \tag{13}$$

The first-order coefficient $S_{i\ell}$ effectively gives the percentage change in c_i (ith concentration variable) for a given percentage change in the rate constant of reaction ℓ. The second-order coefficient $T_{i\ell m}$ gives the effect

180

on c_i of changes in both k_ℓ and k_m. It is now recognized that a sensitivity analysis must be performed for any complex reaction in order to pinpoint the important reaction paths and obtain a good understanding of the reaction mechanism.

Computation of Rocket Performance

One of the first uses of chemical kinetic computations was in the computation of rocket performance using a one-dimensional flow model. This performance is measured by the velocity of the hot gas at the nozzle exit point. As the gas expands and cools, its velocity (i.e., kinetic energy) is kept as high as possible by chemical recombination reactions which occur in the nozzle. These reactions convert high-potential-energy atoms and radicals into low-energy stable molecules. Maximum performance is obtained if these reactions maintain equilibrium conditions in the very short nozzle-residence time. But this is often not the case since the finite rates of the reactions are not fast enough. By knowing the rate constants for the important recombination processes one can compute kinetic performance that more accurately and realistically reflects the experimentally measured performance. An example of this is shown in figure 2 for the oxygen difluoride - diborane system (ref. 12). The three curves of performance as a function of oxidant/fuel ratio (fig. 2(b)) show the maximum and minimum theoretical performance (assuming equilibrium and frozen conditions) as well as the kinetically limited performance. The latter agrees rather well with actual measurements corrected for various losses. The reaction mechanism used is shown in table I. This system is interesting because only one reaction rate constant has to be accurately known in order to compute the kinetic curve. This is the recombination of hydrogen atoms to give molecular hydrogen. This fact was determined by a simple sensitivity analysis. Computed performance is unchanged for wide variations of the other rate constants. The reason for this situation can be seen from the heat release data in table I. The hydrogen atom recombination accounts for well over 50 percent of the heat release in the process, and this, of course, controls performance.

Two-Stage Well-Stirred Reactor

The practical use of the well-stirred reactor model of GCKP84 is illustrated by its simulation of a two-stage turbulent combustor. A theoretical and experimental study of two-stage, rich-lean combustion as a method of controlling nitrogen oxide emissions was performed at Lewis. This technique was suggested as a way of reducing the conversion of the organic nitrogen compounds in hydrocarbons (fuel-bound nitrogen) to nitric oxide during combustion. The objective of the work was to study the effect of operating conditions on emissions of both nitrogen oxides (NO_x) and carbon monoxide (CO) (ref. 13). Both the nitrogen and the hydrogen content of the fuel were changed to simulate coal-derived syncrude fuels. These fuels contain high percentages of aromatic hydrocarbons and therefore have a lower hydrogen-to-carbon ratio than today's petroleum-based fuels. Experiments were performed in the two-stage flame-tube apparatus shown in figure 3. The fuels were mixtures of propane, toluene, and pyridine blended to give a range of hydrogen and nitrogen contents. The primary-zone equivalence ratio was varied from 0.7 to about 1.8. The products of first-stage combustion were rapidly diluted with air injection

and burned at a final equivalence ratio of 0.5. The final NO_x and CO concentrations were measured. The two-stage flame tube was modeled analytically by a two-stage stirred-reactor computation closely simulating the experimental fuels. Instantaneous mixing of the secondary dilution air was assumed. A detailed chemical mechanism was used for propane and toluene oxidation and for NO_x formation. The fuel-bound nitrogen was input as nitrogen atoms and all mixing and heat-transfer effects were neglected. This very simplified model of a quite complex process was able to predict most of the observed trends of NO_x and CO formation with variation of nitrogen and hydrogen concentrations in the fuel. The model's prediction of other trends, which were not measured experimentally, gave additional information about the advantages and disadvantages of using this rich-lean combustion for emissions control. A comparison of some experimental and computed results for NO_x and CO concentration as a function of primary equivalence ratio is given in figures 4 and 5. The simple model qualitatively predicts the observed trends. It can be seen that using a rich primary equivalence ratio does reduce NO_x formation very significantly. However, at the same time, this technique increases the formation of CO, which is also undesirable. Thus, one set of conditions cannot minimize both pollutants, and tradeoffs will have to be made to obtain desired emissions levels for any practical situation. This work has shown that a simple kinetic model can sometimes be used to qualitatively explain the observed trends in a highly complicated combustion system.

Ignition Delays in Benzene-Oxygen-Argon Mixtures

Our current work involves the study of the mechanism of hydrocarbon oxidation. We are studying the aliphatic hydrocarbons by measuring ignition delays and concentration profiles during the shock-heated oxidation of hydrocarbon-oxygen-argon mixtures. Then a detailed chemical mechanism is formulated and used in detailed kinetics computations to match the observed experimental data over a wide range of initial composition, temperature, and pressure. We are also studying the simplest aromatic, benzene. A partial mechanism for benzene oxidation is as follows:

$$C_6H_6 + O_2 = C_6H_5 + HO_2$$

$$C_6H_6 = C_6H_5 + H$$

$$C_6H_6 = C_4H_4 + C_2H_2$$

$$H + O_2 = OH + O$$

$$H + O_2 + M = HO_2 + M$$

$$O + C_6H_6 = C_6H_5 + OH$$

$$OH + C_6H_6 = C_6H_5 + H_2O$$

$$C_6H_5 + O_2 = C_6H_5O + O$$

$$C_6H_5O + M = C_5H_5 + CO + M$$

$$CO + OH = CO_2 + H$$

The experimental program is described by T.A. Brabb's paper presented at this symposium. I attempted to match experimental ignition delay data for benzene-oxygen-argon mixtures that were taken by another investigator at Lewis. The reaction zone behind the experimental reflected shock is approximated by a constant volume batch reaction. The theoretically computed temperature and pressure (for nonreacting conditions) behind the shock are used as starting conditions. A typical, computed profile of pressure as a function of time is shown in figure 6. The ignition delay τ is determined from the first significant pressure rise; this is similar to determining the experimental τ value from the measured pressure trace. The mechanism we used includes over 100 reactions involving benzene and its degradation products, acetylene, phenol, phenylacetylene, ethylene, and methane. It includes all the reactions of the hydrogen-oxygen system as well. Values from the literature were used for all reaction rate constants except the quite uncertain ones of the benzene, phenol, and phenylacetylene reactions. These were varied within reasonable limits to get the best overall agreement between computed and experimental τ values. Starting mixture equivalence ratios ranged from 0.5 to 2, temperatures ranged from about 1200 to 1700 K, and initial pressures ranged from 2 to 6 atm. A simple sensitivity study made by changing rate constants one at a time has shown that the τ values are most sensitive to the rate constant for the $C_6H_5 + O_2$ reaction, which is quite uncertain. Other rate constants which are uncertain and have a significant effect are those for $C_6H_6 \rightleftharpoons C_4H_4 + C_2H_2$ and $C_6H_5 \rightleftharpoons C_4H_3 + C_2H_2$. In figure 7 we show some comparisons between computed and experimental ignition delays. We have used only the experimental data points which are considered the most accurate for the mechanism matching. These are the data with τ values of 100 msec or greater. Shorter ignition delays may have significant error due to the nonuniformity of the reaction mixture and the heating effects. The computed line for $\log \tau$ versus $1/T$ comes within ±50 percent for all but one point which differs by about a factor of two. While this mechanism does fairly well, it is certainly not complete and has two significant problems. First, it tends to predict delays longer than the experimental ignition delays for the lean mixtures and shorter than the experimental delays for the rich mixture. Second, it does not predict the experimentally observed effect of dilution with argon at a constant equivalence ratio of 1.0. Therefore, more work needs to be done on this oxidation mechanism. A full understanding of the oxidation will probably not be achieved until further experimental data are obtained on concentration profiles of a key species, such as the phenyl radical or carbon dioxide. Work along these lines is proceeding at Lewis and other laboratories.

REFERENCES

1. Hindmarsh, A.C.: Linear Multistep Methods for Ordinary Differential Equations: Method Formulations, Stability and the Methods of Nordsieck and Gear. UCRL-51186-Rev 1 Lawrence Livermore Laboratory, 1972.

2. Radhakrishnan, K.: Comparison of Numerical Techniques for Integration of Stiff Ordinary Differential Equations Arising in Combustion Chemistry, NASA TP-2372, 1984.

3. Radhakrishnan, K.: Integrating Chemical Kinetic Rate Equations by Selective Use of Stiff and Nonstiff Methods. AIAA Paper 85-0237, Jan. 1985.

4. Pratt, D.T.; and Radhakrishnan, K.: CREKID: A Computer Code for Transient, Gas Phase Combustion Kinetics. NASA TM-83806, 1984.

5. Pratt, D.T.: PSR-A Computer Program for Calculation of Steady Flow Homogenous Combustion Reaction Kinetics. Washington State University, Dept. of Mech. Eng., Bulletin 336, 1974.

6. Bittker, D.A.; and Scullin, V.J.: GCKP84-General Chemical Kinetics Code For Gas-Phase Flow and Batch Processes Including Heat Transfer Effects. NASA TP-2320, 1984.

7. Zeleznik, F.J.; and McBride, B.J.: Modeling the Internal Combustion Engine, NASA RP-1094, 1985, Chapter 2.

8. Baldwin, R.R.; Rossiter, B.N.; and Walker, R.W.: Hydrogen Peroxide Yields in the Hydrogen + Oxygen Reaction. Reaction of HO_2 Radicals With Hydrogen. Trans. Faraday Soc., vol. 65, no. 556, Part 4, Apr. 1969, pp. 1044-1050.

9. Dunker, A.M.: The Decoupled Direct Method for Calculating Sensitivity Coefficients in Chemical Kinetics. J. Chem. Phys, vol. 81, no. 5, Sept. 1, 1984, pp. 2385-93.

10. Kramer, M.A.; Rabitz, H.; Calo, J.M.; and Kee, R.J.: Sensitivity Analysis in Chemical Kinetics: Recent Developments and Computational Comparisons, Int. J. Chem. Kinetics, vol. 16, no. 5, May 1984, pp. 559-578.

11. Yetter, R.; Eslava, L.A.; Dryer, F.L.; and Rabitz, H.: Elementary and Derived Sensitivity Information in Chemical Kinetics, J. Phys. Chem., vol. 88, no. 8, Apr. 12, 1984, pp. 1497-1507.

12. Bittker, D.A.: Theoretical Nonequilibrium Performance of Oxygen Difluoride-Diborane Rocket Propellant. NASA TN D-4992, 1969.

13. Bittker, D.A.; and Wolfbrandt, G.: Effect of Fuel Nitrogen and Hydrogen Content on Emissions in Hydrocarbon Combustion. ASME Paper 81-GT-63, Mar. 1981.

TABLE I. - OF_2-B_2H_6 MECHANISM

[Equivalence ratio = 1.63.]

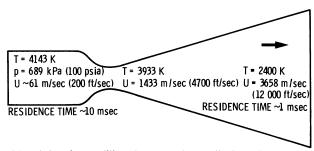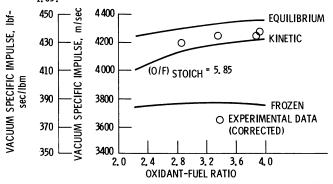| Reaction	Net reaction rate, percent	Heat of reaction, ΔH, kcal/mole	Energy release rate, percent
$H + H + M \rightleftharpoons H_2 + M$	32.3	-104	53.1
$BO + HF \rightleftharpoons BOF + H$	26.8	-33	13.9
$H + F + M \rightleftharpoons HF + M$	5.1	-136	11.1
$H + OH + M \rightleftharpoons H_2O + M$	5.2	-119	9.8
$BF + OH \rightleftharpoons BOF + H$	3.9	-58	3.5
$F + H_2 \rightleftharpoons HF + H$	4.5	-32	2.3
$H_2 + OH \rightleftharpoons H_2O + H$	9.7	-15	2.3
$BF + O \rightleftharpoons BO + F$	9.3	8	1.2
$H + BF_2 \rightleftharpoons HF + BF$	2.4	-25	1.0
$BO + F + M \rightleftharpoons BOF + M$	.3	-169	.7
$BF + O + M \rightleftharpoons BOF + M$	.2	-160	.6
$O + H + M \rightleftharpoons OH + M$	.3	-102	.5
Total	100.0		100.0
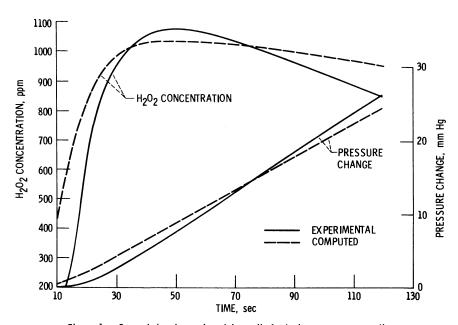
Figure 1. - Computed and experimental results for hydrogen-oxygen reaction. Temperature, T, 500 °C.

185
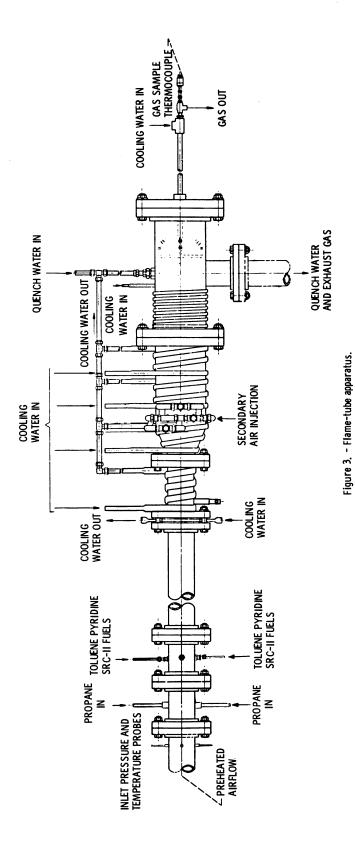
(a) Rocket engine conditions for OF_2-B_2H_6 propellant. Equivalence ratio, 1.63.

(b) Performance of OF_2-B_2H_6 rocket propellant. Chamber pressure, 689 kPa (100 psia).

Figure 2. - Oxygen difluoride-diborane (OF_2-B_2H_6) rocket combustion.
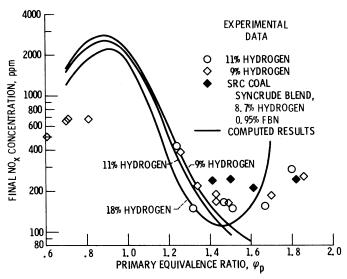
Figure 3. – Flame-tube apparatus.

187

Figure 4. - Effect of hydrogen content on NO_x emissions. Fuel-bound nitrogen, 1.0 percent; secondary equivalence ratio, 0.5; secondary residence time, $\cong$ 2 msec.
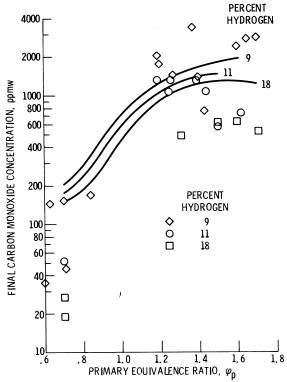

Figure 5. - Effect of percent hydrogen on carbon monoxide emissions for hydrocarbon combustion. Fuel-bound nitrogen, 0 percent; secondary equivalence ratio, 0.5; secondary residence time, $\cong$ 2 msec.
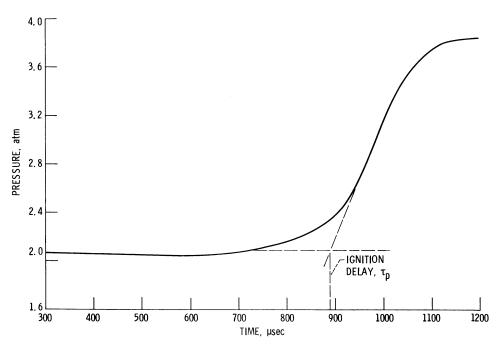
188

Figure 6. – Computed pressure as function of time for benzene-oxygen-argon shock ignition. Initial temperature, 1366 K; equivalence ratio, φ, 2.0.
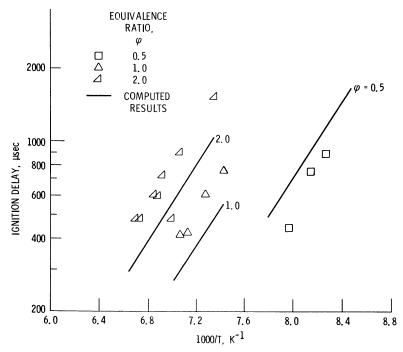

Figure 7. – Ignition delay data for benzene-oxygen-argon mixtures.

EXPERIMENTAL INVESTIGATION OF PILOTED FLAMEHOLDERS

C.F. Guo, Y.H. Zhang, and Q.M. Xie
Gas Turbine Research Institute
Jiangyou County of Sichuan, People's Republic of China

Four configurations of piloted flameholders were tested. The range of flame stabilization, flame propagation, pressure oscillation during ignition, and pressure drop of the configurations were determined. Some tests showed a very strong effect of inlet flow velocity profile and flameholder geometry on flame stabilization.

INTRODUCTION

Pressure oscillation during the transient period from ignition to maximum augmentation is a critical problem for the turbofan augmentor. Since this pressure oscillation may cause fan flow to stall or surge, it is important to know the peak pressure during augmentor ignition and to take some kind of technical measure to reduce this peak pressure. Such a procedure is called "soft ignition."

The combustion process in the fan flow of a turbofan augmentor is under a severe condition. It is helpful to understand how to make use of the hot combustion products in the core stream to ignite the combustible mixture in the cold fan stream. The present research compares the capability for soft ignition and the ability of different configurations of piloted flameholders to ignite a cold fan stream.

SYMBOLS

C   pressure loss coefficient

F   area

G_a air-mass flow rate

G_f fuel flow rate

h   gap height of V-gutter or peripheral length of test section

M   Mach number

P   pressure, kg/cm^2

P*   stagnant pressure, kg/cm^3

ΔP pressure drop or pressure oscillation value, kg/cm^2

T   temperature, °C

T*   stagnant temperature, °C

V   velocity, m/sec

AFR   air-fuel ratio

Subscripts:

0   upstream of flow orifice

1   downstream of flow orifice or upstream of air heater

2   inlet of test section

3   outlet of test section

a   air or ambient

ave   average

APPARATUS

The test apparatus is shown in figure 1. The airflow from the compressor is divided into two streams: one stream goes to ejector 7 to create a low-pressure exhaust condition for the test section; the other stream goes through valve 1, flow-orifice meter 2, air heater 3, control valve 4, and plenum chamber 5 into test section 6. After leaving the test section the combustion products are cooled by water injection. The hot gas is exhausted into the ambient through the ejector.

The test rig assembly is shown in figure 2. It is a rectangular duct 300 mm by 175 mm. The piloted flameholder is mounted inside the test section by bolts. Flame extinction is recorded through a quartz window by a flame-detection device. Flame extinction can also be observed visually. The ignition in the primary zone is provided by a high-energy ignitor of 12 J. The combustible mixture in the secondary zone is ignited by flame propagation from the primary zone. The inlet flow is measured by the static pressure tap, the stagnant pressure tube, and the chromel-alumel thermocouple. The outlet temperature is monitored by a platinum/platinum-rhodium thermocouple. Outlet stagnant pressure is measured by three water-cooled stagnant pressure probes; each has three measuring points. The transient pressure is measured by an induction-type pressure transducer ($C_\gamma G$-1, 0 to 1.0 kg/cm^2) with an LR-1 carrier wave amplifier and an Sc-60 ultraviolet oscilloscope. The fuel flow rate is measured by a turbine-type flowmeter with a digital frequency indicator.

The fuel is injected through a spray bar. There is one spray bar in the primary zone. The total length of the bar is 280 mm. There are six pairs of holes (0.4 mm in diam) on the bar at an intersection angle of 60°. In the secondary zone there are six spray bars. The two bars in the center have four pairs of holes (0.35 mm in diam) at an intersection angle of 30°; the other four spray bars have four holes (0.35 mm in diam) each. Fuel injection in the secondary zone is in the counterflow direction. The test configurations of piloted flameholders are shown in figure 3.

TEST METHOD

The test conditions were as follows:

T_2^* 60 to 70 °C or 500 °C

M_2 0.23

P_2^* 0.25 to 1.2 kg/cm^2

The test procedures were as follows: First, the air supply was adjusted to maintain the inlet conditions of P_2^*, M_2, and T_2^* as specified. After the primary zone had been ignited the ejector air supply was adjusted to maintain P_2^*, M_2, and T_2^* constant. Then the fuel flow in the primary zone G_{fp} was increased until fuel-rich flameout occurred. After that, the primary zone was reignited at the specified inlet condition and P_2^*, M_2, and T_2^* were kept constant. Finally, the fuel flow was reduced until there was fuel-lean flame extinction. Before ignition, the pressure drop between the inlet and outlet was measured. During ignition the peak pressure, the fuel-air mixture in the secondary zone, and the pressure oscillation were also recorded.

RESULTS AND DISCUSSION

Peak Pressure Measurements

As shown in figure 4, the peak pressure rise during ignition is usually lower than 10 percent of the inlet pressure ($\Delta P_2/P_2^* < 10$ percent). The peak pressure rise in the augmentor is normally related to the amount of fuel injected (as in these tests). Since the ignition is realized in a small volume, the amount of fuel necessary for ignition is small. Thus, the peak pressure is lower than that for normal augmentor ignition. This proves that using a piloted flameholder makes it easier to obtain a soft ignition in a turbofan augmentor.

Pressure Oscillation Measurements

Pressure oscillation measurements were performed under the same conditions as the peak pressure measurements. The amount of fuel injected in the primary zone has a very strong effect on the pressure oscillation in the augmentor during ignition in the secondary zone (figs. 5(a) and (b)). It has been shown that, with the same amount of fuel injected in the secondary zone, the pressure oscillation during the onset of secondary combustion varies with the amount of fuel injected in the primary zone. It is clear that there is an optimum fuel injection in the primary zone which minimizes the pressure oscillation during secondary zone ignition.

Flow Resistance

Figure 6 shows the variation of the pressure loss coefficient with the Reynolds number Re for different configurations. When Re increases, the pressure loss coefficient C decreases slightly. The pressure loss coefficient C also decreases with the increase of gap height h. The pressure loss coefficient C for a V-gutter is slightly lower than that for a semispherical shape.

Effect of Inlet Flow Distortion

The inlet flow distortion is shown in figure 7. Figure 8 shows the effect of inlet flow distortion on flame stabilization. When the inlet flow is distorted, the range of flame stabilization is narrowed, and the peak value of the stabilization parameter is also reduced. For instance, at $P_2^* = 0.25$ kg/cm^2 when there is no inlet distortion, it is possible to ignite the secondary zone in 3 sec; but, when there is inlet distortion (even at $P_2^* = 0.3$ kg/cm^2), the range of flame stabilization is very narrow and the ignitability in the secondary zone is very weak. (It is impossible to ignite the fuel-air mixture in the secondary zone.)

Effect of Secondary Air Entry Holes on Stabilization of the SJ410-4A Flameholder

When 54 secondary holes (8 mm in diam) are opened, the range of flame stabilization is very narrow (fig. 9). When these holes are blocked, the stabilization range is broader. The secondary air entry holes also reduce the capability of igniting the fuel-air mixture in the secondary zone. It seems that the secondary air dilutes the primary combustion products and reduces the temperature.

Effect of Gap Height

Figure 10(a) and (b) show the effect of gap height h on flame stabilization for the SJ410-4B and SJ410-3A configurations. The range of flame stabilization decreases with the increase of the gap height h, and the ignitability also decreases. From this test we found that, for a specified configuration, there is an optimum gap height. For instance, when the width of the V-gutter is 70 mm (SJ410-3A), the optimum gap height is 3 to 5 mm, the width of V-gutter is 40 mm (SJ410-4B), and the optimum gap height is 2 to 3 mm. Under these conditions, the range of ignition and flame stabilization and the ignition capability in the secondary zone are nearly the same for the two configurations.

Effect of Bluff Body Shape on Flame Stabilization

Figure 11(a) shows the flame stabilization range for the SJ410-3A configuration under ambient air temperature with a different bluff body shape. The range of flame stabilization of the V-gutter bluff body is wider than that of the semispherical bluff body. But as shown in figure 11(b), at $T_2^* = 500$ °C the ranges of flame stabilization for both bluff bodies are nearly the same. This can be explained as follows. At high inlet temperature, the vaporization rate of the fuel spray (before entering the primary zone) is high for both flameholders; therefore, the gaseous fuel-air ratios of the mixtures in the primary zone are nearly the same. But at low temperature, the fuel vaporization rate on the V-gutter surface is higher than that on the semi-spherical body, and the fuel-air ratio in the primary zone of the V-gutter is higher than that of the semi-spherical body. Thus, the V-gutter has a wider range of flame stabilization.

Effect of Air Entry Holes in V-Gutter Wall on Flame Stabilization

Figure 12 shows the range of flame stabilization for the SJ410-3B configuration with different air entry holes in the V-gutter wall. For a given

opening area, fewer holes with larger diameters offer better flame stabilization than smaller holes. A comparison of figure 10(b) with figure 12 shows that the recirculation zone created by the gap provides better flame stabilization than that created by circular holes.

CONCLUSIONS

These tests led to the following conclusions.

(1) The use of a piloted flameholder in the turbofan augmentor may minimize the peak pressure rise during ignition. At the present experimental conditions, $\Delta P/P_2^*$ is less than 10 percent; therefore, the use of a piloted flameholder is a good method to realize soft ignition.

(2) The geometry of the piloted flameholder and the amount of fuel injected into the flameholder have a strong effect on the pressure oscillation during ignition of the fuel-air mixture in the secondary zone.

(3) Compared with the V-gutter flameholder with holes in its wall, the V-gutter flameholder without holes not only has the advantages such as simple structure and good rigidity but offers a wide combustion stability limit and a high capability of igniting the fuel-air mixture of the secondary zone.

BIBLIOGRAPHY

Branstetter, J.R.; and Juhasz, A.J.: Experimental Performance and Combustion Stability of a Full Scale Duct Burner for a Supersonic Turbofan Engine. NASA TN D-6163, 1971.

Cullom, R.R.; and Johnsen, R.L.: Operating Condition and Geometry Effects on Low-Frequency Afterburner Combustion Instability in a Turbofan at Altitude. NASA TP-1475, 1979.

Kurkov, A.P.: Turbofan Compressor Dynamics During Afterburner Transients. NASA TM X-71741, 1975.

Marshall, R.L.; and Canuel, G.E.: Augmentation Systems for Turbofan Engines. Presented at Crafield International Symposium, 1976.
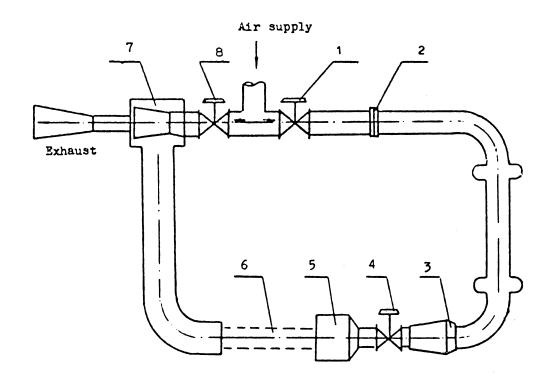
Figure 1. - Test apparatus. Valve, 1; orifice flowmeter,
2; air heater, 3; control valve, 4; plenum chamber,
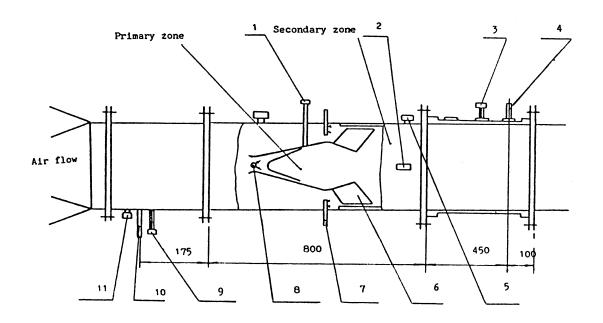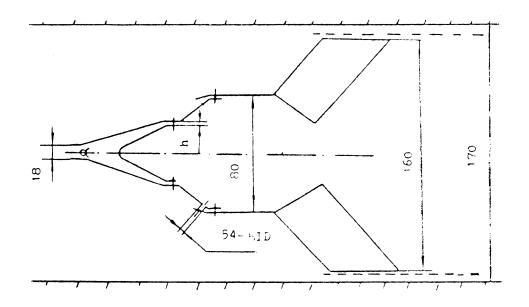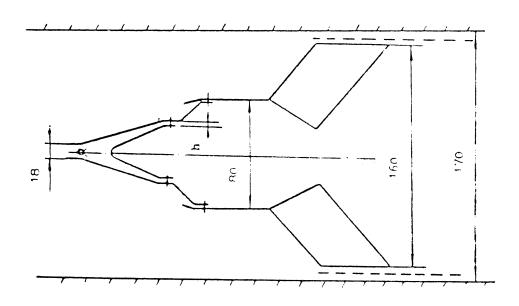5; test section, 6; ejector, 7; valve, 8.

Figure 2. - Test rig assembly. High energy ignitor, 1; quartz
window, 2; thermocouple, 3; pressure probe, 4; pressure
transducer, 5; test configuration, 6; fuel spray, 7; fuel
spray bar, 8; thermocouple, 9; pressure probe, 10; pressure
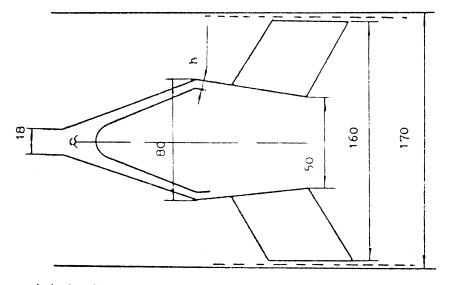tap, 11.
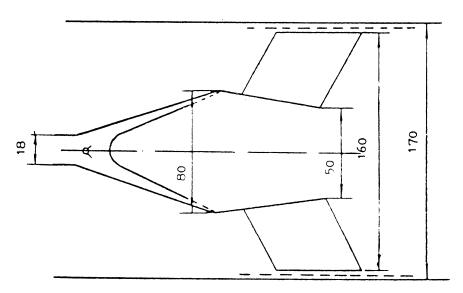
196

(a) Configuration SJ410-4A; h = 4 mm.

(b) Configuration SJ410-4B; h = 2, 3, 4, and 6 mm.

Figure 3. - Test configurations of piloted flameholders.
(All dimensions in mm.)

197

(c) Configuration SJ410-3A; h = 3, 5, and 7 mm.

(d) Configuration SJ410-3B.

Type	Spacing	Number	Diameter
A	30	34	12mm
B	14	76	8mm
C	7	304	4mm

(e) Air-entry holes on the V-gutter.

Figure 3. - Concluded.

198

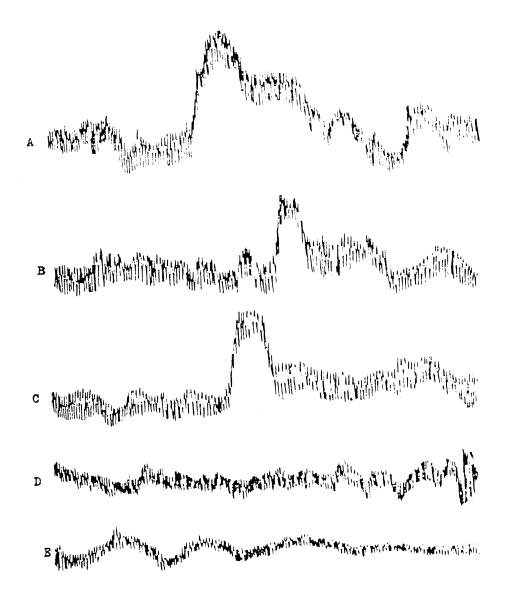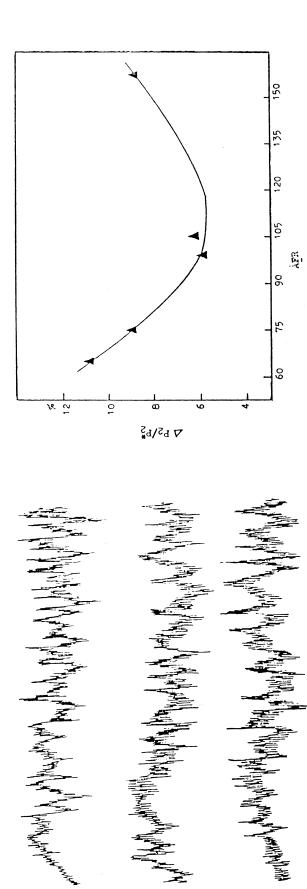| Type	A	B	C	D	E
P_2^* kg/cm^2	1.2	0.8	0.6	0.4	0.3
$\triangle P_2$ kg/cm^2	0.057	0.047	0.051	0.0085	0.0085
$\triangle P_2/P_2^*$ %	4.8	5.9	2.5	2.1	2.8

Figure 4. - Pressure oscillation during ignition.
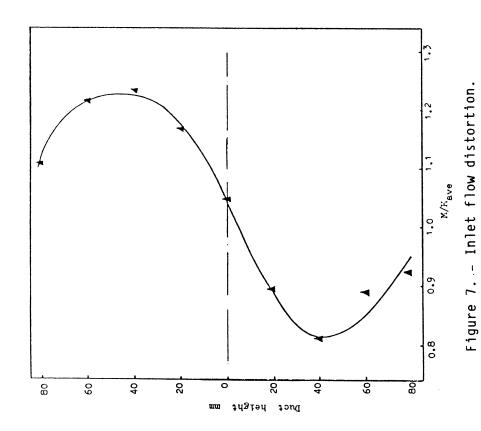
(b) Relation between the pressure oscillation and the fuel flow injected in the primary zone.

Type		A	B	C	D	E
P_2^*	kg/cm^2	0.4	0.4	0.4	0.4	0.4
ΔP_2	kg/cm^2	0.034	0.024	0.036	0.043	0.025
$\Delta P_2/P_2^*$	%	8.5	5.0	9.0	11	6.7
AFR		157	100	74	65	104

(c) Test conditions.

(a) Pressure oscillation during combustion starting in the secondary zone.

Figure 5. – Pressure oscillation in the secondary zone.
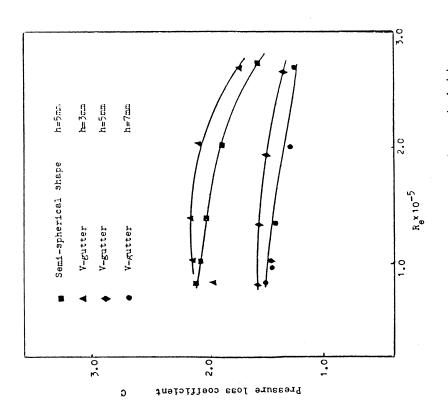
Figure 7. - Inlet flow distortion.

Figure 6. - Effect of shape and gap height on pressure loss coefficient.
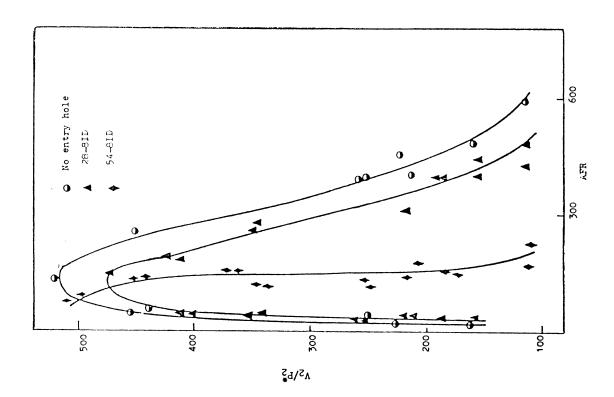
Figure 9. – Effect of secondary air-entry holes on flame stabilization. Configuration SJ410-4A; $T_2^* = 500\ °C$, $M_2 = 0.23$.
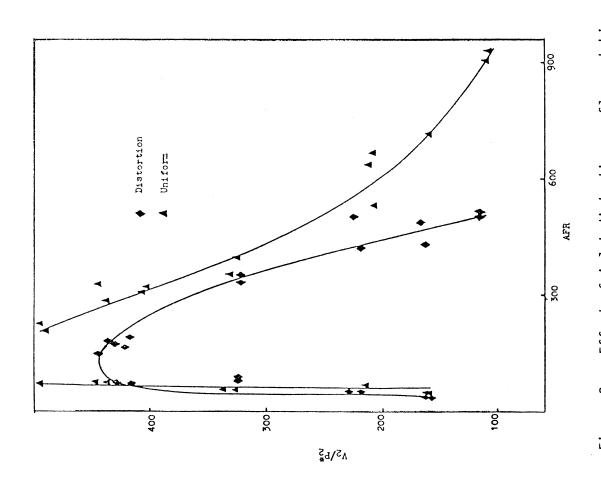
Figure 8. – Effect of inlet distortion on flame stabilization. Configuration SJ410-4B; $T_2^* = 500\ °C$, $M_2 = 0.23$.

(a) Configuration SJ410-4B; $T_2^* = 500 \,°C$, $M_2 = 0.23$.   (b) Configuration SJ410-3A; $T_2^* = 500 \,°C$, $M_2 = 0.23$.
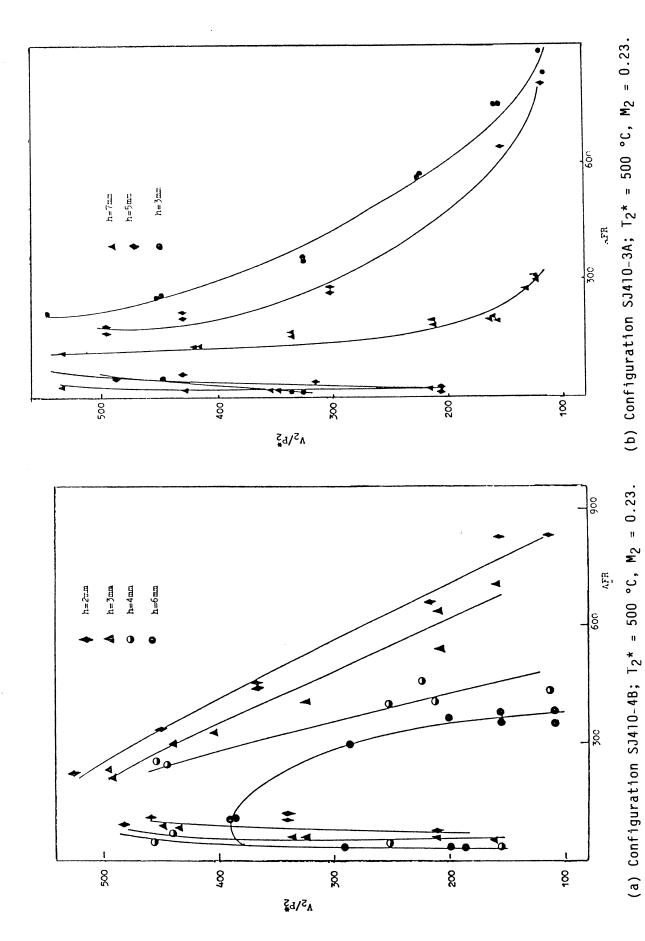
Figure 10. - Effect of gap height on flame stabilization.

203

(a) Configuration SJ410-3A; $T_2^* = 60$ °C, $M_2 = 0.23$.

(b) Configuration SJ410-3A; $T_2^* = 500$ °C, $M_2 = 0.23$.

Figure 11. - Effect of bluff body shape on flame stabilization.

204

Figure 12. - Effect of air-entry holes in V-gutter wall on flame stabilzation. Configuration SJ410-3B; $T_2^* = 500\ °C$, $M_2 = 0.23$.
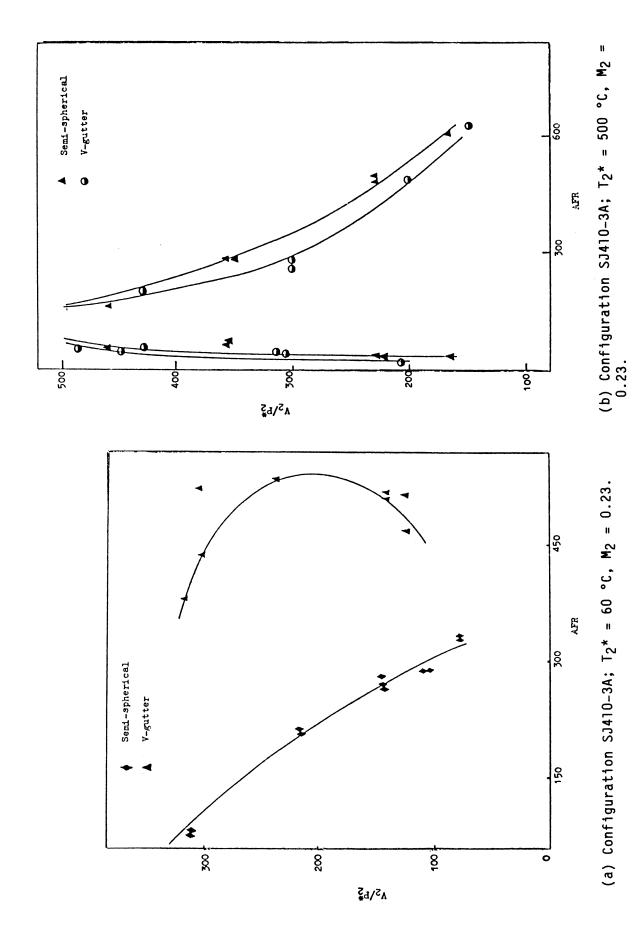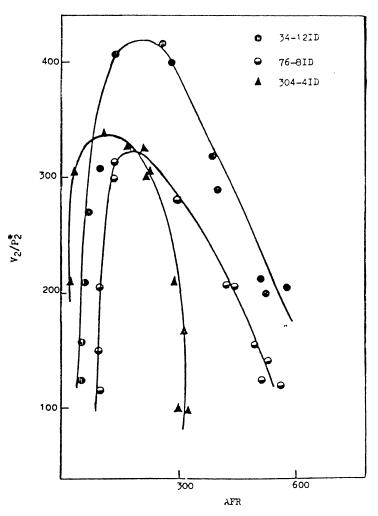
205

THE CHEMICAL SHOCK TUBE AS A TOOL FOR STUDYING HIGH-TEMPERATURE CHEMICAL KINETICS

Theodore A. Brabbs
NASA Lewis Research Center
Cleveland, Ohio

Although the combustion of hydrocarbons is our primary source of energy today, the chemical reactions, or pathway, by which even the simplest hydrocarbon reacts with atmospheric oxygen to form CO_2 and water may not always be known. Furthermore, even when the reaction pathway is known, the reaction rates are always under discussion. The shock tube has been an important and unique tool for building a data base of reaction rates important in the combustion of hydrocarbon fuels.

The ability of a shock wave to bring the gas sample to reaction conditions rapidly and homogeneously makes shock-tube studies of reaction kinetics extremely attractive. In addition to the control and uniformity of reaction conditions achieved with shock-wave methods, shock compression can produce gas temperatures far in excess of those in conventional reactors. Argon can be heated to well over 10 000 K, and temperatures around 5000 K are easily obtained with conventional shock-tube techniques. Experiments have proven the validity of shock-wave theory; thus, reaction temperatures and pressures can be calculated from a measurement of the incident shock velocity.

This report presents a description of the chemical shock tube and auxiliary equipment and of two examples of kinetic experiments conducted in a shock tube. Shock-wave theory and shock tubes in general are discussed in references 1 and 2 and thus are not included in this report.

EXPERIMENTAL APPARATUS AND PROCEDURES

The chemical shock tube used was a single piece of square stainless-steel tubing (5.7 m long, 6.4 cm on a side, 1.3 cm thick walls). The entire length of the tube was ground to a constant inside dimension and then honed to a highly polished finish. Stations for shock-wave detectors were located at 15-cm intervals in the downstream portion of the tube. Two 2.5-cm calcium fluoride windows were located 25 cm from the end of the tube. A quartz pressure transducer was located at a position where it would provide an accurate indication of the time at which a shock wave arrived at the center of the windows. The assembled tube could be evacuated to a pressure of about 1 μm and had a leak rate of less than 0.2 μm/min. A liquid nitrogen cold trap in the vacuum line guarded against the back-migration of pump oil into the shock tube.

The temperature and pressure behind the incident and reflected shock waves were calculated from the measured velocity of the incident shock wave with the shock program of Gordon and McBride (ref. 3). Since the reaction temperature had to be calculated, it was very important to measure the initial temperature and the shock velocity as accurately as possible. The distances between probe locations were accurately measured to four significant figures. The shock-tube wall temperature was measured to ±0.5 C, and it was assumed that the test mixture rapidly achieved this temperature. Thin-film resistance gauges (1.3 cm

diam) were used to detect the passage of the incident shock wave. The amplified output from these gauges was displayed on a digital oscilloscope (see fig. 1). Data points were recorded every 200 nsec. Since with this scope the scale can be magnified to allow viewing of each point, we were able to measure the incident shock velocity to better than ±0.2 μsec (0.1 percent).

All data were taken at an initial test gas pressure of 8.00 kPa (60 torr) and a driver pressure of 792.7 kPa (115 psia). Soft aluminum diaphragms separated the high-pressure driver gas from the test gas. These diaphragms were pressurized and then pierced by a gas-activated piston. The shock strength was varied by adding small amounts of argon to the helium driver gas to change its molecular weight. Figure 2 shows the variation of shock velocity with the reciprocal of the molecular weight of the driver gas. The constant pressure ratio across the diaphragm insured that the opening process for the diaphragm was about the same for all tests.

Gas mixtures were prepared by the method of partial pressures in 34.4-liter stainless-steel tanks. The gases used to prepare the mixtures had stated purities of 99.99-percent methane, 99.98-percent oxygen, and 99.998-percent argon. The partial pressure of methane and oxygen could be determined to better than 0.3 mm of Hg, and the total pressure of the tank to better than 1.38 kPa (0.2 psia). All samples were prepared to a total pressure of 413.6 kPa (60 psia).

Radiation at 3700 Å was monitored for each experiment and was displayed on the oscilloscope with the pressure history. The radiation was detected by a photomultiplier tube whose field of view was restricted by two slits (0.75 and 1.5 mm wide) located 10 and 23 cm from the center of the shock tube. With this arrangement we could view a 3-mm slice of the hot gas in the center of the shock tube at the same location as the pressure transducer. An interference filter centered at 3696.5 Å (with a half band width of 115 Å) was used to isolate the 3700 Å radiation. The filter transmitted 51 percent of the incident radiation.

Examples of kinetic experiments conducted in a shock tube are presented in the next two sections.

SHOCK TUBE MEASUREMENTS OF SPECIFIC REACTION RATES IN THE BRANCHED-CHAIN H_2-CO-O_2 SYSTEM

When a mixture containing hydrogen, carbon monoxide, and oxygen is subjected to a temperature and pressure pulse in a shock tube, small concentrations of atoms and free radicals are first formed by processes such as

$$CO + O_2 \longrightarrow CO_2 + O$$

These concentrations may then grow exponentially via the well-known branched-chain scheme

$$OH + H_2 \xrightarrow{\quad k_1 \quad} H_2O + H \qquad\qquad I$$

$$H + O_2 \xrightarrow{k_2} OH + O \qquad\qquad II$$

$$O + H_2 \xrightarrow{k_3} OH + H \qquad\qquad III$$

$$H + O_2 + M \xrightarrow{k_4} HO_2 + M \qquad\qquad IV$$

$$OH + CO \xrightarrow{k_5} CO_2 + H \qquad\qquad V$$

Theory shows (refs. 4 and 5) that the oxygen atom concentration grows as $[O] \cong A \exp \lambda t$, (except very early in the reaction). Where λ is the positive root of the cubic equation

$$\lambda^3 + (v_1 + v_2 + v_3 + v_4 + v_5)\lambda^2 + [(v_1 + v_5)(v_3 + v_4) + v_3 v_4]\lambda$$

$$- v_3(v_1 + v_5)(2v_2 - v_4) = 0 \qquad (1)$$

where $v_1 \equiv k_1[H_2]$, $v_2 \equiv k_2[O_2]$, $v_3 \equiv k_3[H_2]$, $v_4 \equiv k_4[O_2][M]$, and $v_5 \equiv k_5[CO]$.

Thus, the exponential growth constant λ depends on the gas composition and the rate constants of reactions I to V. This paper reports measurements of mixtures chosen to permit determination of the rates of reactions I, II, III, and V. Mixtures were selected by analyzing equation (1).

Growth constants were obtained by measuring the blue carbon monoxide flame-band emission behind incident shocks. The intensity of this radiation is proportional to the product of carbon monoxide and oxygen atom concentrations (ref. 6), and, since very little carbon monoxide is consumed, the light monitors the increase of oxygen atom concentration with time. A typical emission record is presented in figure 3.

Exponential growth constants were obtained from plots of the logarithm of observed light intensity as a function of gas time (see fig. 4); the relation between gas and laboratory times was obtained from the computer calculations.

SELECTION OF GAS MIXTURES

Let us turn now to the rationale used to select gas mixtures by analyzing equation (1). To begin with, under our experimental conditions v_4 is generally small in comparison with other v; therefore, it can be neglected for purposes of a qualitative discussion. Secondly, λ turns out to be a small positive root - of the order of the smaller v values and very small compared with the larger v values. Thus, we neglect λ^3 in comparison with the other terms and rewrite equation (1) as

$$[(v_1 + v_5) + v_2 + v_3]\lambda^2 + v_3(v_1 + v_5)\lambda \cong 2v_2 v_3(v_1 + v_5) \qquad (2)$$

If the amount of hydrogen in a mixture is large in comparison to the amount of oxygen, v_1 and v_3 are large and the term involving λ^2 may be neglected; in this event,

$$\lambda \simeq 2v_2 \qquad (3)$$

On the other hand, if only a trace of hydrogen is present; v_3 is small, the term involving λ may be neglected, and

$$\lambda^2 \simeq \frac{2v_2 v_3 (v_1 + v_5)}{v_2 + (v_1 + v_5)} \qquad (4)$$

If we choose a mixture with a large amount of carbon monoxide, v_5 is large and

$$\lambda \sim \sqrt{2v_2 v_3} \qquad (5)$$

If there is a large amount of oxygen, v_2 is large and

$$\lambda \sim \sqrt{2v_3(v_1 + v_5)}$$

$$\lambda \sim \sqrt{2v_3 v_1} \qquad \text{for} \qquad [H_2] > [CO] \qquad (6)$$

$$\lambda \sim \sqrt{2v_3 v_5} \qquad \text{for} \qquad [CO] > [H_2]$$

This, then, outlines a strategy for obtaining rates of reactions I, II, III, and IV. First, a mixture rich in hydrogen is used to determine k_2. Next, with k_2 known, a mixture with a trace of hydrogen and rich in carbon monoxide is used to determine k_3. Finally, with k_3 known, mixtures with excess oxygen and varying proportions of hydrogen and carbon monoxide are used to isolate k_1 and k_5.

The foregoing discussion indicates a qualitative procedure for selecting gas mixtures. However, we also need a quantitative measure of the sensitivity of the growth constant for a particular mixture to the various rate constants. For example, we know that to isolate k_3 we need a mixture with a trace of hydrogen, a small amount of oxygen, and an excess of carbon monoxide. But, for a candidate composition, is the hydrogen concentration small enough, and is carbon monoxide sufficiently in excess? A quantitative measure of the sensitivity to the various rates can be obtained by logarithmic partial differentiation of equation (1). For example,

$$\left(\frac{\partial \ln \lambda}{\partial \ln v_3}\right) = \frac{1}{2} - \frac{1}{2}\left[\frac{\lambda^2 + 2v_3\lambda + (v_1 + v_5)(v_3 - v_4) + v_3 v_4}{3\lambda^2 + 2(v_1 + v_2 + v_3 + v_4 + v_5) + (v_1 + v_5)(v_3 + v_4) + v_3 v_4}\right] \qquad (7)$$

Equation (7) shows that the growth constant depends on something less than $\sqrt{v_3}$ (a somewhat weaker dependence than that suggested by equation (5)).

The mixture compositions selected are shown in table I along with the sensitivities calculated for a pressure of 1 atmosphere and the temperatures near the midpoints of the ranges of the experimental data. These mixtures were chosen on the basis of (1) high sensitivity to the rate constant being determined, (2) minimized sensitivity to the other rate constants, (3) growth constants in a convenient range for measurement (5×10^3 to $7 \times 10^4 sec^{-1}$), and (4) sufficient content of minor, rate-limiting constituents to permit accurate mixture preparation.

It was necessary to include in each mixture sufficient infrared-active gas so that the arrival of the contact surface could be detected by the cessation of infrared emission. (The position of the contact surface between the driver and the driven gas was needed for the boundary layer analysis.) Mixtures 2, 3, and 5 have substantial carbon monoxide concentrations; carbon dioxide was added to mixture 1 to achieve adequate infrared activity. Carbon dioxide was also added to mixtures 3 and 5 to ensure vibrational relaxation of the carbon monoxide. In preliminary experiments on a composition similar to mixture 3 (both without CO_2) carbon monoxide was not relaxed and rate constants gave an activation energy of 15 kcal for reaction 3; this is much higher than the values shown in reference 7. Results from mixture 3, with added CO_2, show that the preliminary data were too low (particularly at the lower temperatures).

CALCULATION OF RATE CONSTANTS FROM EXPONENTIAL GROWTH CONSTANTS

Rate constants were obtained from the experimental growth constants by means of equation (1), which was rearranged and solved for the rate constant being sought from the mixture in question: k_2 from mixture 2, k_3 from mixture 3, etc. Mixture 2 was studied first, because the growth constants for this mixture depend almost exclusively on k_2 and are only slightly affected by the rates of the other reactions (table 1). Values of v_4 were calculated from the k_4 suggested by the Leeds Group (ref. 8). Trial values of k_1, k_3, and k_5 were also taken from the Leeds recommendations (refs. 7 to 9), but final values were taken from our own determinations. This involves an iterative procedure since our values of k_3 depend, in turn, on our values of k_2 and, to a lesser extent, of k_5. Two iterations sufficed to establish k_2.

Next, k_3 was obtained by analyzing the growth constants for mixture 3, then k_1 was obtained from mixture 1, and finally k_5 was obtained from mixture 5. Three iterations around the k_3-k_1-k_5 loop were required.

A least-squares fit to the Arrhenius equation was made for each set of rate constants; these equations were then used in subsequent calculations.

The experimental results are presented in the order in which the data were obtained - first k_2, then k_3, k_1, and k_5. This is also the order of decreasing precision.

Rate constants for reactions II and III are plotted as functions of reciprocal temperature in figure 5. The least-squares lines through the data are

$k_2 = 1.25 \times 10^{14} \exp(-16.3 \text{ kcal}/RT) \text{ cm}^3 \text{ mole}^{-1} \text{ sec}^{-1}$
$k_3 = 2.96 \times 10^{13} \exp(-9.8 \text{ kcal}/RT) \text{ cm}^3 \text{ mole}^{-1} \text{ sec}^{-1}$

Figure 6 contains the data for reactions I and V plotted as functions of the reciprocal temperature. The least-squares lines through the data are

$$k_1 = 1.9 \times 10^{13} \exp(-4.8 \text{ kcal/RT}) \text{ cm}^3 \text{ mole}^{-1} \text{ sec}^{-1}$$
$$k_5 = 1.0 \times 10^{12} \exp(-3.7 \text{ kcal/RT}) \text{ cm}^3 \text{ mole}^{-1} \text{ sec}^{-1}$$

In this paper we showed how to make systemmatic measurements so as to isolate the rates of individual bimolecular reaction steps in the complex of six reactions which describe the ignition behavior of the hydrogen-carbon monoxide-oxygen system.

We have obtained what we believe are quite accurate measurements of the rates of the reactions $H + O_2 \rightarrow OH + O$ and $O + H_2 \rightarrow OH + H$. Proper accounting of the effects of boundary layer growth on the pressure, temperature, and residence time behind the shock wave has been essential. Our measurements of the rates of $OH + H_2 \rightarrow H_2O + H$ and $OH + CO \rightarrow CO_2 + H$ were less precise but were perhaps the most direct determinations of these rates for temperatures above 1100 K (previous high-temperature determinations of these rates have been based on flame sampling). Finally, we have estimated the rate of the initiation reaction $CO + O_2 \rightarrow CO_2 + O$.

METHANE OXIDATION BEHIND REFLECTED SHOCK WAVES, IGNITION DELAY TIMES MEASURED BY PRESSURE AND FLAME-BAND EMISSION

Large computers have enabled us to assemble kinetic mechanisms for modeling the combustion of many fuels. These mechanisms may have as many as 150 reactions (variables) and in some cases the only experimental parameter matched has been the ignition delay times obtained from shock tubes. Many studies have been conducted on the ignition of methane-oxygen gas mixtures in shock tubes. However, in some cases the data are in error because of probe location, and in other cases the data are badly scattered because of poor measurements of the incident shock velocity or a very noisy pressure trace.

The delay time measured for a shock-heated hydrocarbon-oxygen mixture is known to be a function of initiation reactions, of reactions of radicals and molecular oxygen with the fuel, and of branching reactions. These branching reactions increase the radical concentrations to a level where ignition will occur. During ignition, there is rapid depletion of the primary fuel, very high radical concentrations, and an exponential rise in temperature and pressure. Usually delay times are measured somewhere in this region by techniques which follow some physical process such as change in pressure or in the appearance of some emitting species. Although the time difference between the start and completion of the pressure rise is small, one would like to determine the time of the appearance of the signal as accurately as possible. This time, which is the start of the ignition process, allows one to separate the fast ignition mechanism from the kinetics of the primary fuel.

The next section presents ignition delay data for the oxidation of methane. Data were measured with a quiet pressure transducer for the temperature range of 1500 to 1920 K. The quiet pressure trace allowed us to determine the initial rise in the ignition pressure. The delay times determined from this initial pressure rise were compared with the time of appearance of the

radiation at 3700 Å. In addition, the methane and carbon dioxide concentrations at the time of ignition will be measured. These parameters, which must be duplicated by any kinetic model, will be used to test the correctness of published kinetic models for the combustion of methane.

RESULTS AND DISCUSSION

Ignition Delay Times and Probe Location

Frenklach (ref. 10) measured ignition delay times at two locations in a shock tube and concluded that the location of the probe must be taken into consideration when selecting delay-time data to be modeled by a kinetic mechanism. Since optical access was necessary to monitor the infrared and ultraviolet radiation behind the reflected shock wave, it was important to know the error involved in measuring the delay time 7 mm from the reflecting surface. Therefore, two pressure transducers were located 7 and 83 mm from the reflecting surface. These allowed us to simultaneously measure the delay time for two locations in the same experiment (see fig. 7). An ethane-oxygen-argon mixture (1.27, 5.05, and 93.68 percent, respectively) was used for this series of tests. For these experiments, delay time was defined as the time at which the ignition pressure exceeded P_5 by 10 percent. This eliminated the guess-work usually involved in determining the point at which the pressure departed from the flat portion of the trace. Figure 8 is a plot of the delay times for the two locations as a function of $1/T$. A curve drawn through the data taken at the 83-mm position appears to show a constant difference in the time between the two locations.

A clearer understanding of this phenomenon can be obtained from figure 9, which is a time-distance (t-x) plot of the trajectory of the incident and reflected shock waves near the end of the shock tube. As can be seen, the time at which shock heating occurs at a given location along the tube is a function of the reflected shock velocity and the distance from the end wall. Thus, ignition would be expected to occur at the end wall first, since the gas there has been heated much longer. When ignition occurs, the pressure rise causes a disturbance which propagates down the tube. The mininum propagation velocity of this disturbance is the speed of sound in the shocked gas. Vermeer (ref. 11) took schlieren photographs of ignition behind the reflected shock wave, and they clearly showed that the disturbance propagated at a velocity much greater than the reflected shock wave.

The data in figure 8 were used to calculate the propagation velocity between the two probes. This velocity had an average value of 1660 m/sec, which is a Mach number of about 2.5. This velocity is about four times that of the reflected shock wave. Using this velocity one can estimate that the delay times measured at the 7-mm position would be too short by about 10 μsec. This error would not be important unless the measured delay times were near 100 μsec. No corrections have been made in the present data, but times less than 100 μsec are not considered reliable.

Another disturbing feature of the pressure traces is the amplitude of the ignition pressure. Unless something changes, one expects the ignition pressure to be the same at all locations in the tube. However, the ignition pressure for probe 2 is much larger than that at probe 1 (fig. 4). The ratio of the

ignition pressure to the reflected shock pressure P_5 for the two probe positions is plotted as a function of the delay time at probe 1 in figure 10. Note that this ratio is nearly constant at probe 1 but increases with decreasing delay times for probe 2. This behavior suggests that the gas properties at ignition are not the same at the two locations.

Ignition Delay Times

Ignition delay times were measured behind reflected shock waves for the mixtures shown in table II. The pressure history and the carbon monoxide flame-band emission at 3700 Å were used to determine the onset of ignition. The delay times measured by both pressure and flame-band emission are recorded in table III. These delay times τ may be correlated by an empirical relation of the form

$$\tau = A \exp(B/RT)[CH_4]^a[O_2]^b[Ar]^c \tag{8}$$

Lifshitz (ref. 12) and Tsuboi (ref. 13) both found an overall pressure dependence of -0.7 for $a + b + c$. Plots of $\tau P^{0.7}$ as a function of $1/T$ for each mixture are shown in figure 8. A least-squares fit to the data yielded the following equations:

$$\varphi = 0.5 \quad \tau P^{0.7} = 9.59 \times 10^{-5} \exp(51.93 \times 10^3/RT) \; \mu sec\text{-}atm^{0.7} \tag{9}$$

$$\varphi = 1.0 \quad \tau P^{0.7} = 2.85 \times 10^{-5} \exp(58.83 \times 10^3/RT) \; \mu sec\text{-}atm^{0.7} \tag{10}$$

$$\varphi = 2.0 \quad \tau P^{0.7} = 3.65 \times 10^{-5} \exp(58.74 \times 10^3/RT) \; \mu sec\text{-}atm^{0.7} \tag{11}$$

A correlation of all of the data in the form used by Lifshitz, $\tau[CH_4]^{-0.33}[O_2]^{1.03}$, is shown in figure 11. The activation energies for the present data were larger than those found by Lifshitz and appear to have depended upon the concentration of oxygen. The mixtures of $\varphi = 1.0$ and 2.0 had 4-percent oxygen and the same activation energy, while the mixture for $\varphi = 0.5$ had 8-percent oxygen and a measurably lower activation energy. This is the same behavior reported by Tsuboi.

REFERENCES

1. Gaydon, A.G; and Hurle, I.R.: The Shock Tube in High-Temperature Chemical Physics. Reinhold Publishing, 1963.

2. Greene, E.F.; and Toennies, J.P.: Chemical Reactions in Shock Waves. Academic Press, 1964.

3. Gordon, S; and McBride, B.J.: Computer Program for Calculation of Complex Chemical Equilibrium Compositions, Rocket Performance, Incident and Reflected Shocks, and Chapman-Jouguet Detonations. NASA SP-273, 1976.

4. Brokaw, R.S.: Analytic Solutions to the Ignition Kinetics of the Hydrogen-Oxygen Reaction. Tenth Symposium (International) on Combustion, The Combustion Institute, 1965, pp. 269-278.

5. Brokaw, R.S.: Ignition Kinetics of the Carbon Monoxide-Oxygen Reaction. Eleventh Symposium (International) on Combustion, The Combustion Institute, 1967, pp. 1063-1073.

6. Clyne, M.A.A.; and Thrush, B.A.: Mechanism of Chemiluminescent Combination Reactions Involving Oxygen Atoms. Proc. Roy. Soc. (London), Ser. A, vol. 269, no. 1338, Sept. 25, 1962, pp. 404-418.

7. Baulch, D.L.; Drysdale, D.D.; and Lloyd, A.C.: Critical Evaluation of Rate Data for Homogeneous, Gas-Phase Reactions of Interest in High Temperature Systems. High Temperature Reaction Rate Data, vol. 2, Dept of Physical Chemistry, The University Leeds, Nov. 1968.

8. Baulch, D.L.; Drysdale, D.D.; and Lloyd, A.C.: Critical Evaluation of Rate Data for Homogeneous, Gas-Phase Reactions of Interest in High Temperature Systems. High Temperature Reaction Rate Data, vol. 3, Dept of Physical Chemistry, The University, Leeds, Apr. 1969.

9. Baulch, D.L.; Drysdale, D.D.; and Lloyd, A.C.: Critical Evaluation of Rate Data for Homogeneous, Gas-Phase Reactions of Interest in High Temperature Systems. High Temperature Reaction Rate Data, vol. 1, Dept. of Physical Chemistry, The University, Leeds, May 1968.

10. Frenklach, M.; and Bornside, D.E.: Shock-Initiated Ignition in Methane-Propane Mixtures. Combust. Flame, vol. 56, no. 1, Apr. 1984, pp. 1-27.

11. Vermeer, D.J.; Meyer, J.W.; and Oppenheim, A.K.: Auto-Ignition of Hydrocarbons Behind Reflected Shock Waves. Combust. Flame, vol. 18, no. 3, June 1972, pp. 327-336.

12. Lifshitz, A., et al.: Shock-Tube Investigation of Ignition in Methane-Oxygen-Argon Mixtures. Combust. Flame, vol. 16, no. 3, June 1971, pp. 311-321.

13. Tsuboi, T.; and Wagner, H.G.: Homogeneous Thermal Oxidation of Methane in Reflected Shock Waves. Fifteenth Symposium (International) on Combustion, The Combustion Institute, 1971, pp. 883-890.

TABLE I. - MIXTURE COMPOSITIONS AND GROWTH CONSTANT SENSITIVITIES

Constituents	Mixture			
	1	2	3	5
	Reaction			
	$OH + H_2 \rightarrow$ $H_2O + H$	$H + O_2 \rightarrow$ $OH + O$	$O + H_2 \rightarrow$ $OH + H$	$OH + CO \rightarrow$ $CO_2 + H$
	Composition, percent			
H_2	0.21	5	0.1046	0.1035
CO	.11	6	10.0	6.01
O_2	10.0	0.5	.503	10.0
CO_2	5.0	---	4.99	5.0
Sensitivities	Mixture			
	1	2	3	5
	Reaction			
	$OH + H_2 \rightarrow$ $H_2O + H$	$H + O_2 \rightarrow$ $OH + O$	$O + H_2 \rightarrow$ $OH + H$	$OH + CO \rightarrow$ $CO_2 + H$
$(\partial \ln \lambda)/(\partial \ln v_1)$	0.34	0.01	0.00	0.07
$(\partial \ln \lambda)/(\partial \ln v_2)$	.33	1.00	.64	.21
$(\partial \ln \lambda)/(\partial \ln v_3)$	.48	.06	.39	.49
$(\partial \ln \lambda)/(\partial \ln v_4)$	-.17	-.07	-.06	-.06
$(\partial \ln \lambda)/(\partial \ln v_5)$	.02	.00	.04	.29

TABLE II. - COMPOSITION OF GAS

MIXTURES AND TEMPERATURE

RISE DUE TO IGNITION

Equivalence ratio, φ	CH₄	O₂	Ar	Temperature rise due to ignition, K
	Composition, percent			
0.50	2	8	90	894
1	2	4	94	882
2	4	4	92	729

TABLE III. - IGNITION DELAY TIMES MEASURED BY

PRESSURE AND FLAME BAND EMISSION

(a) Equivalence ratio, φ, 0.5; methane, 2 percent;
oxygen, 8 percent; argon, 90 percent

Temperature, K	1/T, K⁻¹	Pressure, atm	Delay times, μsec	
			Pressure	Emission
1778	5.624×10^{-4}	3.464	99	110
1763	5.672	3.418	102	110
1752	5.708	3.371	112	125
1730	5.780	3.318	159	167
1695	5.900	3.199	201	208
1687	5.928	3.191	208	209
1657	6.035	3.072	323	322
1620	6.173	2.979	508	512
1610	6.211	2.950	533	542
1605	6.231	2.918	594	597
1601	6.246	2.922	672	672
1579	6.333	2.857	663	658
1576	6.345	2.835	742	738
1555	6.431	2.773	850	858
1554	6.435	2.786	958	964
1531	6.532	2.704	1144	1145
1499	6.671	2.613	1655	1649

TABLE III. - Concluded.

(b) Equivalence ratio, φ, 1.0; methane, 2 percent; oxygen, 4 percent; argon, 90 percent

Temperature, K	1/T, K^{-1}	Pressure, atm	Delay times, μsec	
			Pressure	Emission
1915	5.222x10^{-4}	3.680	57	59
1866	5.359	3.536	84	78
1802	5.549	3.354	171	166
1780	5.618	3.279	201	219
1775	5.638	3.278	185	192
1746	5.727	3.183	295	295
1732	5.774	3.147	383	383
1725	5.797	3.122	397	396
1710	5.848	3.082	427	414
1707	5.858	3.077	531	559
1689	5.921	3.023	525	522
1689	5.921	3.032	589	589
1655	6.042	2.932	794	775
1645	6.079	2.900	867	861
1635	6.116	2.876	967	973
1629	6.139	2.855	1072	1075
1615	6.192	2.822	1163	1144
1593	6.278	2.761	1448	1471

(c) Mixture ratio, φ, 2.0; methane, 4 percent; oxygen, 4 percent; argon, 92 percent

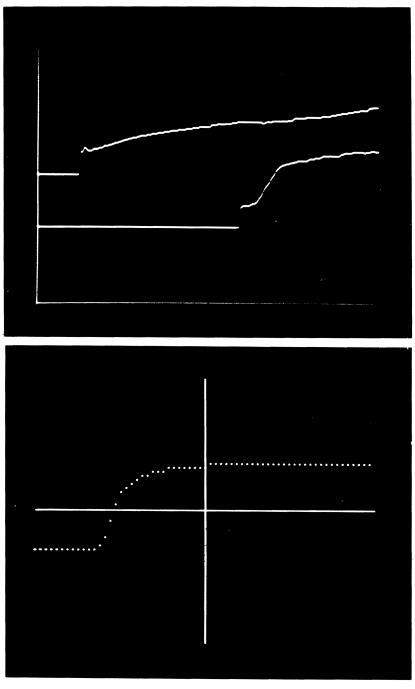| Temperature, K	1/T, K^{-1}	Pressure, atm	Delay times, μsec	
			Pressure	Emission
1922	5.203x10^{-4}	4.012	67	62
1856	5.388	3.797	116	110
1789	5.590	3.583	198	201
1770	5.650	3.524	249	271
1763	5.672	3.485	318	304
1730	5.780	3.381	369	368
1715	5.831	3.351	509	501
1712	5.841	3.326	489	486
1691	5.914	3.260	690	682
1681	5.949	3.228	765	767
1677	5.963	3.217	795	797
1650	6.061	3.134	1102	1096
1627	6.146	3.063	1214	1221
1621	6.169	3.043	1319	1321
1602	6.242	2.984	1534	1557

Figure 1. - Shock velocity measurement. Output from thin-film probe amplifier fed to digital oscilloscope. Time per point, 200 n sec. Lower trace shows expansion of scale, which is helpful in determining exact time shock wave passed probe position.
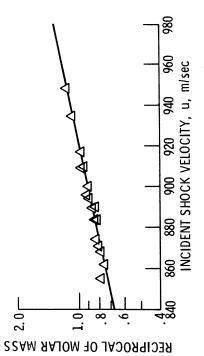
Figure 2. – Shock velocity as function of molar mass of driver gas for constant pressure ratio across diaphragm.
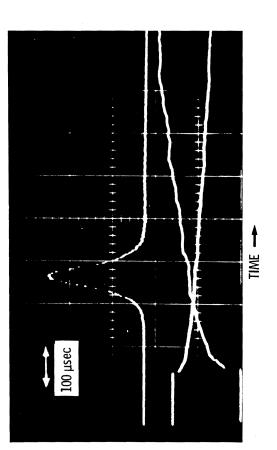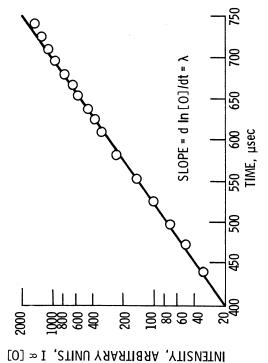
RECIPROCAL OF MOLAR MASS

INCIDENT SHOCK VELOCITY, u, m/sec

SLOPE = d ln [O]/dt = λ

INTENSITY, ARBITRARY UNITS, I ∝ [O]

TIME, μsec

Figure 4. – Flame-band emission intensity as function of time.

100 μsec

TIME →

Figure 3. – Flame-band emission for mixture of hydrogen/oxygen/carbon monoxide/argon.

220
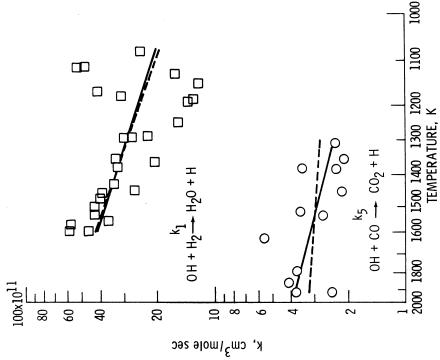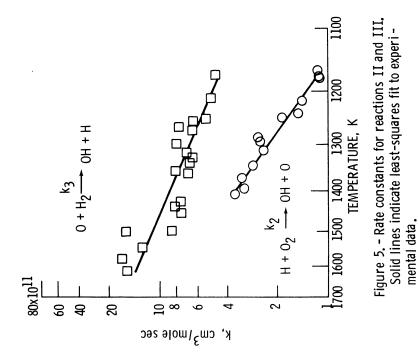
Figure 6. - Rate constants for reactions I and V. Solid lines indicate least squares fit to experimental data. Dashed lines indicate least-squares fit to experimental data plus 300 K datum of Greiner (ref. 13).

Figure 5. - Rate constants for reactions II and III. Solid lines indicate least-squares fit to experimental data.
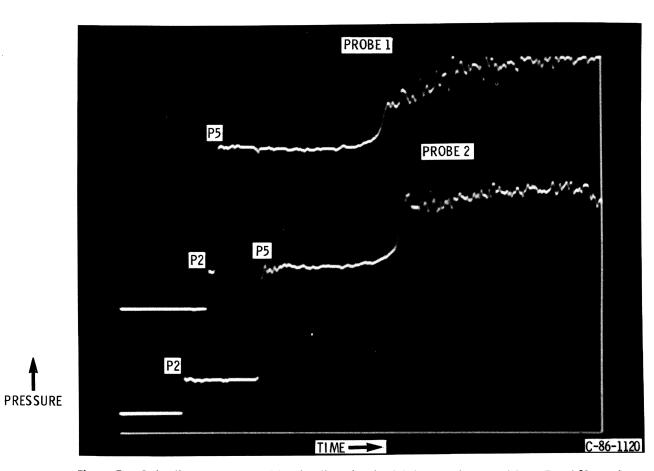
Figure 7. – Delay times measured at two locations in shock tube. Probes 1 and 2 are 7 and 83 mm from reflecting surface, respectively. P2 is incident shock pressure and P5 is reflected shock pressure. Measured delay times were 712 and 574 μsec.
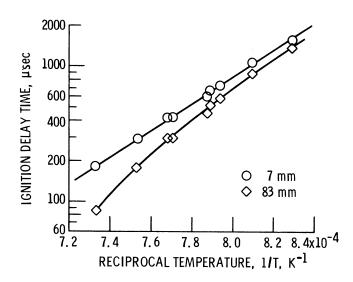
Figure 8. - Ignition delay times for a 1.27-per-cent C_2H_6, 5.05-percent O_2, 93.68-percent Ar (φ = 0.88) mixture as recorded at two different locations along shock tube.
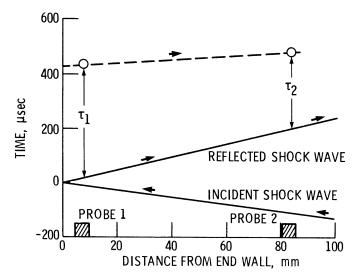

Figure 9. - Time-distance diagram of incident and reflected shock trajectory and delay times τ measured at two locations. Propagation of ignition wave shown by dashed line.
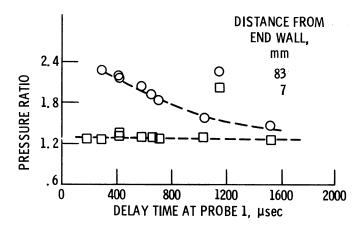
Figure 10. - Ratio of ignition pressure to reflected shock pressure, demonstrating enhanced ignition at second probe position, particularly for shorter delay times.
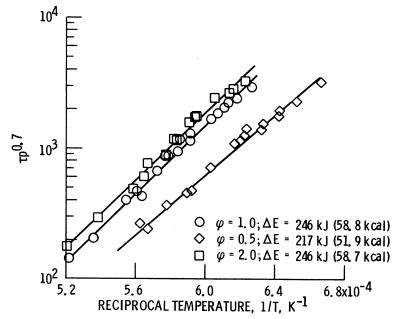

Figure 11. - $\tau p^{0.7}$ as function of $1/T$ for all three CH_4 mixtures, $\varphi = 0.5$, $\varphi = 1.0$, and $\varphi = 2.0$.

REPORT DOCUMENTATION PAGE

1. AGENCY USE ONLY (Leave blank)	2. REPORT DATE September 1985	3. REPORT TYPE AND DATES COVERED Conference Publication

4. TITLE AND SUBTITLE

Combustion Fundamentals
NASA–Chinese Aeronautical Establishment (CAE) Symposium

5. FUNDING NUMBERS

WU–505–62–21–00

6. AUTHOR(S)

None

7. PERFORMING ORGANIZATION NAME(S) AND ADDRESS(ES)

National Aeronautics and Space Administration
Lewis Research Center
Cleveland, Ohio 44135–3191

8. PERFORMING ORGANIZATION REPORT NUMBER

E–3033

9. SPONSORING/MONITORING AGENCY NAME(S) AND ADDRESS(ES)

National Aeronautics and Space Administration
Washington, DC 20546–0001

10. SPONSORING/MONITORING AGENCY REPORT NUMBER

NASA CP–2433

11. SUPPLEMENTARY NOTES

None

12a. DISTRIBUTION/AVAILABILITY STATEMENT

Unclassified - Unlimited
Subject Category 07

This publication is available from the NASA Center for AeroSpace Information, (301) 621–0390.

12b. DISTRIBUTION CODE

13. ABSTRACT (Maximum 200 words)

A NASA–Chinese Aeronautical Establishment (CAE) symposium on combustion fundamentals was held at the NASA Lewis Research Center from September 23–27, 1985. This symposium was the result of an agreement (signed on January 31, 1979) between the United States of America and the People's Republic of China on cooperation in science and technology. A protocol agreement between NASA and CAE was established in May 1983 to conduct exchanges and collaborative activities on the basis of equality, reciprocity, and mutual benefit. The initial agreement was to hold two symposia in the subject areas of structural analysis methods and theoretical and experimental research in combustion fundamentals. This publication is a compilation of the technical papers presented at the second symposium. It consists of five papers from senior specialists of CAE and seven papers from NASA senior specialists.

14. SUBJECT TERMS

Combustion; Fluid mechanics; Kinetics; Fuel sprays

15. NUMBER OF PAGES
231

16. PRICE CODE
A11

17. SECURITY CLASSIFICATION OF REPORT	18. SECURITY CLASSIFICATION OF THIS PAGE	19. SECURITY CLASSIFICATION OF ABSTRACT	20. LIMITATION OF ABSTRACT
Unclassified	Unclassified	Unclassified	